Synthesis and surface reactivity of ZnO: application to gas and photon detection

by

©Jiaqi Cheng

A thesis submitted to the School of Graduate Studies in partial fulfillment of the requirements for the degree of

Doctor of Philosophy

Department of Chemistry

Memorial University of Newfoundland

March 2016

St. John's Newfoundland

Abstract

This work employs different synthesis techniques to control the surface properties of polycrystalline ZnO for sensing device applications. ZnO micro-scale and nano-scale particles were made by various solid-state, solvothermal, and high temperature synthesis techniques that are designed for controlling crystal habit, surface polarity and surface area. The ZnO samples exhibited different degrees of degradation when exposed to ambient water and CO_2, which were linked to ZnO surface dissolution and crystal growth conditions. In addition, a strategy for controlling the hydroxide in the products of the solid-state metathesis has been developed.

Thin film gas sensors were assembled using the ZnO products. The capacitance responses of ZnO particles were evaluated after exposure to volatile organic compounds (ethanol and hexane) at various operation temperatures between 20 and 500 °C. The results showed that gas sensing processes at low temperatures were mediated by the ambient humidity when detecting hydrophilic gases, and the responses from ZnO nanoparticles were greatly enhanced at high temperatures. Furthermore, a preliminary study for UV ac-

tivated gas sensing was conducted to examine the effect of UV light radiation on the electrical properties of the ZnO samples, in which the AC frequency dependence of the photoresponse was revealed by electrical impedance spectroscopy.

Acknowledgments

I would like to express my deep gratitude to my supervisor, Dr. Kristin M. Poduska, for her full support of this thesis. Her supervision has a character that to me can be best described in those super-fast and thorough email replies and weekly one-on-one meetings. It has been a great pleasure working with her in this journey of my Ph.D. pursuit as she helps me to evolve toward an independent researcher.

I would like to thank a number of colleagues in Poduska group with whom I had the pleasure of working and hanging out: Dr. Muhammad Asim Rasheed (who helped with my first ever experiment in graduate school) has been a mentor to me at the beginning of my Ph.D. program. Throughout my program, I have received direct help from Haruki Hirasaw, Han Chao, Jake Wells, Kayla Kenneally and Liam Whelan who were involved in various projects that made the chapters of this thesis. My thanks to fellow graduate students and postdoctoral fellows: Payam Bagheri, Dr. Tiju Thomas, Dr. Jie Ma and Dr. Chuan (Sandy) Xu, Dr. Ramesh Kumar, Zixian Li, Dr. Ben Xu and Tanzir Ahmed for all the fun time we spent together both on and

after work.

My thanks to my advisory board: Dr. Peter Pickup and Dr. Christina Bottaro for their annual evaluations and valuable comments that improve this thesis.

I would like express my special thanks to Dr. Erika Merschrod in the Department of Chemistry and her group members for constantly providing advice throughout my course work and research.

Finally, I thank my family for the unconditional love that drives me forward.

Table of Contents

List of Tables

List of Figures

List of Abbreviations and Symbols

Abbreviations

a.u.	arbitrary unit
AC	alternating current
BET	Brunauer-Emmett-Teller
CPE	constant phase element
DC	direct current
DLS	dynamic light scattering
DRS	diffuse reflectance spectroscopy
DRIFT	diffuse reflectance infrared Fourier transform spectroscopy
EDX	energy-dispersive X-ray spectroscopy
EIS	electrochemical impedance spectroscopy
EtOH	ethanol
FWHM	full width at half maximum
FTIR	Fourier transform infrared spectroscopy

GC-MS	gas chromatography mass spectrometry
ITO	indium tin oxide
JCPDS	Joint Committee for Powder Diffraction Studies
LCR	inductance-capactiance-resistance
MOX	metal oxides
PAHs	polycyclic aromatic hydrocarbons
ppb	parts per billion
ppm	parts per million
RH	relative humidity
RMS	root mean square
RT	room temperature
SEM	scanning electron microscopy
SSM	solid-state metathesis
TGA	thermogravimetric analysis
UV	ultraviolet
VOCs	volatile organic compounds
XPS	X-ray photoelectron spectroscopy
XRD	X-ray diffraction
ZC	smithsonite ($ZnCO_3$)
ZHC	hydrozincite ($Zn_5(OH)_6(CO_3)_2$)

Symbols

A	area
C	capacitance
d	distance
e^-	electron
f	frequency
h^+	hole
I	current
p	vapor pressure
Q	quasi-capacitance
R	resistance
S	sensitivity
T	temperature
V	voltage
Z	impedance
Z_{re}	real component of impedance
Z_{im}	imaginary component of impedance
ϵ	dielectric constant
ΔG	Gibbs free energy change
ζ	zeta potential
θ	angle
λ	wavelength
τ	time constant

ω angular frequency

Chapter 1

Introduction

1.1 Overview

The theme of this dissertation is materials chemistry issues associated with developing semiconductor gas sensors. Gas sensors have broad applications in domestic uses, such as air quality control, household carbon monoxide alarms, and breath alcohol tests for drunk driving violations [1]. They are also required by various industries for monitoring potential gas leaks [2]. The gas sensor research of this thesis is motivated by the oil and gas industry, who requires gas detection at special locations in harsh environments (*e.g.* the tip of a flare stack) for close monitoring of gaseous pollutant emissions generated from petroleum exploration and production processes. The emission often contains a mixture of volatile organic compounds (VOCs), polycyclic aromatic hydrocarbons (PAHs), CO_2, CO, NOx, SO_2, H_2S, and water [3].

By flaring alone these gases cannot be thoroughly eliminated. As a result, it is crucial for the oil and gas industry to have on-site detection with a gas sensor in close proximity to the emissions in order to assess the environmental impact of these products of incomplete combustion [3]. In principle, detection of the gases present in the emissions can be achieved with various types of gas sensors with different sensing mechanisms (optical, electrical, electrochemical). However, the challenge is that most gas sensors cannot survive the flare stack environment that combines high temperature, fast gas flow and interference from moisture. For this task, solid-state electrical gas sensors based on metal oxides (MOX) stand above the rest due to their high thermal durability, high gas sensitivity (ppm to ppb level) to a broad spectrum of target gases at elevated temperatures, fast signal response and recovery, and low cost [4–7].

The basic working principle behind solid-state electrical gas sensors is that variations of the electrical properties (conductance, capacitance, impedance) of the solid-state sensing elements can be triggered by gas-surface interactions [4, 8]. There are two factors that control the sensing performances of solid-state gas sensors: (1) the ability of the sensing element to interact with the analyte molecules, and (2) the ability to convert chemical energy from the gas-surface interactions into sensing signals [9–11].

Based on these two governing factors, not all MOX are suitable for gas sensing. High surface reactivity is required in order to trigger the surface chemistry that alters the electrical properties. However, many non-

transition-metal oxides, such as MgO, are too inert and too resistive (due to their large band gaps) for gas sensing applications [6, 11]. The transition-metal oxides (*e.g.* Fe_2O_3) with partially filled d shells are also not reliable sensor candidates because of their structural instability, as they can be easily oxidized or reduced [6]. As a result, the superior options are the transition semiconducting MOX with d^{10} (ZnO, SnO_2) or d^0 (TiO_2, WO_3) configurations [11, 12]. Recently, nanostructures (nanoparticle, nanowires, nanorods) of these MOX have been extensively investigated for gas sensing applications due to the enhanced sensitivity. Several recent review papers with this focus of nano-structured MOX gas sensors can be found in the literature [12–15].

The overall quality of a gas sensor is determined by the "4S" standard (sensitivity, speed, selectivity and stability) [4, 5]. Over the last decade of research, large enhancements in gas sensitivity and signal responses/recovery time (speed) have been achieved by various approaches, including reducing particle sizes [16], changing particle morphology [17], hybridizing with metal (Au, Pd, Ru) catalysts [18], and doping with other MOX [19]. Moreover, devices such as high electron mobility transistors, were constructed to amplify the sensing signals [20].

Nevertheless, issues associated with MOX based gas sensors are also apparent. First of all, the selectivity to target gases remains a great challenge because the sensing mechanism for many gases by MOX are similar and hardly distinguishable [4]. For example, ambient moisture is the most common interfering gas as it also triggers large sensing responses [21]. Second,

the stability criterion has been overlooked for MOXs sensors despite the important fact that they undergo perpetual chemical exchanges at their surfaces with the surrounding environment [22]. Third, due to reaction barriers, thermal (or photo) activation is often required for a MOX gas sensor to achieve optimal sensing responses [4, 23]. The operating temperature is normally above 250 °C for optimal sensitivity. This can be an advantage for MOX, especially when the sensors are used for extreme tasks, such as flare stack gas sensing. However, for general use, it is a drawback because a heater needs to be incorporated, which increases the cost of the sensor and reduces its minimization capacity [6].

1.2 Thesis goals

Resolving the issues outlined above requires understanding the surface chemistry responsible for triggering the electrical sensing signals under different conditions. This task is both intricate, as extremely rich chemistry is associated with the MOX surfaces, and nontrivial because such information is key to accelerating the development of reliable gas sensing devices.

In this dissertation, ZnO is my sensing material because it is reported to have high sensitivities to a large spectrum of gases, including CO [24], H_2 [25], H_2S [16], NOx [26], NH_3 [27] and different VOCs [28]. Comprehensive reviews of the properties and device applications of ZnO can be found in recent articles by Özgür *et al.* [29, 30]. ZnO adopts a wurtzite crystal structure [29].

ZnO is an n-type semiconductor with a band gap of 3.37 eV. ZnO has many attractive bulk properties that have sparked many device applications such as light-emitting diodes, thin film transistor, piezoelectric devices [30].

Investigating the surface properties of ZnO has been a popular research topic for a long time because ZnO is a key heterogeneous catalyst in methanol production. Also, ZnO is used in the rubber industry as a catalyst to accelerate sulphur-induced vulcanisation, a process for improving the mechanical properties of rubber [31]. Driven by the interests of understanding the mechanism behind the catalysis with ZnO, a number of studies have been conducted on various clean or adsorbate (H_2, $H_2O/-OH$, O_2, CO)-covered ZnO surfaces. Some representative experimental and theoretical studies can be found in the 2007 review article by C. Wöll [32]. The knowledge of ZnO surfaces including surface structures [33], active (binding/reaction) sites [34], and the structures and binding energies of adsorbates [35] provides insights on the detail of the gas-surface interactions. For example, consensus has been reached on two surface properties for ZnO: (1) the oxygen vacancies on ZnO surfaces are the active sites for catalyzing methanol production from CO/CO_2 and H_2, and (2) clean ZnO surfaces are easily hydroxylated when exposed to water [36]. In other words, the surfaces of ZnO tend to be hydrophilic.

Aimed at making contribution to the field of ZnO based gas sensor, my investigation focuses on the role of surface chemistry in the electrical responses of polycrystalline ZnO. My study follows three main steps: ZnO synthesis,

assessment of surface and electrical properties, and testing of sensing performances in different harsh environments at high temperature, high humidity, and under UV light irradiation. My work concentrates on two fundamental questions.

1.2.1 How does the capacitance of a ZnO film changes in the presence of various gases?

Most ZnO-based gas sensors measure the DC conductance/resistance changes triggered by gas-surface interactions. Herein, the capacitance responses of ZnO films under AC voltage are investigated. In general, AC capacitive gas sensors are relatively scarce in the market compared to the DC conductive sensors (except for humidity sensors), because the generation and processing of AC signals requires more expensive electronics [37]. However, in a previous study, stable sensing signals could not be obtained during DC conductive gas sensing with ZnO under ambient conditions because the baseline signal was drifting constantly [38]. This baseline drift has been attributed to the possible hydrolysis of ZnO surfaces induced by the DC potential [38]. Therefore, a low magnitude and zero-biased AC voltage is used in my work in order to reduce the impacts of electrolysis on the ZnO surfaces.

In the conductive sensing mode, a DC bias voltage (V) is applied across the layer of polycrystalline ZnO, and the current (I) passing through the sensing layer is measured. A sensing signal is observed when the resistance

(R) of the sensing layer is changed by gas-surface interactions [4]. This can be expressed as:

$$\Delta R = \frac{V}{I_0} - \frac{V}{I_t} \tag{1.1}$$

where I_0 and I_t are the current measured before and after gas exposure, respectively.

Capacitance describes the amount of charge a body can store when a given voltage is applied, and it is proportional to the dielectric constant of the body [39]. Upon gas exposure, a sensor's capacitance signal can result from changes of the effective dielectric constant caused by gas molecule adsorption [40]. This mechanism is believed to be the major sensing mechanism behind the commercial capacitive humidity sensors based on porous Al_2O_3 as water processes an abnormally large dielectric constant [41, 42] . For semiconducting MOX-based gas sensor, an alternative mechanism proposed by some studies–which has not been accepted widely—attributes the capacitance signal to the gas-induced change in the width of depletion region [43, 44]. A depletion region can be present at the surface of semiconductor as a consequence of band bending, induced by charge transfer interaction when the surface is in contact with other media (solid, air, water). Due to the separation of charges in the surface depletion region, it has a capacitance associated with its width [45]. During a gas sensing event, the capacitive responses can arise from the changes of this width induced by redox reactions at the surfaces [4, 12].

Investigations of this thesis focus on testing the capacitance responses of ZnO upon exposure of various gases under various experimental conditions. We discuss, based on our data, plausible explanations for the capacitive gas sensing signals.

1.2.2 What are the factors that improve ZnO as a gas sensing material?

A range of factors are known to affect ZnO capacitive gas responses, including operating temperature, ambient humidity, target gas identity, ZnO crystal size/shape and UV radiation.

1.2.2.1 Working temperature

It is well established that the operating temperature is a key factor in determining the gas sensing performances of MOX [6, 46]. Thus, in this thesis, capacitive gas sensing experiments with ZnO are conducted at different working temperatures, a factor that determines the nature of the gas sensing mechanism. In general, high temperatures (≥ 200 °C) are required for achieving the optimal gas sensitivity for ZnO. This is because the surface oxygen species, which are responsible for reacting with the gas analytes at the surface, only reach the optimal reactivity at higher temperatures [4, 6, 8, 11, 46].

At room temperature (RT), gas sensing with ZnO has been reported with inferior sensitivity [47]. It is believed that the adsorbed water on ZnO surfaces

plays a major role at room temperature. Chakrapani *et al.* [48, 49] proposed a sensing mechanism that attributes the changes of surface conductivities to the oxidation/reduction (redox) reactions or acid/base-type reactions triggered by the the gases dissolved in the surface water layer. However, according to this mechanism, it is less clear how ZnO might respond to VOC molecules. For example ethanol can readily dissolve in the surface water layer without apparent dissociation, or without triggering any redox reaction at the ZnO surface at RT [50].

In this thesis, we conducted capacitive gas sensing experiments at different temperatures from RT to 500 °C for various VOCs.

1.2.2.2 ZnO particle size and shape

A range of ZnO samples with various particles sizes and shapes were synthesized for gas sensing tests, since we expected that the morphology of ZnO particles would affect the sensing performances. In general, the reduction of the particle sizes into the nanometre-region can lead to sharp enhancement of gas sensing responses [8] because of the substantially increased surface to volume ratios.

The shapes of ZnO particles also matter for gas sensing performance. ZnO has polar and non-polar surfaces [51] with distinct surface chemistries. A rule of thumb is that the polar surfaces of ZnO are more reactive than the non-polar ones [34, 51]. To compare gas sensing behaviors between the polar and non-polar surfaces of ZnO, particles with various shapes were synthesized

[52].

1.2.2.3 Ambient humidity

In this thesis, the effects of ambient humidity were initially studied as an interference factor for gas sensing. However, we discovered an interesting effect of ambient humidity that is it helps to improve the selectivity of ZnO sensors. This finding shifted our emphasis on the role of ambient humidity from an annoyance to a facilitator for room temperature gas sensing [47].

Furthermore, the impacts of ambient humidity on the structural stability of ZnO were also investigated. It has been reported that the surfaces of ZnO undergo slight dissolution when covered by a thin water layer [53], causing the corrosion/degradation of ZnO [54, 55]. This issue is often overlooked in other research, even though the compositional changes induced by surface chemistry could alter the surface chemical and electrical properties, as well as the gas sensing performances, of ZnO.

1.2.2.4 The impact of UV radiation

Gas sensing responses of ZnO can also be substantially enhanced with UV-light stimulation [17]. Although the mechanism behind the photo-enhancement is not fully understood, UV activation for gas sensing provides an alternative to the conventional thermal activation strategy that requires heating of the sensing element, and makes highly sensitive (and potentially selective) room temperature operation possible for ZnO gas sensing. In this thesis, impacts

of UV radiation on the electrical properties of ZnO film were studied in the absence of target gases, as a first step toward UV-activated capacitive gas sensing.

1.3 Thesis structure

This thesis contains eight chapters based on three main themes: material synthesis, properties and device applications.

In Chapter 2, I review the basic theories of the experimental techniques that I employed to characterize ZnO materials.

Chapter 3 demonstrates the synthesis and structure characterizations of different ZnO micro- and nano-particles with size and particle shape specificity. The surface reactivity and stability of the ZnO samples are assessed, and the results provide new angles to assess surface stability [52].

Chapter 4 presents the capacitive gas sensing results for polycrystalline ZnO samples under ambient conditions. It shows that the moisture plays a major role in sensing ethanol vapor by ZnO at room temperature [47].

Chapter 5 presents the results of the capacitive gas sensing experiments conducted at elevated temperatures. We tested the sensing responses of various ZnO samples when exposed to different target gases, including ethanol, hexane, and water vapor.

Chapter 6 gives a preliminary study of ZnO photoresponses when exposed to UV light using both AC and DC electrical measurements.

Chapter 7 presents a synthetic strategy for making phase selective zinc carbonates nanoparticles by a facile solid-state metathesis method [56].

Chapter 8 includes a summary of the entire thesis. It also contains an assessment of the contributions of my ZnO research in a broader context, beyond gas sensor development.

1.4 Copyright and Authorship statement

 As the first author, I contributed to the collection and analysis of all experimental data, and to manuscript writing. Dr. Poduska helped write the paper. (Section 3.8 of this chapter was not part of the original publication).

section (4.7) is included for more discussion). As the first author, I contributed to the collection and analysis of all experimental data, and the manuscript writing. Dr. Muhammad Asim Rasheed, a former PhD student in the Poduska group, contributed to the design and setup of experiment, and to the manuscript editing. Dr. Poduska helped write the paper.

The content of Chapter 7 is reprinted with permission from *Nanomaterials*, **3**, 3, 2013, authored by Jiaqi Cheng and Dr. Kristin M. Poduska. As the first author of this publication, I contributed to the collection and analysis of all experimental data, and to the manuscript writing. Dr. Poduska helped write the paper.

The reminder of this thesis is work that has not been published elsewhere.

Bibliography

[1] Dieter Kohl. Function and Applications of Gas Sensors. *J. Phys. D: Appl. Phys.*, 34(19):R125, 2001.

[2] Björn Timmer, Wouter Olthuis, and Albert van den Berg. Ammonia Sensors and Their Applications-A Review. *Sens. Actuat. B*, 107(2):666–677, 2005.

[3] Aniefiok E. Ite and Udo J. Ibok. Gas Flaring and Venting Associated with Petroleum Exploration and Production in the Nigeria's Niger Delta. *Am. J. Envir. Protect. Sci.*, 1(4):70–77, 2013.

[4] N. Barsan, D. Koziej, and U. Weimar. Metal Oxide-Based Gas Sensor Research: How to? *Sens. Actuat. B*, 121:18–35, 2007.

[5] Yu-Feng Sun, Shao-Bo Liu, Fan-Li Meng, Jin-Yun Liu, Zhen Jin, Ling-Tao Kong, and Jin-Huai Liu. Metal Oxide Nanostructures and Their Gas Sensing Properties: A Review. *Sensors*, 12(3):2610–2631, 2012.

[6] G. Korotcenkov. Metal Oxides for Solid-State Gas Sensors: What Determines Our Choice? *Mater. Sci. Eng. B*, 139(1):1–23, 2007.

[7] Hua Bai and Gaoquan Shi. Gas Sensors Based on Conducting Polymers. *Sensors*, 7(3):267–307, 2007.

[8] Marion E. Franke, Tobias J. Koplin, and Ulrich Simon. Metal and Metal Oxide Nanoparticles in Chemiresistors: Does the Nanoscale Matter? *Small*, 2(1):36–50, 2006.

[9] Noboru Yamazoe. Toward Innovations of Gas Sensor Technology. *Sens. Actuat. B*, 108:2–14, 2005.

[10] Avner Rothschild and Yigal Komem. The Effect of Grain Size on the Sensitivity of Nanocrystalline Metal-Oxide Gas Sensors. *J. Appl. Phys.*, 95(11):6374–6380, 2004.

[11] G. H. Jain. MOS Gas Sensors: What Determines Our Choice? *Proceedings of the Fifth International Conference on Sensing Technology 2011*, N/A:71–77, 2011.

[12] Chengxiang Wang, Longwei Yin, Luyuan Zhang, Dong Xiang, and Rui Gao. Metal Oxide Gas Sensors: Sensitivity and Influencing Factors. *Sensors*, 10:2088–2106, 2010.

[13] M. M. Arafat, B. Dinan, Sheikh A. Akbar, and A. S. M. A. Haseeb. Gas Sensors Based on One Dimensional Nanostructured Metal-Oxides: A Review. *Sensors*, 12(6):7207–7258, 2012.

[14] Ghenadii Korotcenkov. Metal Oxides. In *Handbook of Gas Sensor Materials*, Integrated Analytical Systems, pages 49–116. Springer New York, 2013.

[15] Soumen Das and V. Jayaraman. SnO_2: A Comprehensive Review on Structures and Gas Sensors. *Prog. Mater. Sci.*, 66(0):112–255, 2014.

[16] L. Liao, H. B. Lu, J. C. Li, H. He, D. F. Wang, D. J. Fu, C. Liu, and W. F. Zhang. Size Dependence of Gas Sensitivity of ZnO Nanorods. *J. Phys. Chem. C*, 111(5):1900–1903, 2007.

[17] Mohammad R. Alenezi, Abdullah S. Alshammari, K. D. G. I. Jayawardena, Michail J Beliatis, Simon J. Henley, and S. R. P. Silva. Role of the Exposed Polar Facets in the Performance of Thermally and UV Activated ZnO Nanostructured Gas Sensors. *J. Phys. Chem. C*, 117(34):17850–17858, 2013.

[18] Liwei Wang, Shurong Wang, Mijuan Xu, Xiaojing Hu, Hongxin Zhang, Yanshuang Wang, and Weiping Huang. A Au-Functionalized ZnO Nanowire Gas Sensor for Detection of Benzene and Toluene. *Phys. Chem. Chem. Phys.*, 15:17179–17186, 2013.

[19] M. S. Wagh, G. H. Jain, D. R. Patil, S. A. Patil, and L. A. Patil. Modified Zinc Oxide Thick Film Resistors as NH_3 Gas Sensor. *Sens. Actuat. B*, 115(1):128–133, 2006.

[20] Travis Anderson, Fan Ren, Stephen Pearton, Byoung Sam Kang, Hung-Ta Wang, Chih-Yang Chang, and Jenshan Lin. Advances in Hydrogen, Carbon Dioxide, and Hydrocarbon Gas Sensor Technology Using GaN and ZnO-Based Devices. *Sensors*, 9(6):4669–4694, 2009.

[21] Zikui Bai, Changsheng Xie, Mulin Hu, Shunping Zhang, and Dawen Zheng. Effect of Humidity on the Gas Sensing Property of the Tetrapod-Shaped ZnO Nanopowder Sensor. *Sens. Actuat. B*, 149:12–17, 2008.

[22] Moazzam Ali and Markus Winterer. ZnO Nanocrystals: Surprisingly "Alive". *Chem. Mater.*, 22(1):85–91, 2010.

[23] Shan-Wei Fan, Arvind K. Srivastava, and Vinayak P. Dravid. UV-Activated Room-temperature Gas Sensing Mechanism of Polycrystalline ZnO. *Appl. Phys. Lett.*, 95(14):142106, 2009.

[24] Hyun-Wook Ryu, Bo-Seok Park, Sheikh A. Akbar, Woo-Sun Lee, Kwang-Jun Hong, Youn-Jin Seo, Dong-Charn Shin, Jin-Seong Park, and Gwang-Pyo Choi. ZnO Gel Derived Porous Film for CO Gas Sensing. *Sens. Actuat. B*, 96(3):717–722, 2003.

[25] O. Lupan, V. V. Ursaki, G. Chai, L. Chow, G. A. Emelchenko, I. M. Tiginyanu, A. N. Gruzintsev, and A. N. Redkin. Selective Hydrogen Gas Nanosensor Using Individual ZnO Nanowire with Fast Response at Room Temperature. *Sens. Actuat. B*, 144(1):56–66, 2010.

[26] Naoto Koshizaki and Toshie Oyama. Sensing Characteristics of ZnO-Based NOx Sensor. *Sens. Actuat. B*, 66:119–121, 2000.

[27] J. X. Wang, X. W. Sun, Y. Yang, H. Huang, Y. C. Lee, O. K. Tan, and L. Vayssieres. Hydrothermally Grown Oriented ZnO Nanorod Arrays for Gas Sensing Applications. *Nanotechnology*, 17(19):4995, 2006.

[28] Yali Cao, Pengfei Hu, Weiyu Pan, Yudai Huang, and Dianzeng Jia. Methanal and Xylene Sensors Based on ZnO Nanoparticles and Nanorods Prepared by Room-Temperature Solid-State Chemical Reaction. *Sens. Actuat. B*, 134:462–466, 2008.

[29] Ü. Özgür, Ya. I. Alivov, C. Liu, A. Teke, M. A. Reshchikov, S. Dogan, V. Avrutin, S.-J. Cho, and H. Morkoç. A Comprehensive Review of ZnO Materials and Devices. *J. Appl. Phys.*, 98(4):041301, 2005.

[30] Ü. Özgür, Daniel Hofstetter, and Hadis Morkoç. ZnO Devices and Applications: A Review of Current Status and Future Prospects. *Proc. IEEE*, 98(7):1255–1268, 2010.

[31] G. Heideman, R. N. Datta, J. W. M. Noordermeer, and B. van Baarle. Influence of Zinc Oxide During Different Stages of Sulfur Vulcanization. Elucidated by Model Compound Studies. *J. Appl. Polym. Sci.*, 95(6):1388–1404, 2005.

[32] Christof Wöll. The Chemistry and Physics of Zinc Oxide Surfaces. *Prog. Surf. Sci.*, 82:55–120, 2007.

[33] Markus Valtiner, Mira Todorova, Guido Grundmeier, and Jörg Neugebauer. Temperature Stabilized Surface Reconstructions at Polar ZnO(0001). *Phys. Rev. Lett.*, 103:065502, Aug 2009.

[34] Honggang Ye, Guangde Chen, Haibo Niu, Youzhang Zhu, Li Shao, and Zhijuan Qiao. Structures and Mechanisms of Water Adsorption on

ZnO(0001) and GaN(0001) Surface. *J. Phys. Chem. C*, 117(31):15976–15983, 2013.

[35] Wei An, Xiaojun Wu, and X. C. Zeng. Adsorption of O_2, H_2, CO, NH_3, and NO_2 on ZnO Nanotube: A Density Functional Theory Study. *J. Phys. Chem. C*, 112(15):5747–5755, 2008.

[36] Francesc Viñes, Ana Iglesias-Juez, Francesc Illas, and Marcos Fernández-García. Hydroxyl Identification on ZnO by Infrared Spectroscopies: Theory and Experiments. *J. Phys. Chem. C*, 118(3):1492–1505, 2014.

[37] Tatsumi Ishihara, Shinobu Sato, Tomokatsu Fukushima, and Yusaku Takita. Capacitive Gas Sensor of Mixed Oxide CoO-In_2O_3 to Selectively Detect Nitrogen Monoxide. *J. Electrochem. Soc.*, 143(6):1908–1914, 1996.

[38] Muhammad Asim Rasheed. *Synthesis, Electrical and Gas Sensing Properties of Polycrystalline ZnO Films.* PhD thesis, Memorial University of Newfoundland, 2012.

[39] A. K. Walton. *Network Analysis and Practice.* Cambridge University Press: Cambridage, UK, 1987.

[40] E. S. Snow, F. K. Perkins, E. J. Houser, S. C. Badescu, and T. L. Reinecke. Chemical Detection with a Single-Walled Carbon Nanotube Capacitor. *Science*, 307(5717):1942–1945, 2005.

[41] Zhi Chen and Chi Lu. Humidity Sensors: A Review of Materials and Mechanisms. *Sens. Lett.*, 3(4):274–295, 2005.

[42] Hamid Farahani, Rahman Wagiran, and Mohd Nizar Hamidon. Humidity Sensors Principle, Mechanism, and Fabrication Technologies: A Comprehensive Review. *Sensors*, 14(5):7881–7939, 2014.

[43] A. Erola, S. Okur, B. Combaa, O. Mermerc, and M. C. Arkana. Humidity Sensing Properties of ZnO Nanoparticles Synthesized by Sol-gel Process. *Sens. Actuat. B*, 145:174–180, 2010.

[44] Ghenadii Korotcenkov. Materials for Capacitance-Based Gas Sensors. In *Handbook of Gas Sensor Materials*, Integrated Analytical Systems, pages 365–376. Springer New York, 2013.

[45] S. M. Sze. *Physics of Semiconductor Devices*. John Wiley: New York, US, 1981.

[46] Liwei Wang, Yanfei Kang, Xianghong Liu, Shoumin Zhang, Weiping Huang, and Shurong Wang. ZnO Nanorod Gas Sensor for Ethanol Detection. *Sens. Actuat. B*, 162(1):237–243, 2012.

[47] Jiaqi Cheng, Muhammad Asim Rasheed, and Kristin M. Poduska. Exploiting Water-Mediated Ethanol Sensing by Polycrystalline ZnO at Room Temperature. *ECS J. Solid State Sci. Technol.*, 2(1):Q23–Q26, 2013.

[48] Vidhya Chakrapani, John C. Angus, Alfred B. Anderson, Scott D. Wolter, Brian R. Stoner, and Gamini U. Sumanasekera. Charge Transfer Equilibria Between Diamond and An Aqueous Oxygen Electrochemical Redox Couple. *Science*, 318(5855):1424–1430, 2007.

[49] Vidhya Chakrapani, Chandrashekhar Pendyala, Kathleen Kash, Alfred B. Anderson, Mahendra K. Sunkara, and John C. Angus. Electrochemical Pinning of the Fermi Level: Mediation of Photoluminescence from Gallium Nitride and Zinc Oxide. *J. Am. Chem. Soc.*, 130(39):12944–12952, 2008.

[50] K. K. Korir, A. Catellani, and G. Cicero. Ethanol Gas Sensing Mechanism in ZnO Nanowires: An ab Initio Study. *J. Phys. Chem. C*, 118(42):24533–24537, 2014.

[51] Jacek Goniakowski, Fabio Finocchi, and Claudine Noguera. Polarity of Oxide Surfaces and Nanostructures. *Rep. Prog. Phys.*, 71(1):016501, 2008.

[52] Jiaqi Cheng and Kristin M. Poduska. Ambient Degradation of ZnO Powders: Does Surface Polarity Matter? *ECS J. Solid State Sci. Technol.*, 3(5):P133–P137, 2014.

[53] Andrej Degen and Marija Kosec. Effect of pH and Impurities on the Surface Charge of Zinc Oxide in Aqueous Solution. *J. Eur. Ceram. Soc.*, 20(6):667–673, 2000.

[54] Zhengwei Pan, Jing Tao, Yimei Zhu, Jing-Fang Huang, and M. Parans Paranthaman. Spontaneous Growth of $ZnCO_3$ Nanowires on ZnO Nanostructures in Normal Ambient Environment: Unstable ZnO Nanostructures. *Chem. Mater.*, 22(1):149–154, 2010.

[55] K. A. Cimatu, S. M. Mahurin, K. A. Meyer, and R. W. Shaw. Nanoscale Chemical Imaging of Zinc Oxide Nanowire Corrosion. *J. Phys. Chem. C*, 116(18):10405–10414, 2012.

[56] Jiaqi Cheng and Kristin M. Poduska. A Strategy for Hydroxide Exclusion in Nanocrystalline Solid-State Metathesis Products. *Nanomater.*, 3(3):317–324, 2013.

Chapter 2

Experimental Methods

Every sample I made for this thesis work has been carefully characterized by a range of spectroscopic, microscopic, and electrical techniques. I assessed structure, particle size/shape, surface and interface characteristics, as well as electronic properties of my ZnO samples. Taken together, these measurements give a comprehensive picture of the sample characteristics. This chapter introduces working principles and details of the measurements, and examples of relevant data.

2.1 Bulk structure characterization

The samples synthesized in this thesis are polycrystalline powders, which contain a large number of particles. Bulk characterization involves a set of measurements for identifying the crystal structure and chemical composition

of the synthesis products because I need products with high purity.

2.1.1 Powder X-ray diffraction

Structure determination of crystalline samples was achieved with powder X-ray Diffraction (XRD). I used an XRD facility with a Rigaku Ultima IV X-ray diffractometer managed by the Core Research Equipment & Instrument Training Network (CREAIT), Memorial University. The measurements were done with the help of Dr. Wanda Aylward. Typically, $\sim$ 1 g of dry sample powder was spread on a sample holder for analysis.

The XRD data are presented using a plot of intensity versus angle. Fig. 2.1 shows an example of the XRD profile for a polycrystalline ZnO sample, in which all peaks correspond to the specific crystal planes of wurtzite ZnO (crystal planes are indexed with Miller indices (hkl)). Fig. 2.1 indicates successful preparation of single-phase ZnO.

The book by Brandon and Kaplan [1] provides a good background for the theory behind XRD. As a wave of electromagnetic nature, X-rays can interact with electrons in an atom. Diffraction occurs when X-ray waves are scattered by the three dimensional arrays of periodically arranged atoms, the crystal lattice. Constructive interference of scattered waves, which give rise to the diffraction peaks, can only occur when Bragg's relation is satisfied:

$$n\lambda = 2 \cdot d_{hkl} \cdot sin\theta. \tag{2.1}$$

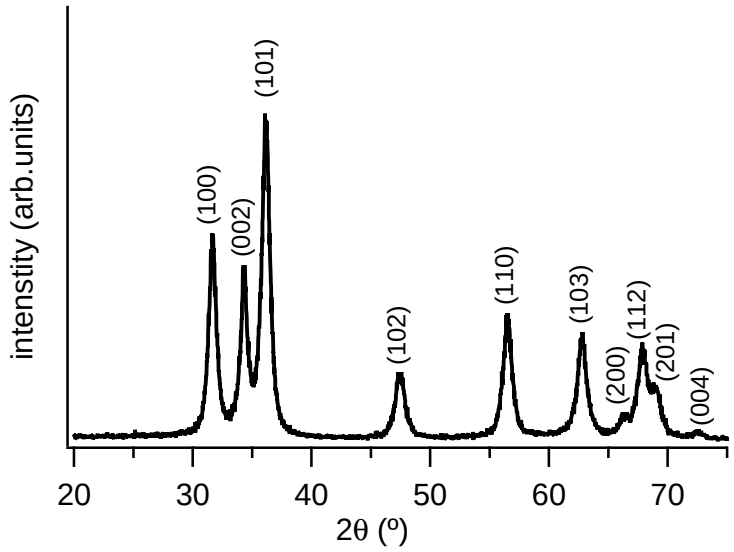

Figure 2.1: Representative XRD plot of a polycrystalline ZnO sample. The peaks are indexed according to the standard pattern JCPDS 36-1451 [2].

Here, n is 1 (first-order diffraction), d_{hkl} is the distance between successive crystal planes (hkl), λ is the X-ray wavelength (1.54 Å for my measurements), and θ is the incident angle. As depicted in Fig. 2.2, for diffraction to happen, the beam path length differences ($2{\cdot}d_{hkl}{\cdot}sin\theta$) between planes must be equal to an integer number of wavelengths ($n\lambda$). The diffraction intensity, on the other hand, is related to electron density within a given family of hkl planes.

In my measurements, the incident X-rays were generated by a Cu Kα source with a wavelength of 1.5406 Å. The diffraction data were collected over a scan range of 20 to 90° in 2θ with a scan speed of 6°/min and a step size of 0.02°. After raw data collection, lattice refinements were performed

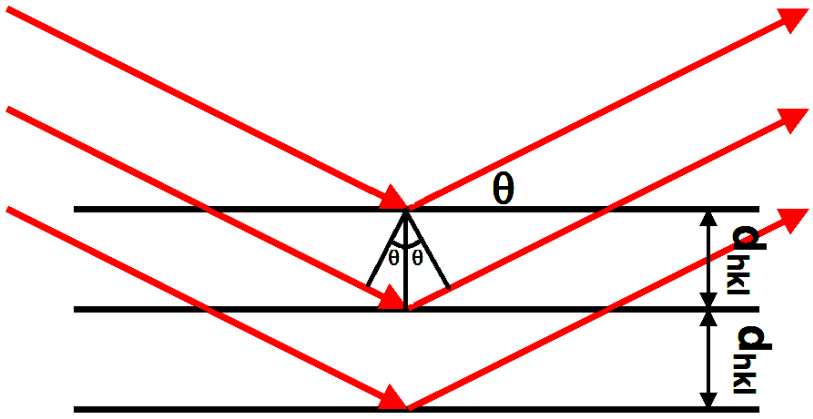

Figure 2.2: Schematic diagram of Bragg's diffraction from crystal planes (hkl) with distance d_{hkl}. For simplicity, the X-ray waves of wavelength λ are presented as arrows.

using Jade software (Materials Data Incorporated [3]) in order to obtain accurate peak indexing and unit cell parameters. The refinement involves a set of treatments, such as peak minimization and background correction [4]. Finally, the crystal phase information was obtained by comparing all peaks positions to a database maintained by the Joint Committee for Powder Diffraction Studies (JCPDS) [2]. The data shown in Fig. 2.1 correspond to the wurtzite ZnO structure, JCPDS 36-1451.

2.1.2 Vibrational spectroscopy

Fourier transform infrared spectroscopy (FTIR) and Raman spectroscopy were also used as supplementary techniques for structural and compositional

characterization. The major purpose of using FTIR on our ZnO samples is to confirm their bulk purities. This is necessary because potential amorphous impurities in a large quantity of ZnO cannot be picked up by XRD. Raman was employed for phase identification of ZnO synthesis products.

FTIR works as a structural characterization tool because changes of dipole moments during vibrations in the specimen will cause it to absorb IR light at distinct wavelengths [5]. An Alpha FTIR spectrometer (Bruker, Billerica, MA, U.S.A.) was used to measure the sample at 4 cm^{-1} resolution. Samples were ground with KBr powder and compressed into disks (7 mm in diameter) before measurement. The purpose of the KBr, which is inert and transparent in the IR region, is to dilute the solid sample to reduce scattering.

Raman spectra were collected with a Renishaw inVia Raman microscope, 830 nm excitation. The Raman effect involves inelastic scattering of light when interacting with optical phonons in solids. To be Raman active, a vibration mode must induce a change in polarizability (the ratio of induced dipole moment to electrical field of incident light). Raman spectroscopy is complementary to IR owing to its sensitivity to vibrations that are not IR active. During a Raman measurement, minimal sample preparation is required besides laying the sample powder on a flat substrate. I used a silica wafer as a substrate due to its low fluorescence interference.

2.1.3 Thermogravimetric analysis

Thermal stabilities of the samples were evaluated by thermogravimetric analysis (TGA). TGA monitors mass loss due to decomposition as the sample is being heated. In this thesis, I used a TGA (Q50 TA instrument, managed by C-CART (CREAIT) at MUN) for investigating thermal decomposition processes of the ZnO synthesis products. Typically, less than 0.1 g of powder sample was placed in a platinum weighting pan which was heated in a furnace with precise temperature control. The plot of TGA results can take many forms, and in this thesis, the mass loss of each sample was plotted as a function of temperature. Moreover, TGA can also give compositional information based on mass loss after thermal decomposition.

2.2 Size characterization

Particle size is one of the most important factors affecting gas sensing behavior of polycrystalline ZnO. It determines surface area and has considerable impact on the electronic and surfaces properties of ZnO. In this thesis, size characterization was performed using several different methods.

2.2.1 Scherrer's estimation from XRD data

Widths of XRD peaks contain crystallite size information, according to Scherrer's equation [6]:

$$L = \frac{K\lambda}{Bcos\theta}. \tag{2.2}$$

Here, L is the crystalline domain, λ is the X-ray wavelength, B is the full width at half maximum (FWHM), θ is the diffraction angle. K is the dimensionless Scherrer constant, a crystallite shape and size distribution related proportionality with a value close to 1 for spherical particles [6].

Caution is required when applying the Scherrer's equation for the crystallite size analysis. The inherent peak broadening, which is caused by instrumental errors, has to be subtracted from the overall peak width. Therefore, a generally accepted range of size for a valid Scherrer's estimation is below 1 μm [6]. In Fig. 2.1, the average crystallite size estimated from the XRD peaks for this ZnO sample is 14 $\pm$ 1 nm.

2.2.2 Scanning electron microscopy

I used scanning electron microscopy (SEM) [7] to image my ZnO samples. An example of a ZnO micrograph with 60000$\times$ magnification is shown in Fig. 2.3. It shows a single, hexagonal bi-pyramid shaped ZnO particle. The micrograph was acquired with a FEI Quanta 400 high resolution field emission scanning electron microscope. Michael Shaffer at CREAIT (Memorial University), helped with image collection. Prior to imaging, my ZnO samples were sputtered with a thin coating of conductive carbon. This treatment is necessary for samples with low conductivities, such as ZnO, since unwanted

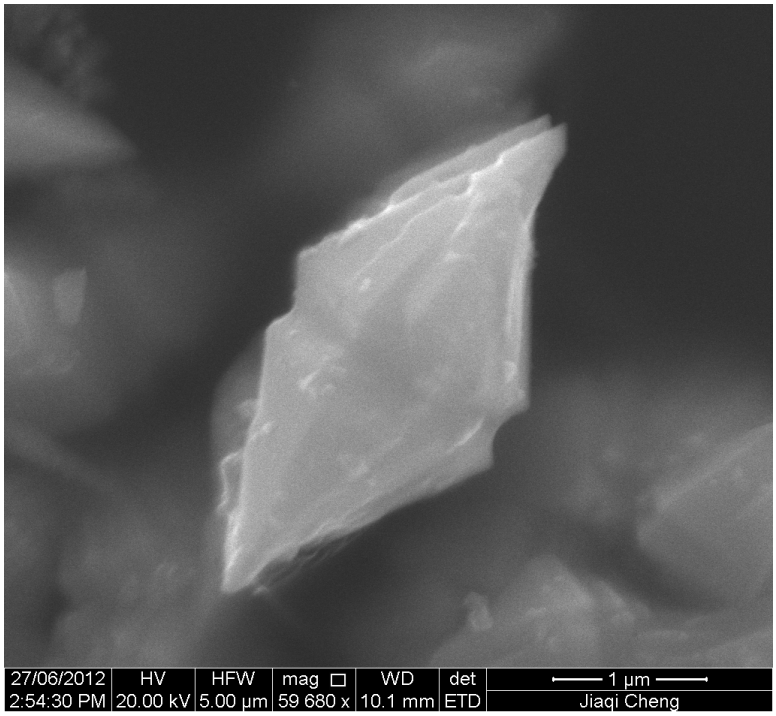

Figure 2.3: Representative SEM micrograph of an hexagonal-bipyramid shaped ZnO particle.

charge accumulation on the sample surface can devastate the image quality and reduce resolution of the image. Additionally, a graphite substrate was used in order to ground the sample. Nevertheless, even with all aforementioned efforts, the resolution was still limited to ~ 100 nm. This means that we did not get clear images for our smallest ZnO particles.

2.2.3 Dynamic light scattering

As a widely used size characterization technique, dynamic light scattering (DLS) takes advantage of Brownian motion of particles suspended in

a fluid [8]. DLS remedies the inadequacy in size assessment using XRD peak width or SEM. For XRD, in addition to the limited applicability of Scherrer's equation, the approximate crystallite size is not necessarily equivalent to the actual particle size because an individual particle often contains multiple crystallites. For SEM, the images obtained for a tiny portion of samples may not reflect the real size distribution of the entire sample. Moreover, limited by the resolution of SEM, ZnO samples with particle sizes smaller than 100 nm can be identified.

One can refer to Chu's book for the science behind DLS [8]. Briefly: when light is shone on a colloidal suspension, the intensity of scattered light fluctuates due to the randomly moving particles in solution. Such intensity fluctuation is then incorporated into a correlation function [8]:

$$G(\tau_a) = \frac{1}{T}\int_0^T I(t)\cdot I(t+\tau_a)\,\mathrm{d}\tau_a \tag{2.3}$$

where $G(\tau)$ is the correlation function, $I(t)$ is the scattered light intensity at a time t, and τ_a is the correlation time that is defined as the time interval with a typical range from hundreds of microseconds to milliseconds. According to this relation, in a Brownian system, the correlation function decays exponentially as the correlation time increases (Fig. 2.4a). The rate of this decay is proportional to particle sizes. It is worth noting that the particle size obtained by DLS represents a hydrodynamic size of particle, which is a spherical approximation.

I ran the DLS measurements using a Malvern Nano S Zetasizer with dual capabilities for DLS analysis and zeta potential measurements. Thanks to Dr. Valerie Booth in the Department of Biochemistry, Memorial University, for providing access to the instrument. The results from DLS are presented in a form of size distribution histogram (Fig. 2.4b). A typical size measurement with this instrument typically requires less than 5 min. Before the measurements, $\sim$ 1 mL of suspension with particle concentration of 50 mg/L was sonicated for at least 30 min, in order to break apart the conglomerates. The ZnO samples were dispersed in acetone as other media caused either severe conglomeration or dissolution of the ZnO particles.

2.3 Surface structure characterization

Gas sensing responses are triggered by gas-surface interactions. Thus, knowing the surface characteristics of ZnO has been a major task in my thesis investigation. I used several surface sensitive techniques to probe various surface features, such as surface area, surface chemical composition, and surface charge. The data obtained from these techniques are informative for deducing mechanisms behind the gas sensing performances by ZnO under various operating conditions.

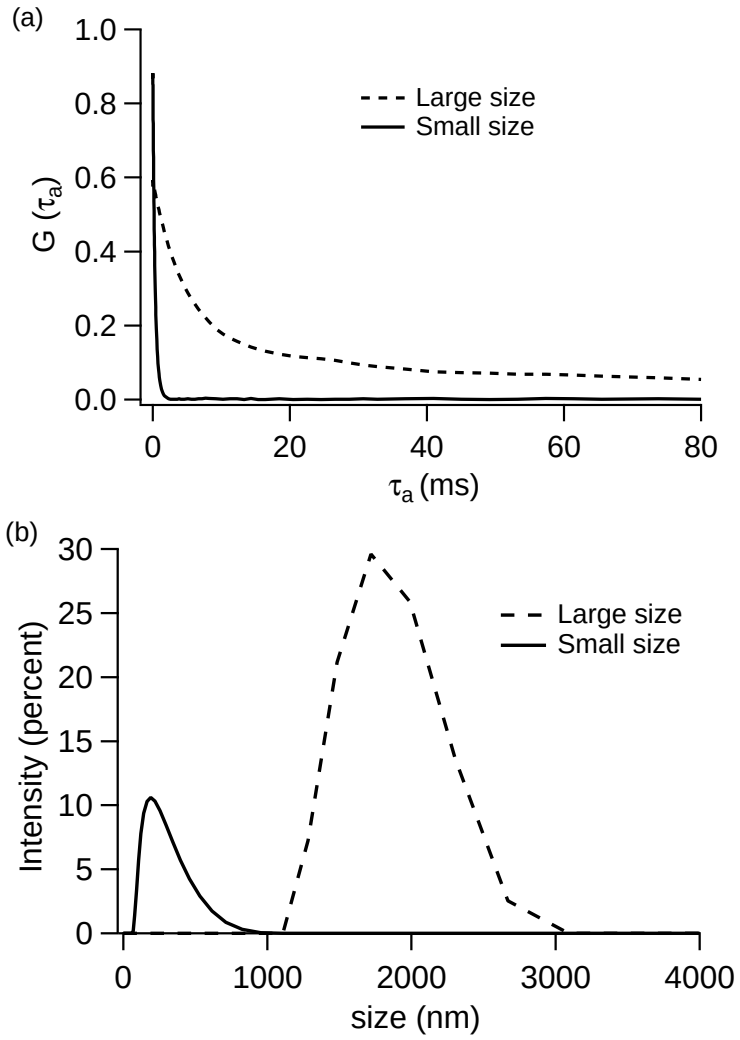

Figure 2.4: (a) Raw correlation function diagram of two ZnO samples with different average particles sizes and (b) the corresponding size distribution histogram.

2.3.1 X-ray photoelectron spectroscopy

Surface composition analysis was performed using X-ray photoelectron spectroscopy (XPS). XPS can provide information about (1) surface elements identities (except for H and He), (2) quantitative concentrations of the elements, and (3) chemical states of the elements [9]. My ZnO samples were sent to Dalhousie University (Halifax, NS, Canada) for XPS measurements. Data collection and preliminary analysis was done by Dr. Zeynel Bayindir with a VG Microtech MultiLab ESCA 2000 instrument.

Peaks show up at different binding energies in a typical XPS plot (Fig. 2.5). Each peak corresponds to electrons dislodged from a core level orbital. For ZnO, the O *1s* and Zn $2p_{3/2}$ electrons give rise to the major peaks on a XPS spectrum, due to high cross section of the emissions from these two orbitals. In Fig. 2.5, shifts of the binding energy for O *1s* peaks indicate different bonding environments for different types of surface oxygen. The peak positions and relative intensities were confirmed through peak fittings using Gaussian functions.

The theory of XPS can be found in van der Heide's book [9]. The predecessor of XPS is the photoelectric effect. When light is absorbed by an atom, electrons would be emitted from the atom if the energy of the incident photon is greater than the binding energy of electron to an atom. The energy difference is then transferred to kinetic energy of the dislodged electron. XPS works according to the same principle in that the interactions between the X-ray photons and the core-level electrons in the atoms would trigger

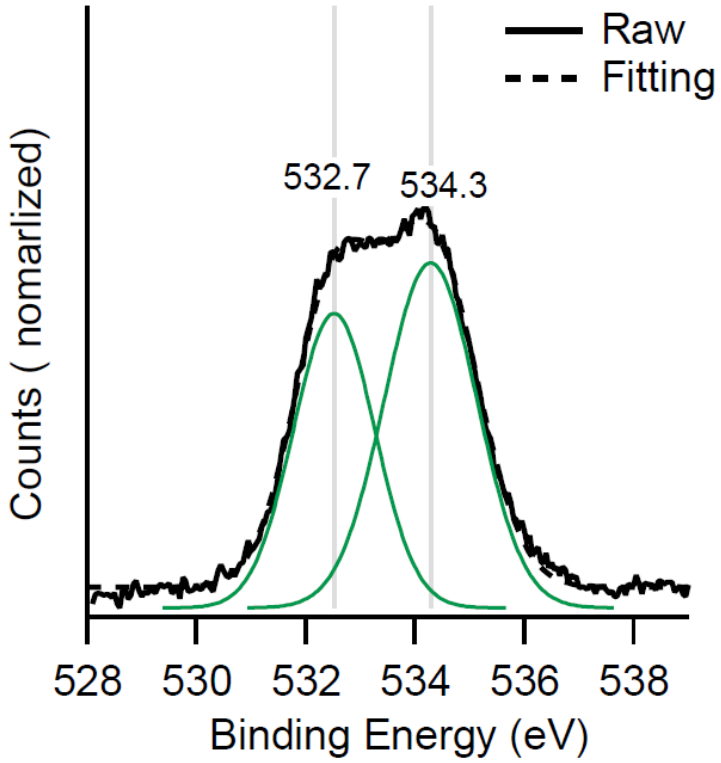

Figure 2.5: Representative XPS peaks showing binding energies related to O *1s* electrons near the ZnO surface. Overlapping peaks are fitted with Gaussian functions. The raw data was collected by Dr. Zeynel Bayindir at Dalhousie University.

emission of electrons from the atoms. Although the penetration depth of X-rays is typically several micrometers, XPS is a true surface sensitive technique because only those photoelectrons close to the sample surface can gain sufficient kinetic energy to escape from the sample and be detected. Hence, XPS reveals information of the sample's surface region with a depth of ~ 5 nm. This makes XPS a superior surface technique to energy-dispersive X-ray spectroscopy (EDX), which is built into in the FE-SEM. EDX has excessive sample penetration depth (≥ 500 nm) induced by the high energy electrons from the scanning electron beam.

2.3.2 Surface zeta potential measurement

Surface charge also holds clues about surface reactivity. Most particulate surfaces are electrically charged when suspended in solution. In general, the particle surface charge in solution could originate from either surface dissolution or adsorption of foreign charged species [10]. One way to quantify the surface charge is to measure zeta potential (ζ), which arises from the charge difference across the diffuse layer [10]. As illustrated in Fig. 2.6, a charged particle surface in solution attracts a thin layer of counter-ions (Stern layer) that travels with the particle. Beyond the outer edge of Stern layer, the ions diffuse across a diffuse/slipping layer into solution bulk where the net charge is zero.

The sign and magnitude of ζ is strongly influenced by several factors, including solution pH, solution ionic strength, as well as functional group at

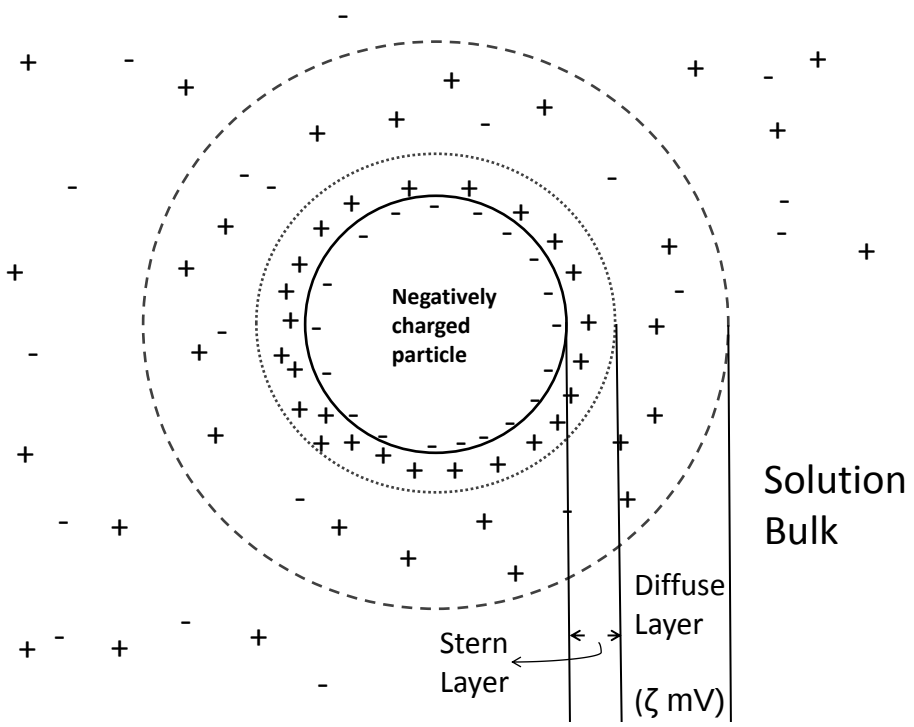

Figure 2.6: Schematic diagram of charge distribution for a negatively charged spherical particle dispersed in solution.

the particle surface. For my uncoated ZnO samples, the ζ investigation was focused on the effects of suspension pH. We found that the ζ of suspended ZnO particles varies with medium pH. At a pH around 9 to 10, the isoelectric point—characteristic to the ZnO surface-solution equilibrium—is reached, where the ζ registers a zero value.

Electrophoresis is the most common method to measure ζ, based on particle mobilities in an electric field. Measurements were done with the same instrument used for DLS analysis (Malvern Nano S Zetasizer). The particle suspensions were prepared by the same procedure as size measurement, except that two parallel metal plates separated by 5 mm were inserted into the suspension. During a measurement, an electrical field was generated by applying a potential (up to 100 V) across the space between the two plates, driving the particles to move. Finally, ζ was computed from the electrophoretic mobility of particles, according to Henry's equation:

$$U_E = \frac{2\epsilon\zeta f(Ka)}{3\eta}. \tag{2.4}$$

Here, U_E is the electrophoretic mobility, ϵ and η are the dielectric constant and viscosity of the medium, respectively. The Henry's function *f(Ka)* is related to the thickness of the Stern layer, which takes a value of 1.5 in my case when large ϵ medium, such as water, is used. In contrast, *f(Ka)* approaches 1 for most non-polar media [11].

2.3.3 Gas adsorption surface area measurement

Surface areas of ZnO samples were assessed by gas adsorption measurements based on Brunauer-Emmett-Teller (BET) theory. BET theory states that material surfaces can adsorb multi-layers of external gaseous molecules; and relative pressure of the gases in the environment after the adsorption is proportional to the specific surface area of the material. This relation leads to BET equation [12]:

$$\frac{1}{v[(p_0/p)-1]} = (\frac{C_{BET}-1}{v_m \cdot C_{BET}})\frac{p}{p_0} + \frac{1}{v_m \cdot C_{BET}} \tag{2.5}$$

where p_0 is the vapor pressure at saturation, p is the actual vapor pressure at the solid-gas equilibrium, v is the adsorbed gas quantity (in this case, volume) and v_m is the volume of adsorbed gas molecules forming monolayer on the solid surface, which gives rise to the surface area, and C_{BET} is the BET constant related to the heat of adsorption.

Samples were sent to Dr. Aicheng Chen's research group at Lakehead University (Thunder Bay, ON, Canada) for N_2 adsorption measurements. Then BET theory was applied to obtain surface areas of the powdered samples. The measurements and BET analyses were done by J. Wen. The results were plotted in the form of $1/v[(p_0/p)-1]$ as a function of p/p_0 with a measurement range $0.1 \leq p/p_0 \leq 0.30$ (Fig. 2.7). This typical range was chosen because a linear relationship in the isotherm is expected in this low pressure region [13]. The values of v_m and C_{BET} can be calculated by finding the slope

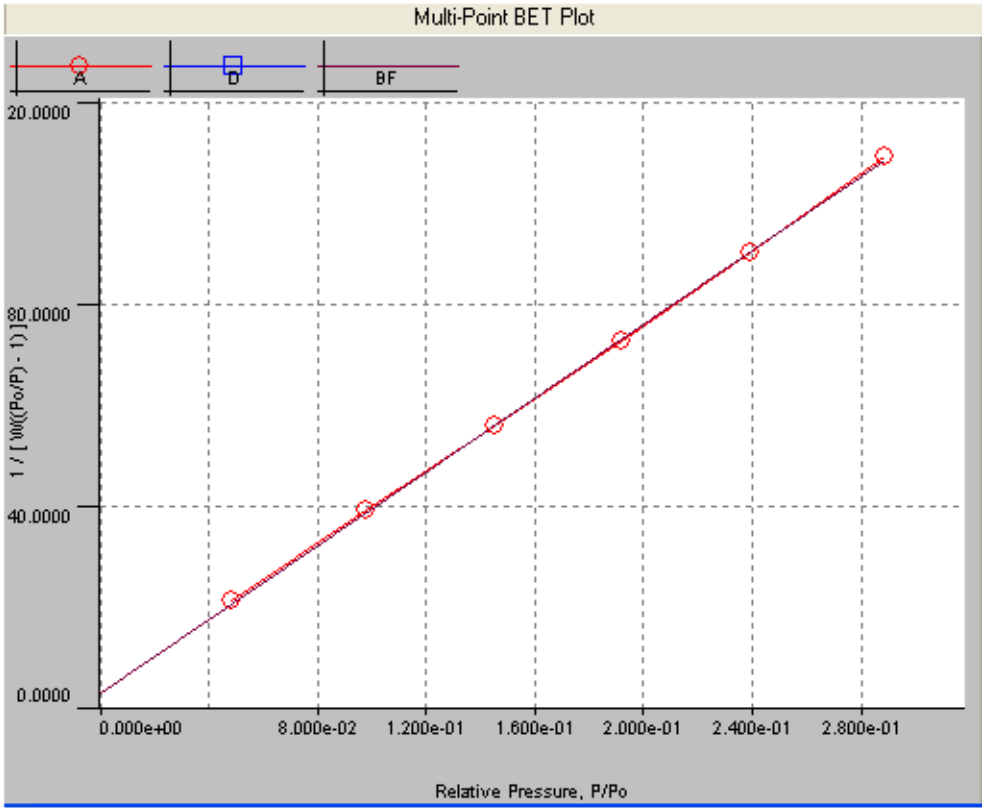

Figure 2.7: Multi-point BET plot of N_2 adsorption for ZnO nanoparticles. Collected and plotted by Dr. Aicheng Chen's research group at Lakehead University.

and intercept from least-square fit. The final surface area was then obtained after correcting the v_m with molecular volume of N_2.

2.4 Electronic properties

After the careful structure, size and surface characterizations, electronic properties of the ZnO particles were investigated. This section provides an overview of the techniques used for the electronic properties study.

2.4.1 Diffuse reflectance spectroscopy

Diffuse reflectance spectroscopy (DRS) measures direct electronic band gap of ZnO. DRS works based on a principle that photon with energies greater than ZnO band gap will be absorbed. The absorption will result in an energy cutoff on a spectrum recording the reflected photons from sample surfaces. Measurements were conducted using a Model DT 1000 CE UV-Visible light source (200-800 nm, Analytical Instrument Systems), in conjunction with an Ocean Optics SD2000 system for data collection and analysis. A reference sample of 100% reflectance was used to calibrate the system before measurement. The band gap energy is often determined according to the absorption edge that is equivalent to the wavelength at which the reflectance spectra starts rising [14] (Fig. 2.8a). However, we use the peak position obtained from the differentiation of the raw reflectance data (Fig. 2.8b) for the band gap value, since the values obtained this way have shown higher consistencies with transmission mode [15].

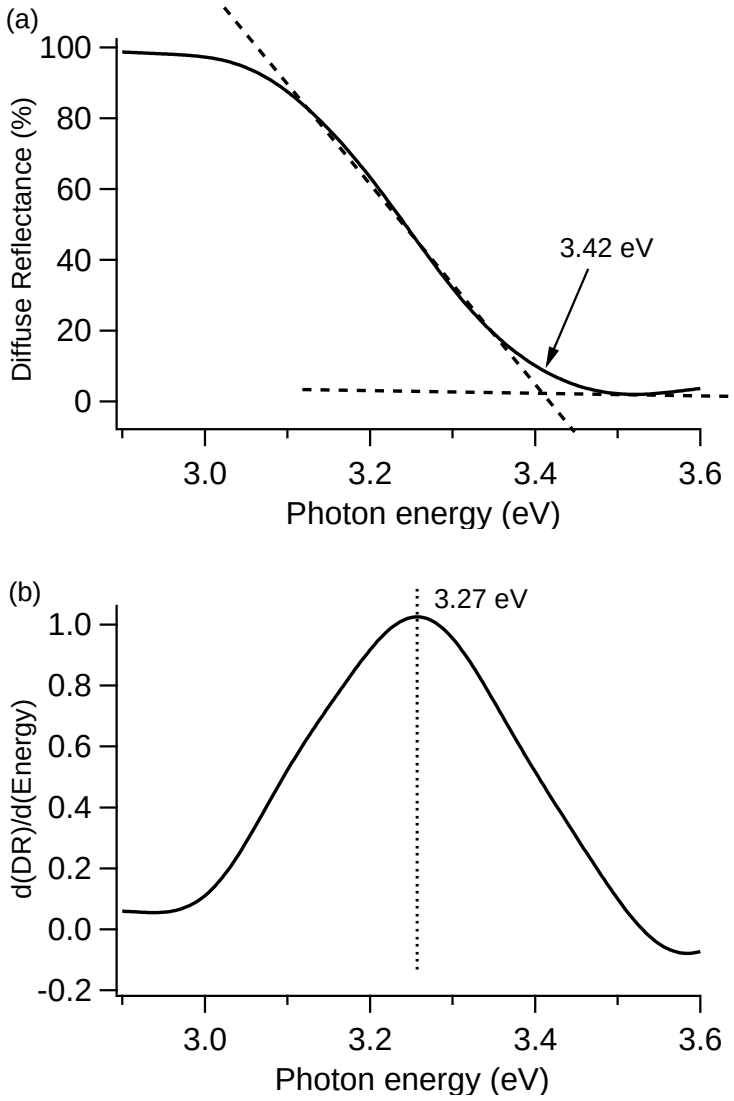

Figure 2.8: (a) Representative UV-Visible diffuse reflectance spectrum of ZnO nanoparticles and (b) corresponding differentiation of the raw spectrum. In (b), the dashed line indicates where the band gap value is extracted.

2.4.2 Current-voltage characteristics of ZnO film

Current (I)-voltage (V) characterization evaluates qualities of the electrodes in contact with ZnO film. An I-V measurement is performed by sweeping a DC potential across ZnO film and recording electrical current. This was done using a Princeton Applied Research (PAR) EG&G Potentiostat (Powersuite interface) or Hokuto Denko HA 501 potentiostat (Labview interface) with sweeping voltage between -2 V to 2 V and a rate of 10 mV/s. The I-V relationship reveals basic electrical behavior—Ohmic or non-Ohmic—of the system. An ideal contact between an electrode and the ZnO film should show an Ohmic behavior such that the current passing through the material increases linearly with the increasing bias, according to Ohm's law:

$$V = IR \tag{2.6}$$

As a result, resistance of an Ohmic system can be obtained from slope of a straight line of the I-V relationship.

In contrast to the Ohmic behavior, any deviation from the linear I-V relation, *i.e.* resistance is not constant when applied potential varies, displays a non-Ohmic behavior which is typical for electronic devices such as diode. I checked for Ohmic behavior as a sign of good contact between my ZnO samples and the electrical measurement devices.

2.4.3 Electrochemical impedance spectroscopy

Beyond *I-V* characterization, a more in depth knowledge of a material's electrical responses can be reached using electrochemical impedance spectroscopy (EIS). EIS is powerful for probing the complex nonlinear process in a system by applying a low-amplitude sinusoid AC potential to the material and monitoring the current-voltage relations as a function of AC frequency.

The basic concept of EIS can be found in the book by Barsoukov and Macdonald [16]. When a sinusoidal potential is applied to sample at steady state, the instantaneous voltage (υ) and current (i) at a certain point of time (t) can be expressed as:

$$i(t) = I_m sin(\omega t + \theta) = I_m \exp(j\omega t - \theta) \tag{2.7}$$

$$\upsilon(t) = V_m sin(\omega t) = V_m \exp(j\omega t) \tag{2.8}$$

where V_m the voltage at maximum amplitude, ω is the angular frequency, I_m is the maximum amplitude of current and θ is the phase difference between current and voltage in radians. The impedance as a function of angular frequency ($Z(\omega)$) is obtained by dividing $\upsilon(t)$ by $i(t)$:

$$Z(\omega) = \frac{V_m \exp(j\omega t)}{I_m \exp(j\omega t - \theta)} = Z \exp(j\omega) = Z(cos\theta + j sin\theta) = Z_{re} + jZ_{im} \tag{2.9}$$

where $Z(\omega)$ is a complex quantity. It is composed of real and imaginary parts that can be expressed in Cartesian form. θ represents the phase shift

between the input voltage and measured current. Z_{re} is the resistance (R). Z_{im} is the reactance (X) that takes negative value in the absence of induction effect and it is inversely proportional to capacitance of the sample.

An EIS spectrum can be represented in various forms. The most commonly used options are Bode and Nyquist graphs. Bode plots show the impedance quantities against frequency so that the frequency dependent-behavior of the quantities under examination can be clearly displayed (Fig. 2.9a). A Nyquist graph, on the other hand, shows the imaginary part of the complex impedance (y-axis) against the real part (x-axis) at various frequencies. As shown in Fig. 2.9b, each point represents Z_{im} and Z_{re} values for the system at a given frequency that decreases from left to right across x-axis. Although visualizing frequency responses may not be easy, Nyquist plot is an useful representation as it displays other key parameters such as $|Z|$ and θ.

Nyquist plots come in handy when modeling the EIS spectra with an equivalent electrical circuit (This was done using freeware EIS Spectrum Analyser [17]). The modeling serves the purpose of decoupling various electrical components (resistor, capacitor) in the non-linear system and helps us deduce the likely physical/chemical origin of electrical responses of the system [16]. For example, a perfect semicircle in the Nyquist plot, as shown in Fig. 2.9b, is characteristic to a simple paralleled RC circuit (Fig. 2.9b insert). The R and C values obtained from the modeling are 87 kΩ and 400 pF, respectively. For a Nyquist plot with shapes deviated from the per-

fect semi-circle, more components should be added into its equivalent circuit. This is demonstrated in Chapter 6.

2.5 Gas sensing measurement

Films made of polycrystalline ZnO were utilized as gas sensors, whose capacitance variations were monitored after exposure to target gases. This section provides details about the gas sensing experiment.

2.5.1 Assembly of sensing film

The films of polycrystalline ZnO were made through a simple drop casting method: a slurry of as-prepared ZnO powder (0.10 g dispersed in 2 mL of acetone and sonicated for 30 s) was slowly poured onto, and spread evenly over a conductive substrate. Various substrates were used including stainless steel strips, aluminum strips (both were mechanically polished to remove the surface oxide layer), and indium tin oxide (ITO) glass slides. Prior to deposition, each substrate was washed several times with ethanol and deionized water, and sonicated for 30 min in deionized water. A sandwich-structured sensor with a ZnO middle layer was constructed: the substrate served as one electrode, and a second substrate of the same material was overlaid on the ZnO film.

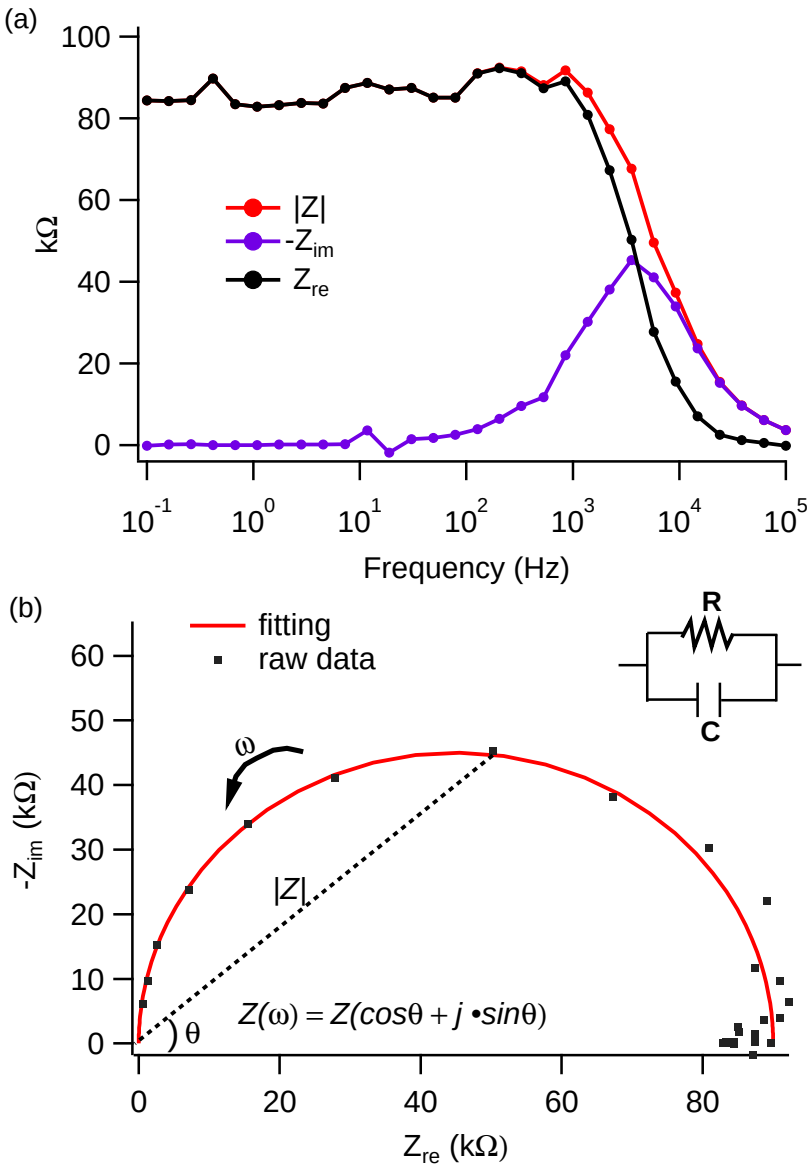

Figure 2.9: (a) Bode and (b) Nyquist representations of EIS spectra for a ZnO film over a frequency range of 10^{-1} to 10^{5} Hz. In (b), the raw data were fitted with a circuit model of a single resistor and capacitor in parallel (insert). The arrow indicates the direction of increasing frequency. The representations of $|Z|$ and θ are also sketched.

2.5.2 Gas testing apparatus

We built a simple room temperature gas testing apparatus, as illustrated in Fig. 2.10. The sensor was placed inside of a sealed (25 cm × 25 cm ×25 cm) chamber. Electrical connections were made between the sensor and a inductance-capacitance-resistance (LCR) meter (National Instruments) that was located outside the chamber. Prior to use, relative humidity (RH) levels inside of the test chamber were controlled and modified using different saturated salt solutions. This was done by placing 150 mL of saturated salt solution in the chamber because each saturated salt solution yields a distinct and characteristic relative humidity at 22 °C: CH_3CO_2K (20 ± 2%), K_2CO_3 (45 ± 2%), or KNO_3 (90 ± 2%) [18]. Before initiating the gas detection measurements, one of the aforementioned salt solutions was kept in the chamber for 2 h to reach the intended equilibrium RH.

Gas sensing experiments were also conducted at high temperatures (100 °C to 500 °C). To construct a high temperature gas testing system, aluminum plates were used to make electrical contacts with the ZnO sensing layer. The sensor was placed in a tube furnace (Lindberg/Blue 1500 °C, Thermo Scientific) with programmable temperature. At elevated temperatures, humidity levels in the tube were not deliberately controlled and were assumed to be near 0 RH.

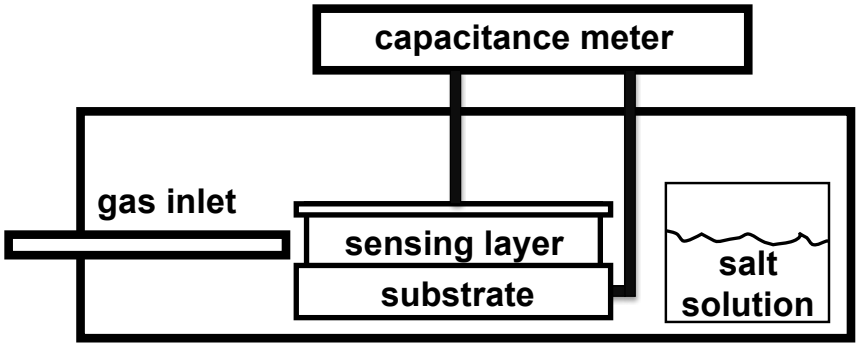

Figure 2.10: Schematic diagram of the humidity-controlled sensing experiments (not drawn to scale) operated at room temperature.

2.5.3 Gas concentration calibration

Target gas was collected from vapor above the liquid of the analyte with a syringe. The concentration (mole fraction) of gas was estimated through partial vapor pressure of the pure analyte under ambient condition. For example, to collect ethanol vapor, 10 mL of anhydrous ethanol liquid was sealed in a 50 mL flask. Assuming the gas molecules behave ideally, we estimated the mole fraction of the ethanol vapor inside the flask according to Dalton's law [19]:

$$n = \frac{p}{p_0}. \tag{2.10}$$

Here, p is the vapor pressure of ethanol (5.95 kPa at 22 °C) and p_0 is the atmospheric pressure (1 atm = 101.325 kPa), and n is the mole fraction ($\sim$ 0.06) of ethanol vapor. Further dilution of the analyte vapor was achieved by drawing air into the syringe. Using this method, the humidity level of the target gas was also controlled by mixing the vapor with air of various

humidities.

Although this method of gas concentration determination does not provide high precision, stable sensing responses were achieved to various gases calibrated by this method (Chapter 4 [20] and Chapter 5). It is also worth noting that our vapor pressure based method is a more conservative way for gas concentration estimation than some methods adopted by others [21]. For example, in an experiment by Zhou *et al.*, a drop of ethanol liquid was evaporated in a seal chamber, and the gas concentration was assumed as a ratio of the liquid volume to the volume of the chamber [21]. Nevertheless, we believe that directly using the volume of a liquid analyte to approximate the gas concentration is a vast overestimate because the liquid volume is greatly smaller than the volume of same number of molecules in gas phase.

2.5.4 Target gas exposure

Room temperature sensing experiments were initiated by injecting 20 mL of target gas mixture into the chamber in close proximity to the sensing film. Given the large chamber volume relative to that of the injected gas, multiple injections could be executed without interference from one injection to the next. For high temperature gas sensing, 100 mL of target gas was injected into the tube placed in the furnace, then the gases were released by opening the ends of the tube. Sensing responses for the ZnO films were assessed by measuring capacitance changes at 3 kHz with an applied AC RMS voltage of 50 mV at zero bias (National Instruments LCR meter with

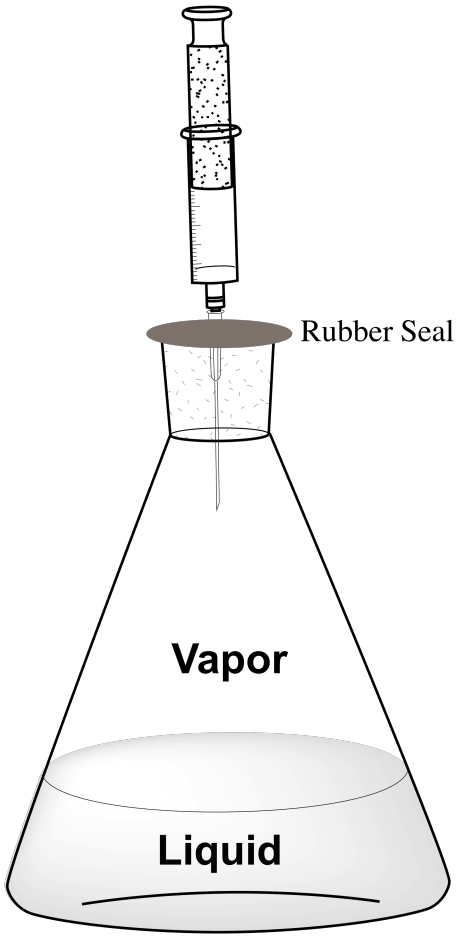

Figure 2.11: Schematic diagram depicting the vapor collection process.

PXI-1033 interface).

Bibliography

[1] D. Brandon and W.D. Kaplan. *Microstructural Characterization of Materials*. John Wiley: New York, US, 2013.

[2] Powder Diffraction File Joint Commission on Powder Diffraction Standards – International Centre for Diffraction Data, 2003.

[3] http://www.materialsdata.com. Materials Data, Inc., 2014.

[4] V. Pecharsky and P. Zavalij. *Fundamentals of Powder Diffraction and Structural Characterization of Materials, Second Edition*. Springer: New York, US, 2008.

[5] B. C. Smith. *Fundamentals of Fourier Transform Infrared Spectroscopy*. Taylor & Francis: Abingdon, UK, 1995.

[6] J. I. Langford and A. J. C. Wilson. Scherrer After Sixty Years: A Survey and Some New Results in the Determination of Crystallite Size. *J. Appl. Cryst.*, 11:102–113, 1978.

[7] Joseph I. Goldstein, Dale E. Newbury, Patrick Echlin, David C. Joy, Charles E. Lyman, Eric Lifshin, Linda Sawyer, and Joseph R. Michael. The SEM and Its Modes of Operation. In *Scanning Electron Microscopy and X-ray Microanalysis*, pages 21–60. Springer US, 2003.

[8] B. Chu. Dynamic Light Scattering. In *Soft Matter Characterization*, pages 335–372. Springer Netherlands, 2008.

[9] P. van der Heide. *X-ray Photoelectron Spectroscopy: An introduction to Principles and Practices*. John Wiley: New York, US, 2011.

[10] Jeffrey D. Clogston and Anil K. Patri. Zeta Potential Measurement. In *Characterization of Nanoparticles Intended for Drug Delivery*, volume 697 of *Methods in Molecular Biology*, pages 63–70. Humana Press, 2011.

[11] R. J. Hunter. *Zeta Potential in Colloid Science: Principles and Applications*. Colloid science. Academic Press: San Diego, US, 1988.

[12] G. Fagerlund. Determination of Specific Surface by the BET Method. *Matériaux et Construction*, 6(3):239–245, 1973.

[13] R. B. Anderson. Introduction to The Physical Chemistry of Ceramic Surfaces. *Trans. Brit. Ceram. Soc.*, 3:423, 1966.

[14] D. Gal, Y. Mastai, G. Hodes, and L. Kronik. Band Gap Determination of Semiconductor Powders via Surface Photovoltage Spectroscopy. *J. Appl. Phys.*, 86(10):5573–5577, 1999.

[15] Tingting Ren, Holly R. Baker, and Kristin M. Poduska. Optical Absorption Edge Shifts in Electrodeposited ZnO Thin Films. *Thin Solid Films*, 515:7976–7983, 2007.

[16] E. Barsoukov and J.R. Macdonald. *Impedance Spectroscopy: Theory, Experiment, and Applications*. John Wiley: New York, US, 2005.

[17] Bondarenko A. S. and Ragoisha G. A. *In Progress in Chemometrics Research*. Nova Science: New York, US, 2005.

[18] L. B. Rockland. Saturated Salt Solution for Static Control of Relative Humidity Between 5°C and 40 °C. *Anal. Chem.*, 32:1375–1376, 1960.

[19] P. Atkins and J. de Paula. *Atkins' Physical Chemistry*. OUP Oxford, 2010.

[20] Jiaqi Cheng, Muhammad Asim Rasheed, and Kristin M. Poduska. Exploiting Water-Mediated Ethanol Sensing by Polycrystalline ZnO at Room Temperature. *ECS J. Solid State Sci. Technol.*, 2(1):Q23–Q26, 2013.

[21] Xiaoyan Zhou, Jianpeng Li, Ming Ma, and Qingzhong Xue. Effect of Ethanol Gas on the Electrical Properties of ZnO Nanorods. *Physica E*, 32:1056–1060, 2011.

Chapter 3

Ambient Degradation of ZnO Powders: Does Surface Polarity Matter?

Reproduced with permission from The Electrochemical Society [1].

3.1 Abstract

Comparing different synthesis methods to investigate ambient degradation differences among ZnO crystals with different crystal habits, we examined the effects of particle size, surface area, shape (surface polarity), and zeta (surface) potential. Neither surface polarity nor surface area, on their own, can account for the differences in the surface carbonation among differently

synthesized ZnO samples. Our results demonstrate that surface dissolution and carbonation tendencies must be considered together, in the context of surface polarity, to explain different propensities toward degradation in ZnO powders.

3.2 Introduction

The surface reactivity of ZnO makes this material appealing for technological applications such as UV photodetection and electrical sensors [2, 3], but it also makes it prone to instability and degradation over the long-term. This aging problem can have a strong adverse effect on the material's optical, electrical, and mechanical properties [4, 5], and it is especially pronounced in materials with high surface area [6]. Even though there is a large body of literature related to tailoring the size and morphology of ZnO toward enhanced functionality, very few studies have investigated how these factors affect the material's long term stability.

When ZnO is immersed in water, a soluble $Zn(OH)_2$ layer is formed on the particle surface *via* chemisorption or physisorption of hydroxyl [7, 8]. The rate of ZnO dissolution is then controlled by the equilibrium established between $Zn(OH)_{2(s)}$ and species (*e.g.* $Zn^{2+}{}_{(aq)}$, $Zn(OH)^{+}{}_{(aq)}$ depending on pH) in the solution phase. A generally accepted trend is that the particle dissolution rate increases with reduced particle size due to increasing surface area [4]. However, to our knowledge, no study has taken into account the

particle shape effect on the dissolution rate.

The ambient instability of ZnO is also well-known in the context of corrosion studies on galvanized metallic zinc coatings [9–11]. The oxidation layer of ZnO that forms on a Zn metal surface can react readily with ambient CO_2, moisture, and other airborne gaseous species. It is generally accepted that Zn corrosion involves surface dissolution of ZnO due to a thin surface water layer that is acidified by dissolved atmospheric CO_2. This dissolution and carbonation sequence converts ZnO into $Zn_5(OH)_6(CO_3)_2$ (hydrozincite, abbreviated here as ZHC). This ZHC layer is electrically insulating, unlike the semiconducting behavior of its ZnO precursor.

Despite its role in metal corrosion, there are few atmospheric degradation studies of ZnO. Several recent reports focused on the stability of high-temperature-grown nanowires [12, 13]. After prolonged exposure to humidity and CO_2, ZHC bunches were first observed in electron microscopy studies of thermally deposited ZnO nanowires. Subsequently, second harmonic generation spectroscopy on similarly prepared samples showed the growth patterns of ZHC forming on single ZnO nanowires [13]. There remains a lack of data on the degradation tendencies of ZnO prepared by liquid-based methods, at lower temperatures, and/or with other crystal habits, even though there are numerous reports of new synthesis methods for more economical synthesis of ZnO by using these strategies.

One factor that makes nanowires different from other shapes of ZnO crystallites is that this morphology tends to expose predominantly non-polar

faces, as shown schematically in Fig. 3.1. Rod-shaped ZnO is regarded as the most stable shape of ZnO because of its many low energy non-polar facets [14]. In contrast, for a pyramid shaped particle all facets exposed on ZnO pyramid are high-energy polar surfaces.

In this work, we explore the role that surface polarity can play in regulating surface carbonation in ZnO powders, since the presence of an electrically insulating carbonate can have dire consequences for using ZnO in electronic or optical device applications. Different synthesis methods facilitate our investigation of ambient degradation rates of bare ZnO crystallites with different crystal habits, examining factors including particle size, surface area, shape (surface polarity), and zeta potential. Our results demonstrate that surface dissolution and carbonation tendencies are closely linked in ZnO, while surface area and polarity alone are not necessarily the most diagnostic parameters for predicting degradation tendencies.

3.3 Experimental

3.3.1 Synthesis

We utilized several distinct synthesis strategies to produce either faceted or mixed polarity (irregularly shaped) crystallites, while avoiding organic surfactants and other surface stabilizers. All reagents were analytical grade and used as received.

Predominantly polar-faceted **MS-ZnO** particles with pyramid shapes

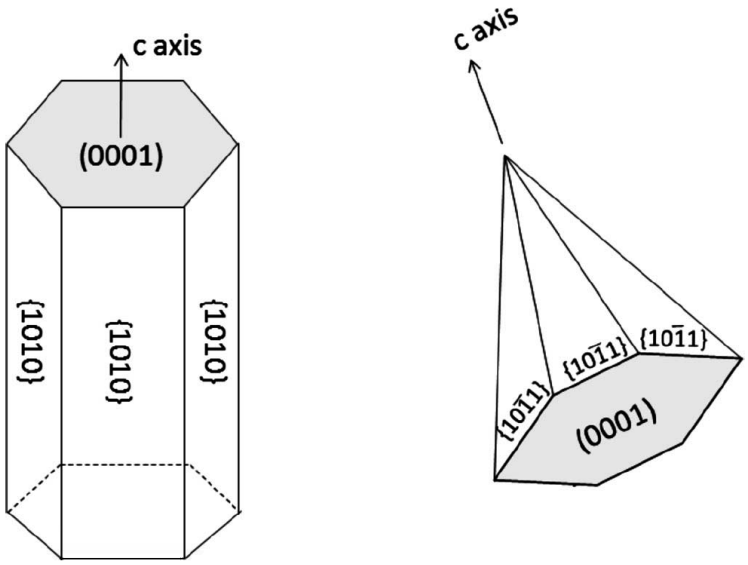

Figure 3.1: Schematic illustration of different polar and non-polar faces for ZnO. The conventional hexagonal rod (left) has many low energy (1010) non-polar facets exposed, while the hexagonal pyramid shape (right) presents polar (10$\bar{1}$1) facets. In both illustrations, the basal face is polar (0001).

were prepared by a molten-salt-assisted route, adapted from methods reported by others [15, 16]. In our experiments, $Zn(O_2CCH_3)_2 \cdot 2\,H_2O$ (Caledon) at 1 mmol was mixed well with 0.1 mol of $LiNO_3$ (Aldrich) in an alumina crucible for $\sim$ 6.5 g total mass. The mixture was heated in air at 500 °C for 1 h, then removed from the oven and cooled in air. Excess $LiNO_3$ was removed by washing and filtering the products many times with ultrapure water until the filtrate pH approached 7.

Predominantly non-polar-terminated **MA-ZnO** particles were rod-like, and were prepared using a solvent-free solid-state metathesis reaction [17] followed by annealing. In powder form, NaOH (EM Science) and $ZnCl_2$ (Caledon) salts were ground together in 2:1 ratio. A self-sustained exothermic reaction that produced ZnO was triggered after about 2 min of grinding. The byproducts were removed by intensive washing and filtering with ultrapure water until the pH of the filtrate approached 7. The remaining product was then oven-dried at 85 °C in air and then heated for 8 h in air at 500 °C, which is well below the melting point of ZnO (2248 K).

Irregularly shaped **M-ZnO** particles were prepared identically to the MA-ZnO particles described above, but without the annealing step.

Smaller-sized irregularly shaped **ST-ZnO**, was prepared solvothermally by refluxing 50 mM $Zn(O_2CCH_3)_2 \cdot 2\,H_2O$ (Caledon) with 50 mM NaOH (EM Science) in ethanol for 6 h at 80 °C, adapted from a method reported by others [18]. The resulting white precipitate was washed several times with ultrapure water and separated *via* centrifugation before oven-drying at 85

°C in air.

3.3.2 Material characterization

Crystalline phases and their average domain sizes were assessed by powder X-ray diffraction (PXRD; Rigaku Ultima IV X-ray diffractometer with Cu Kα at 3°/min, step size 0.02°; lattice constant refinements from Jade software (Materials Data Inc.)) and compared with JCPDS [19] data. Particle size distributions were also measured with dynamic light scattering (DLS; Malvern Nano S Zetasizer, measurement range: 0.3 nm to 10.0 μm). Particles shapes were determined from scanning electron microscopy images (SEM, FEI Quanta 400). The surface areas of the samples were evaluated by the Brunauer-Emmet-Teller (BET) method at a relative pressure ratio of 0.1-0.35. The band gaps of the samples were examined with Diffuse Reflectance Spectroscopy (DRS) using a Model DT 1000 CE UV-Visible light source (200-800 nm, Analytical Instrument Systems), joining with an Ocean Optics SD2000 system.

Surface compositions for fresh samples were investigated with X-ray Photoelectron Spectra (XPS) data collected with a VG Microtech MultiLab ESCA 2000. Zeta potentials were measured in aqueous solutions: 5% v/v of freshly made ZnO samples were immersed in ultrapure water that had been prepared at either an initial pH 5 (using HCl) or initial pH 11 (using NaOH). The suspensions were sealed and then magnetically stirred for 24 h and sonicated for 1 h prior to measurements (Malvern Nano S Zeta-

Approach (label)	Size (nm)	Surface area (m^2g^{-1})	mean size change (%)
Molten-salt-assisted (MS-ZnO)	1000±500	4.2±0.3	-10 ± 2
Annealed metathesis (MA-ZnO)	400±100	2.8±0.3	-15 ± 5
Metathesis (M-ZnO)	100±50	3.4±0.3	-90 ± 20
Solvothermal (ST-ZnO)	20±10	9.4±0.3	-50 ± 10

Table 3.1: Comparisons of ZnO sizes (from DLS data) and surface areas (from BET measurements), and changes to mean particle size after exposure to acidic solution (pH 5).

sizer). The pH of solution changes immediately after the addition of ZnO particles, and stabilizes at a new value after a few hours. We refer to this stabilized value as the aged pH. The aged pH values of the suspensions were also recorded. Qualitative assessments of sample dissolution were compared through the hydrodynamic diameters of particles equilibrated under acidic conditions and alkaline conditions.

3.4 Results and Discussion

3.4.1 Bulk characterization

XRD data (Fig. 3.2) show that all of the different synthesis methods yield ZnO as the only crystalline product. In each case, all diffraction peaks can be indexed to wurtzite-type ZnO (JCPDS 36-1451) and no secondary phase is present. However, the particle sizes and morphologies are quite different among the four different products, as shown in Fig. 3.3 and summarized in Table 3.1.

The molten-salt-assisted growth (MS-ZnO) produced the largest particles,

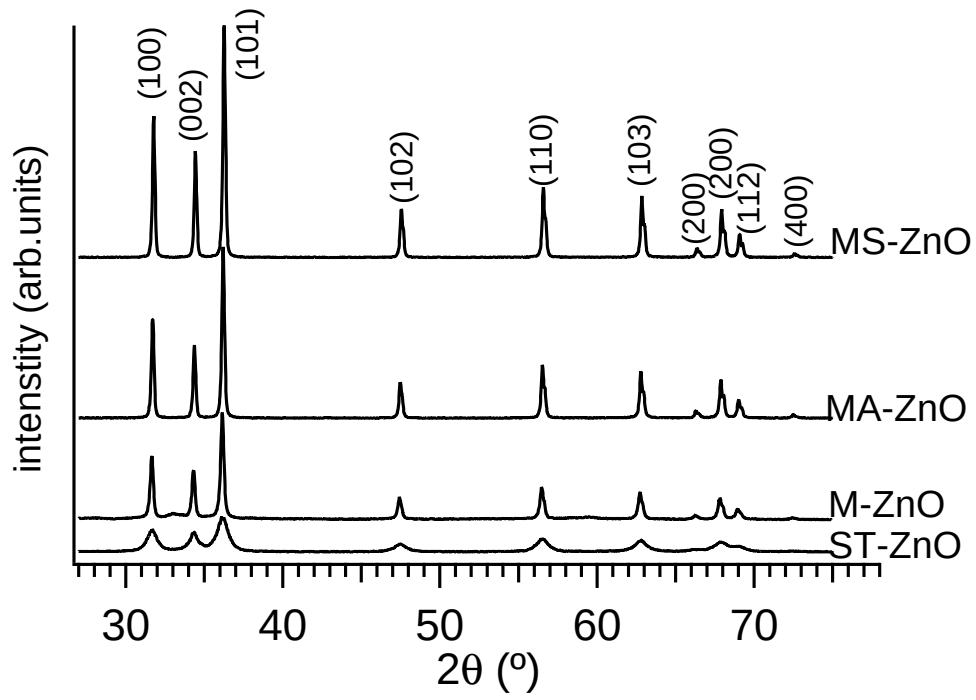

Figure 3.2: Representative XRD data for ZnO prepared by four different synthesis methods. In each case, all diffraction peaks can be indexed to wurtzite-type ZnO (JCPDS 36-1451).

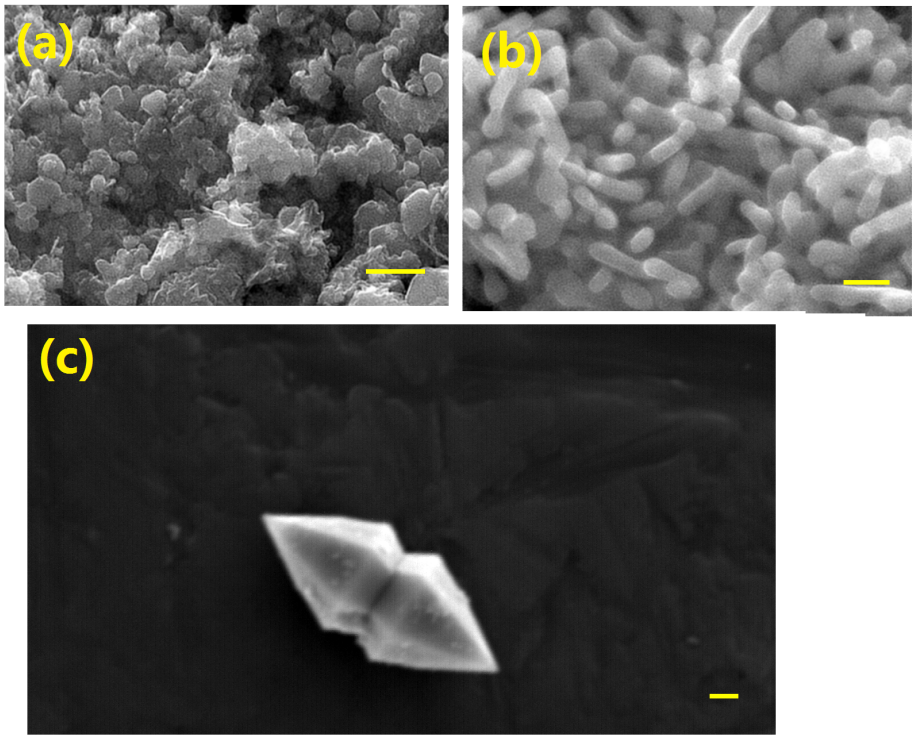

Figure 3.3: Representative SEM images of freshly made (a) M-ZnO (b) MA-ZnO and (c) MS-ZnO with distinct shapes. In each image, the scale bar represents 200 nm.

exhibiting hexagonal pyramid shapes that were often twinned at the base (Fig. 3.3c). Others have suggested that the excess Li^+ present in the molten salt during crystallite growth can electrostatically passivate the polar $10\bar{1}1$ faces to slow their growth rate, since heating in the absence of molten $LiNO_3$ yields a conventional rod shape.

The metathesis-produced M-ZnO has irregular crystallite shapes (Fig. 3.3a), which is not surprising in light of its extraordinarily fast crystallization time ($\sim$ 1 min). Others have attributed irregular particle shapes to the lack of solvent in this solid-state method that would promote diffusion-related crystal ripening [20]. After annealing, the MA-ZnO particle size increases relative to M-ZnO, and it also transforms into a rod-like shape (Fig. 3.3b).

Solvothermal methods (ST-ZnO) produce the smallest particles (20 $\pm$ 10 nm), based on DLS data and Scherrer analyzes of XRD peak widths (Table 3.1). This method of refluxing zinc salts and OH^- in an alcoholic medium is one of the most commonly employed methods for making ZnO nanocrystals [18, 21–24]. The lower solubility of the precursor salts (such as $ZnCl_2$ or $Zn(O_2CCH_3)_2 \cdot 2\,H_2O$) in alcohol relative to aqueous media would presumably lead to both faster nucleation and slower ripening, but this has not yet been studied in detail [14].

3.4.2 Surface characterization: short-term degradation

XPS reveals information of the surface compositions of freshly made samples (Fig. 3.4). Gaussian fits to the O 1*s* spectra (Fig. 3.4a) yield up to three

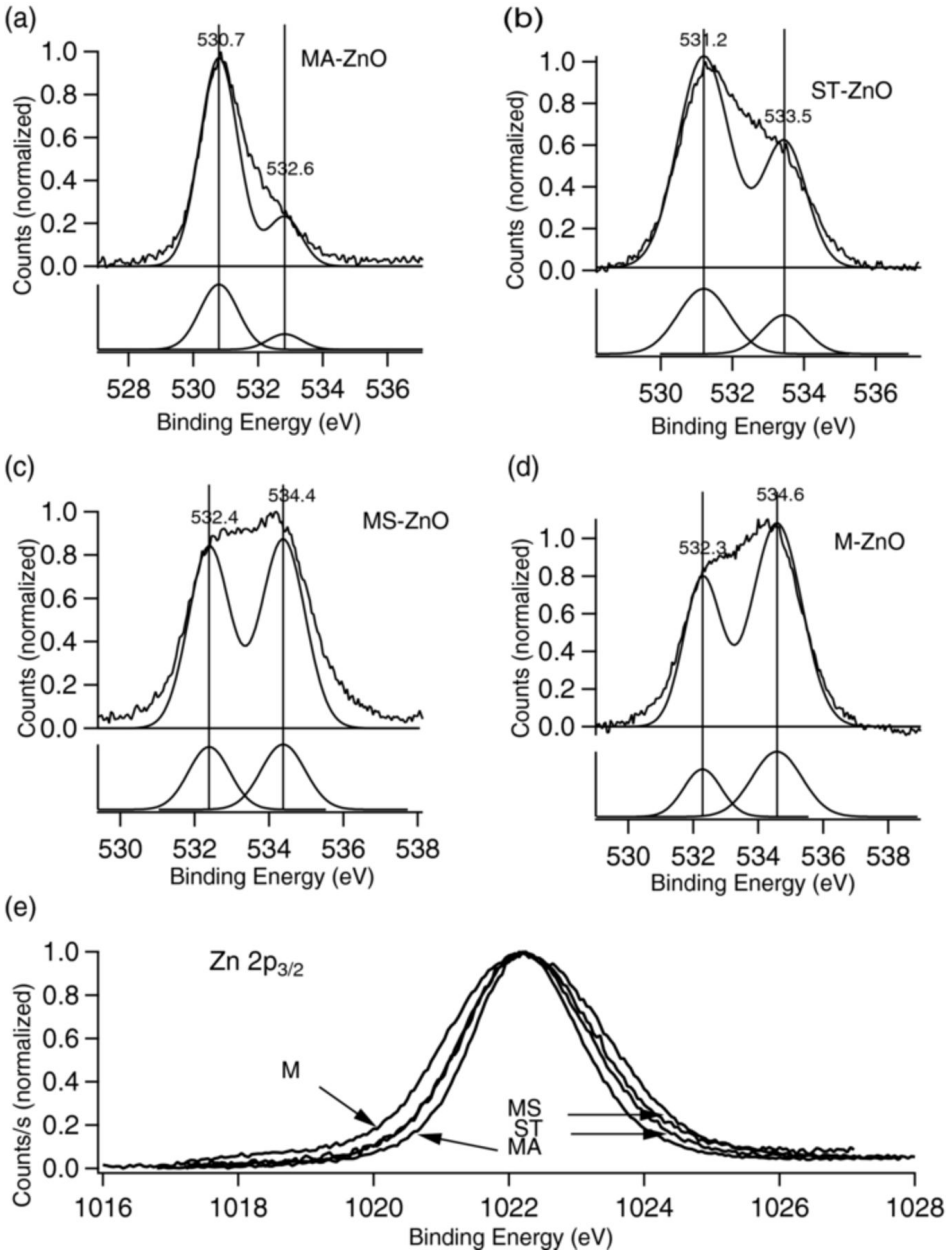

Figure 3.4: XPS data for (a,b,c,d) O 1s, and (e) Zn $2p_{2/3}$ for fresh ZnO synthesized by different methods.

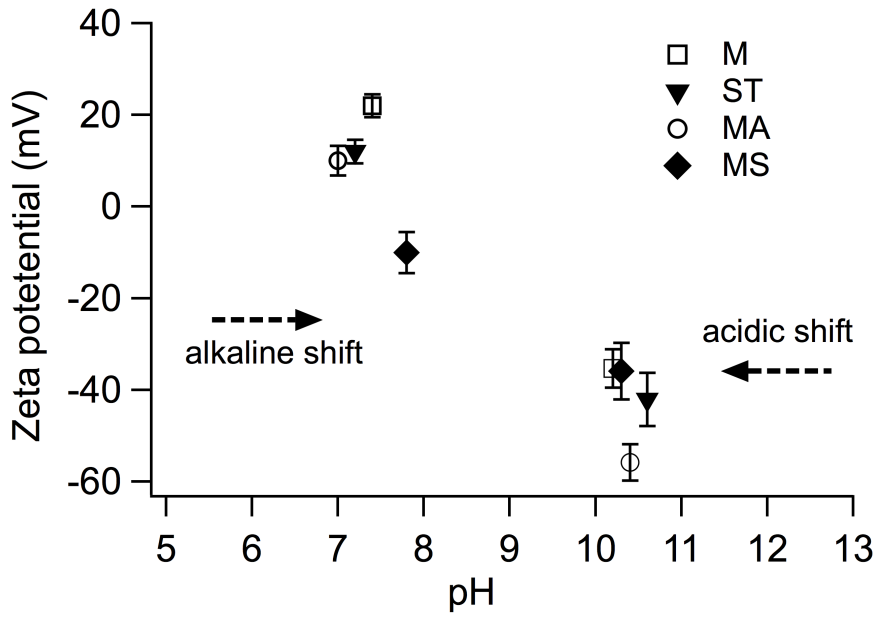

Figure 3.5: Zeta potentials of ZnO samples with respect to solution final pHs drifted from preset value at pH=5.0 and pH=11.0, the arrows indicate direction of pH drift.

peaks: 530.7 eV corresponds to lattice O in ZnO, 533 eV is due to O from surface hydroxides (OH), and the peak at 534 eV is from O from carbonate species [25]. No evidence of carbonates was present for either MA-ZnO or ST-ZnO. The Zn $2p_{2/3}$ peak was centered on 1021.7 eV to correspond with the usual 2+ oxidation state for Zn [26]. There were slight variations in the peak width for Zn $2p_{2/3}$, with M-ZnO the largest and ZnO-MA the narrowest.

To probe surface differences in an aqueous environment, the zeta potential for each kind of ZnO preparation was measured as a function of aged pH of the suspensions (Fig. 3.5). There are two distinct groupings. Suspensions

that started with pH 11 showed only slight increases in acidity with aging (pH $\geq$ 10) and had large negative zeta potentials (-40 to -60 mV). These large zeta potentials are consistent with earlier reports that have shown that ZnO displays good colloidal stability at alkaline pH values [8]. However, suspensions with an initial pH =5 aged to considerably more alkaline values (6.5–7.5) and displayed positive zeta potentials with smaller magnitudes (+10 for most, with M-ZnO at +22 mV). The lone exception to this trend is MS-ZnO, which shows a negative zeta potential that is uncharacteristic for ZnO (whose isoelectric point ranges from 8.5 to 10.5). This anomaly is likely due to surface carbonation: XPS data (Fig. 3.4) shows clear evidence of this in MS-ZnO, and carbonates such as ZHC have been reported to have a negative zeta potential in this pH range [27].

The pH shifts in aged suspensions are a result of different degrees of surface dissolution to equilibrate with the aqueous environment. A qualitative comparison of the relative dissolution tendencies emerges by comparing the mean hydrodynamic particle sizes after equilibrating in either the acidic (initial pH 5) or basic (initial pH 11) water (Table 3.1). In all cases, the mean particle size from more alkaline suspensions is consistent with the particle sizes extracted from XRD peak widths. Also true in all cases is that the more acidic suspensions show smaller particle sizes, as expected. However, there is considerable variability in the extent of the size reduction, with the most severe dissolution occurring for M-ZnO.

3.4.3 Long-term atmospheric carbonation

To investigate the long-term ambient carbonation of ZnO, 200 mg of each sample was placed in a sealed chamber (500 mL volume) with opaque walls to prevent photolysis [5]. The relative humidity (RH) inside the chamber was maintained at 93 ± 2% at 22 °C with the equilibrium vapor pressure of a saturated KNO_3 solution [28]. High CO_2 concentrations were achieved by sublimating 50 mg of dry ice in the chamber. All samples were stored under high humidity and CO_2 conditions for 2 weeks prior to the degradation assessments. The degradation products were assessed with Fourier transform infrared spectroscopy (FTIR; Alpha spectrometer (Bruker, Billerica, MA, U.S.A.) at 4 cm^{-1} resolution on powdered samples dispersed in a 7 mm diameter KBr pellet). FTIR is an effective method to assess the extent of ZnO carbonation because it identifies both crystalline and poorly crystalline phases, without introducing heating effects that could alter the atmospheric carbonation product. Separate thermal decomposition experiments were conducted with a Q500 thermogravimetric analyzer (TA Instruments, New Castle, DE, U.S.A.) using a Pt pan to 600 °C at 20.00 °C/min under 40.0 mL/min N_2 gas flow).

The differences in short-term carbonation and dissolution that appear in XPS data (Fig. 3.4 and DLS data (Table 3.1)) are amplified when long-term degradation changes are monitored. Fig. 3.6a shows representative FTIR spectra for freshly made samples. With all four syntheses, only the Zn-O lattice modes (a broad peak near 450 cm^{-1}) are apparent, which is

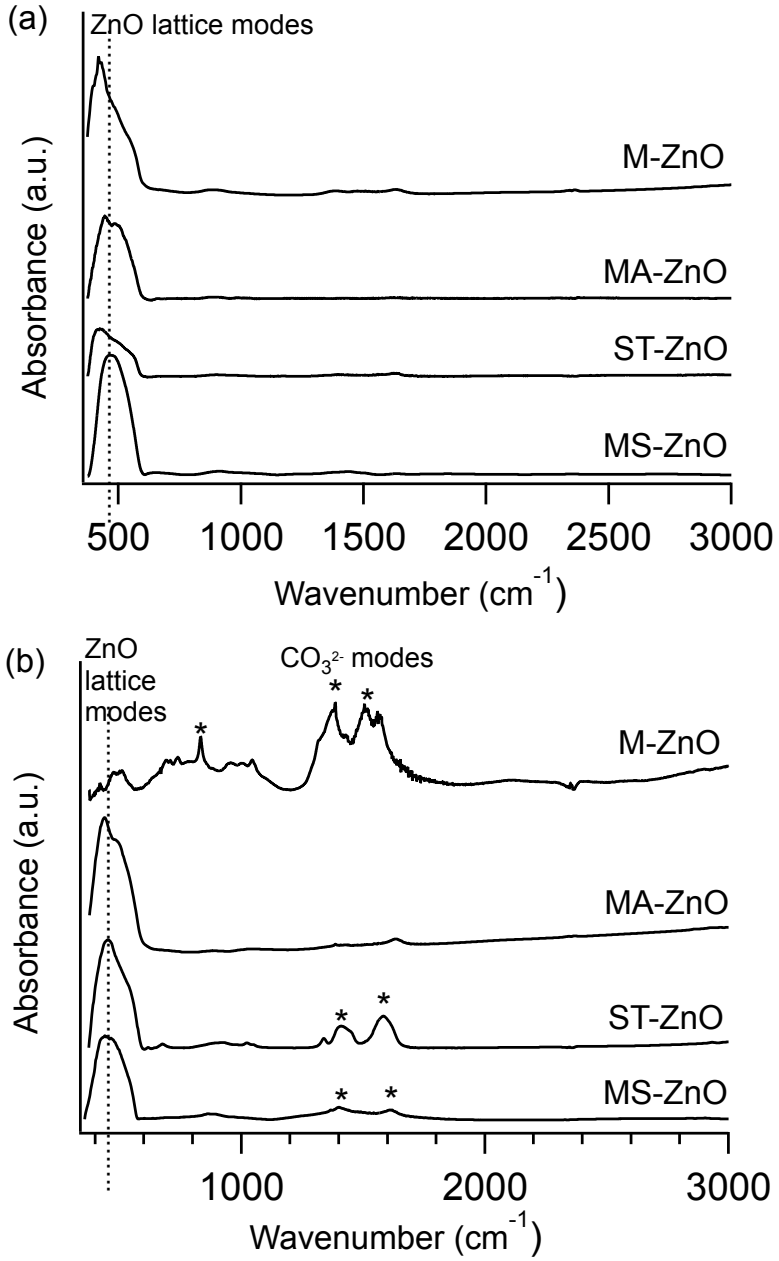

Figure 3.6: Representative FTIR spectra for (a) fresh samples and (b) samples aged for 30 days in a high CO_2 and high humidity environment.

consistent with the XRD data shown in Fig. 3.5. In contrast, after 30 days of exposure to CO_2 and high humidity, there are many new spectral features (Fig. 3.6b). Carbonate vibration modes due to ZHC appear between 1380 and 1510 cm^{-1}, while the peak near 950 cm^{-1} has been attributed to a Zn-OH distortion [29, 30]. ST-ZnO and MA-ZnO show exclusively ZnO, MS-ZnO shows moderate ZHC formation with substantial ZnO remaining, while M-ZnO shows complete conversion to ZHC. We note that the trends for higher amounts of the ZHC decomposition product in the FTIR spectra correlate well with wider Zn $2p_{2/3}$ peaks in the XPS data.

To confirm the transformation from ZnO to ZHC, product from the most degradation prone preparation method (M-ZnO) was confirmed with additional FTIR measurements to monitor relative intensity changes of the Zn-O lattice mode and carbonate modes (Fig. 3.7a), and with TGA weight loss data (Fig. 3.7b). After 30 days of exposure, TGA data on the degradation product compare well with the expected theoretical weight loss of 25.5% for complete ZnO conversion to ZHC [31].

3.5 Discussion: controlling factors for surface reactivity

It is clear that different preparations of ZnO lead not only to distinct particle morphologies, but also to different carbonation tendencies in the ambient and when exposed to wet and CO_2-rich conditions. For reasons explained

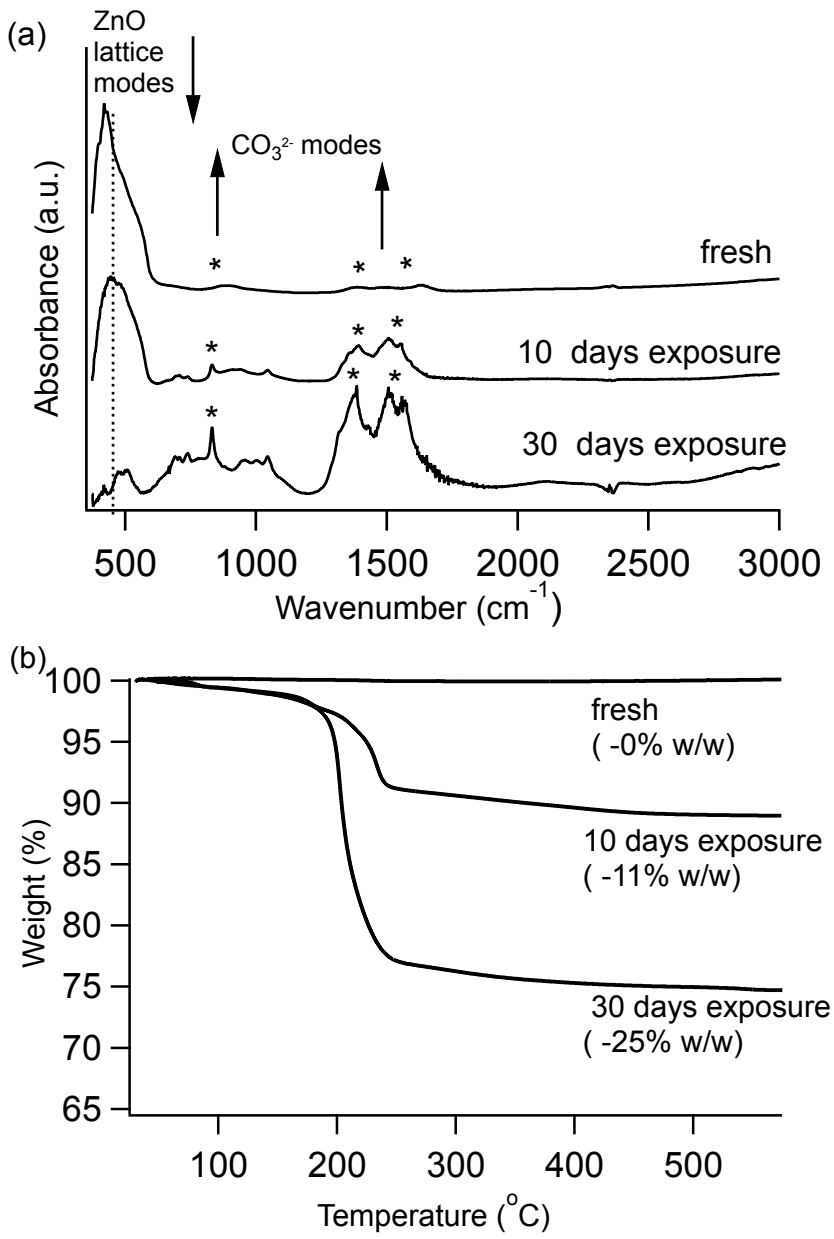

Figure 3.7: (a) Representative FTIR spectra of M-ZnO samples taken after exposure to high CO_2 and humidity for different periods of time and (b) their corresponding TGA data. In (a), the carbonate-related modes are indicated with an asterisk (*).

below, polar surfaces alone cannot be sufficient to explain the differences in the time evolution of the atmospheric degradation. We propose that surface dissolution, influence by surface polarity, is a key factor that affects the extent of carbonation in these materials.

We observe that on only two of the freshly made types (M-ZnO (irregularly shaped) and MS-ZnO (polar faceted)), a thin layer of ZHC forms soon after synthesis. This layer can be detected with XPS (5-10 nm depth probe) but is not present in a large enough quantity for FTIR detection (sensitive to $\leq 1\%$ of bulk). Interestingly, it is the zeta potential measurements that highlight an important difference in the way the carbonate layer behaves on these two different ZnO preparations. On the polar MS-ZnO, the carbonate appears to be preserved under mildly acidic pH conditions, as suggested by the negative zeta potential of MS-ZnO from initially acidic aged suspensions and the small decrease in mean size. On the other hand, M-ZnO has a zeta potential consistent with pure ZnO and shows a very dramatic size decrease.

The differences in the extent of size decrease do not correlate well with original particle size, but they do match the trend in relative tendency to convert to ZHC (Fig. 3.6 and 3.7). For example, our FTIR data indicate that the ZHC layer on the irregularly shaped M-ZnO continues to grow over time at the expense of ZnO (Fig. 3.7a), while the ZHC layer on the polar MS-ZnO does not evolve as rapidly.

Based on these comparison, it seems that the carbonate layer on polar surfaces can act as a protective layer. This idea has been explored by others in

the context of passivating film formation on Zn metal [27]. In general, polar surfaces are expected to have higher surface energies [32], which would be consistent with an increased tendency toward humidity-related degradation. This is in line with our XPS results for surface composition, with the least surface carbonation present on the samples with a higher proportion of non-polar (low-energy) surfaces, namely the rod-like MA-ZnO.

Some have suggested that the hydrophobic nature of ZHC can substantially retard the rate of further ZnO carbonation [33]. However, more recent studies on thermally produced ZnO nanowires concluded that the formation of a ZHC layer inhibits ZnO attack initially, but degradation of the ZnO core is not completely suppressed because the ZHC film is less compact than the underlying ZnO [12, 13]. These observation by others, along with the suppressed degradation we see after annealing our ZnO, suggests that the persistent atmospheric degradation of M-ZnO is likely due to a higher concentration of defects (plausibly due to its fast crystallization process) that make the particle surface more prone to humidity-assisted dissolution [31].

It is worthy of note that the extent of the carbonation differences shown in Figs. 3.6 and 3.7 do not correlate directly with surface area (Table 3.1). For example, the most reactive samples are M-ZnO (BET surface area 3.6 m^2g^{-1}), while the synthesis method that produces the highest surface area product (ST-ZnO, with BET surface area of 9.4 m^2g^{-1}) shows the least evidence of carbonation. Taken together, our analyses show that other factors related to the surface composition have a larger effect on the relative tendency of ZnO

toward atmospheric carbonation.

3.6 Conclusions

Surface polarity impacts the carbonation rates among the differently synthesized ZnO samples, but it is not necessarily the dominant factor. In particular, ZnO produced in rapid reactions can be more susceptible to ambient carbonation; we demonstrate an extreme case wherein exposure to high ambient humidity and CO_2 levels leads to complete conversion of ZnO to $Zn_5(OH)_6(CO_3)_2$ in less than one month. This transformation from a semiconducting metal oxide material to an insulating carbonate phase would have profound impacts on the electrical and optical properties of the product, and could have devastating effects in device applications. While others have have shown that ZnO nanowire degradation can be mitigated by applying a protective coating of compact alumina or titania using atomic layer deposition, [5, 12, 13] our work shows that synthesis and annealing conditions alone can have a dramatic effect on the tendency for ZnO powders to degrade in ambient environments.

Extending beyond the specific case of ZnO, these results are generally important for metathesis reactions and other rapid syntheses for producing nano-crystalline materials [17, 20, 31, 34–38]. Since nanostructured materials made by solid-state metathesis have been utilized for solar cell [36], cathode material [39], UV-detector [37] and gas sensor [35, 40, 41] applications, it is

important to recognize the tradeoffs between rapid production and long-term stability against atmospheric degradation.

3.7 Acknowledgements

Natural Science and Engineering Resource Council (Canada), Petroleum Research Atlantic Canada, and the Canada Foundation for Innovation (New Opportunities) funded this work. K. Kenneally, J. Wells, and H. Hirasawa assisted with sample preparation. W. Aylward (PXRD), J. Collins (TGA), and M. Shaffer (SEM) granted use of the facilities they manage through Memorial University Core Research Equipment and Instrument Training network. V. Booth at Memorial University granted use of DLS and zeta potential instrumentation. J. Wen and A. Chen conducted the BET measurements at Lakehead University, Thunder Bay, Ontario, Canada. Z. Bayindir conducted the XPS measurements at the Dalhousie University Facilities for Materials Characterization managed by the Institute for Research in Materials, which is funded by the Atlantic Innovation Fund and other partners.

3.8 X-ray Photoelectron spectrum: C 1s for ZnO samples

XPS C 1s spectra for freshly made ZnO samples are shown in Fig. 3.8. This figure is not part of the published paper on which this chapter is based [1], but

it was added because the C 1s spectra provide direct evidence for the presence of surface carbonates on some ZnO samples.

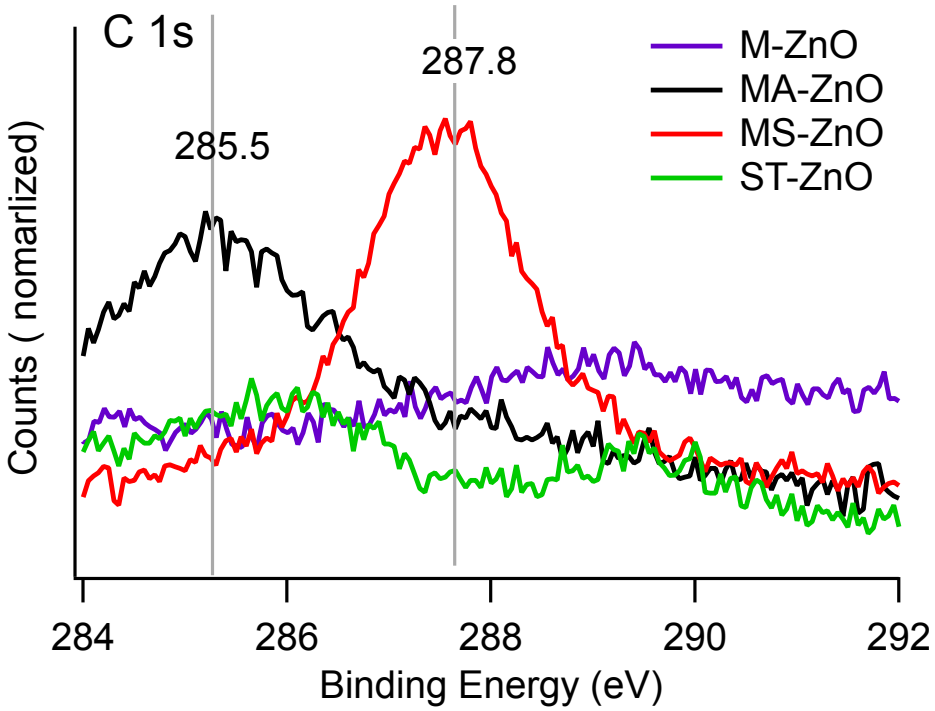

Figure 3.8: Raw XPS data for C 1*s* for fresh ZnO synthesized by different methods. The peak at 287.8 eV corresponds to carbonates. The peak at lower binding energy (285.5 eV) is likely due to the presence of hydrocarbon on the surfaces because the samples were washed with ethanol prior to XPS measurement. (This figure is relevant for Chapter 3, but is not part of the published paper on which that chapter is based [1].)

Bibliography

[1] Jiaqi Cheng and Kristin M. Poduska. Ambient Degradation of ZnO Powders: Does Surface Polarity Matter? *ECS J. Solid State Sci. Technol.*, 3(5):P133–P137, 2014.

[2] C. Soci, A. Zhang, B. Xiang, S. A. Dayeh, D. P. R. Aplin, J. Park, X. Y. Bao, Y. H. Lo, and D. Wang. ZnO Nanowire UV Photodetectors with High Internal Gain. *Nano Lett.*, 7(4):1003–1009, 2007.

[3] Jun Zhang, Shurong Wang, Mijuan Xu, Yan Wang, Baolin Zhu, Shoumin Zhang, Weiping Huang, and Shihua Wu. Hierarchically Porous ZnO Architectures for Gas Sensor Application. *Cryst. Growth Des.*, 9(8):3532–3537, 2009.

[4] Imali A. Mudunkotuwa, John M. Pettibone, and Vicki H. Grassian. Environmental Implications of Nanoparticle Aging in the Processing and Fate of Copper-Based Nanomaterials. *Environ. Sci. Technol.*, 46(13):7001–7010, 2012.

[5] Yang Yang, Dong Sik Kim, Yong Qin, Andreas Berger, Roland Scholz, Hyunbin Kim, Mato Knez, and Ulrich Gösele. Unexpected Long-Term Instability of ZnO Nanowires Protected by a TiO_2 Shell. *J. Am. Chem. Soc.*, 131(39):13920–13921, 2009.

[6] Gregory V. Lowry, Kelvin B. Gregory, Simon C. Apte, and Jamie R. Lead. Transformations of Nanomaterials in the Environment. *Environ. Sci. Technol.*, 46(13):6893–6899, 2012.

[7] Randy A. Reichle, Keith G. McCurdy, and Loren G. Hepler. Zinc Hydroxide: Solubility Product and Hydroxy-complex Stability Constants from 12.575. *Can. J. Chem.*, 53(24):3841–3845, 1975.

[8] Andrej Degen and Marija Kosec. Effect of pH and Impurities on the Surface Charge of Zinc Oxide in Aqueous Solution. *J. Eur. Ceram. Soc.*, 20(6):667–673, 2000.

[9] T. Falk, J.-E. Svensson, and L.-G. Johansson. The Role of Carbon Dioxide in the Atmospheric Corrosion of Zinc: A Laboratory Study. *J. Electrochem. Soc.*, 145(1):39–44, 1998.

[10] Rakel Lindström, Jan-Erik Svensson, and Lars Gunnar Johansson. The Influence of Salt Deposits on the Atmospheric Corrosion of Zinc. The Important Role of the Sodium Ion. *J. Electrochem. Soc.*, 149(2):B57–B64, 2002.

[11] Jonas Hedberg, Steven Baldelli, and Christofer Leygraf. Evidence for the Molecular Basis of Corrosion of Zinc Induced by Formic Acid Using Sum Frequency Generation Spectroscopy. *J. Phys. Chem. Lett.*, 1(10):1679–1682, 2010.

[12] Zhengwei Pan, Jing Tao, Yimei Zhu, Jing-Fang Huang, and M. Parans Paranthaman. Spontaneous Growth of $ZnCO_3$ Nanowires on ZnO Nanostructures in Normal Ambient Environment: Unstable ZnO Nanostructures. *Chem. Mater.*, 22(1):149–154, 2010.

[13] K. A. Cimatu, S. M. Mahurin, K. A. Meyer, and R. W. Shaw. Nanoscale Chemical Imaging of Zinc Oxide Nanowire Corrosion. *J. Phys. Chem. C*, 116(18):10405–10414, 2012.

[14] Bettina Ludi and Markus Niederberger. Zinc Oxide Nanoparticles: Chemical Mechanisms and Classical and Non-classical Crystallization. *Dalton Trans.*, 42:12554–12568, 2013.

[15] Zhi-Yuan Jiang, Tao Xu, Zhao-Xiong Xie, Zhi-Wei Lin, Xi Zhou, Xin Xu, Rong-Bin Huang, and Lan-Sun Zheng. Molten Salt Route Toward the Growth of ZnO Nanowires in Unusual Growth Directions. *J. Phys. Chem. B*, 109(49):23269–23273, 2005.

[16] Tao Xu, Xi Zhou, Zhiyuan Jiang, Qin Kuang, Zhaoxiong Xie, and Lansun Zheng. Syntheses of Nano/Submicrostructured Metal Oxides with All Polar Surfaces Exposed via A Molten Salt Route. *Cryst. Growth Des.*, 9(1):192–196, 2009.

[17] Jiaqi Cheng, Muhammad Asim Rasheed, and Kristin M. Poduska. Exploiting Water-Mediated Ethanol Sensing by Polycrystalline ZnO at

Room Temperature. *ECS J. Solid State Sci. Technol.*, 2(1):Q23–Q26, 2013.

[18] Jagriti Gupta, K.C. Barick, and D. Bahadur. Defect Mediated Photocatalytic Activity in Shape-Controlled ZnO Nanostructures. *J. Alloys Compd.*, 509(23):6725–6730, 2011.

[19] Powder Diffraction File Joint Commission on Powder Diffraction Standards – International Centre for Diffraction Data, 2003.

[20] Xiang R. Ye, Dian Z. Jia, Jian Q. Yu, Xin Q. Xin, and Ziling Xue. One-Step Solid-State Reactions at Ambient Temperatures-A Novel Approach to Nanocrystal Synthesis. *Adv. Mater.*, 11(11):941–942, 1999.

[21] Zeshan Hu, Gerko Oskam, and Peter C. Searson. Influence of Solvent on the Growth of ZnO Nanoparticles. *J. Colloid Interface Sci.*, 263(2):454–460, 2003.

[22] Zeshan Hu, Gerko Oskam, R. Lee Penn, Noshir Pesika, and Peter C. Searson. The Influence of Anion on the Coarsening Kinetics of ZnO Nanoparticles. *J. Phys. Chem. B*, 107(14):3124–3130, 2003.

[23] Zeshan Hu, José F. Herrera Santos, Gerko Oskam, and Peter C. Searson. Influence of the Reactant Concentrations on the Synthesis of ZnO Nanoparticles. *J. Colloid Interface Sci.*, 288(1):313–316, 2005.

[24] A. G. Vega-Poot, G. Rodriguez-Gattorno, O. E. Soberanis-Dominguez, R. T. Patino-Diaz, M. Espinosa-Pesqueira, and G. Oskam. The Nucle-

ation Kinetics of ZnO Nanoparticles from $ZnCl_2$ in Ethanol Solutions. *Nanoscale*, 2:2710–2717, 2010.

[25] R. Al-Gaashani, S. Radiman, A. R. Daud, N. Tabet, and Y. Al-Douri. XPS and Optical Studies of Different Morphologies of ZnO Nanostructures Prepared by Microwave Methods. *Ceram. Inter.*, 39(3):2283–2292, 2013.

[26] J. H. Zheng, Q. Jiang, and J. S. Lian. Synthesis and Optical Properties of Flower-like ZnO Nanorods by Thermal Evaporation Method. *Appl. Sur. Sci.*, 257(11):5083–5087, 2011.

[27] Tim H. Muster and Ivan S. Cole. The Protective Nature of Passivation Films on Zinc: Surface Charge. *Corros. Sci.*, 46(9):2319–2335, 2004.

[28] L. B. Rockland. Saturated Salt Solution for Static Control of Relative Humidity Betwee 5° and 40° C. *Anal. Chem.*, 32:1375–1376, 1960.

[29] Matthew C. Hales and Ray L. Frost. Synthesis and Vibrational Spectroscopic Characterisation of Synthetic Hydrozincite and Smithsonite. *Polyhedron*, 26(17):4955–4962, 2007.

[30] Bin Su, Mei Li, Zhengyu Shi, and Qinghua Lu. From Superhydrophilic to Superhydrophobic: Controlling Wettability of Hydroxide Zinc Carbonate Film on Zinc Plates. *Langmuir*, 25(6):3640–3645, 2009.

[31] Jiaqi Cheng and Kristin M. Poduska. A Strategy for Hydroxide Exclusion in Nanocrystalline Solid-State Metathesis Products. *Nanomater.*, 3(3):317–324, 2013.

[32] Jacek Goniakowski, Fabio Finocchi, and Claudine Noguera. Polarity of Oxide Surfaces and Nanostructures. *Rep. Prog. Phys.*, 71(1):016501, 2008.

[33] Y. Hamlaoui, F. Pedraza, and L. Tifouti. Corrosion Monitoring of Galvanised Coatings Through Electrochemical Impedance Spectroscopy. *Corros. Sci.*, 50(6):1558–1566, 2008.

[34] Limin Ren, Qinming Wu, Chengguang Yang, Longfeng Zhu, Caijin Li, Pengling Zhang, Haiyan Zhang, Xiangju Meng, and Feng-Shou Xiao. Solvent-Free Synthesis of Zeolites from Solid Raw Materials. *J. Am. Chem. Soc.*, 134(37):15173–15176, 2012.

[35] Yali Cao, Dianzeng Jia, Ruiying Wang, and Jianmin Luo. Rapid One-Step Room-Temperature Solid-state Synthesis and Formation Mechanism of ZnO Nanorods as H_2S-Sensing Materials. *Solid-State Electronics*, 82(0):67–71, 2013.

[36] Yantao Shi, Kai Wang, Yi Du, Hong Zhang, Junfu Gu, Chao Zhu, Lin Wang, Wei Guo, Anders Hagfeldt, Ning Wang, and Tingli Ma. Solid-State Synthesis of ZnO Nanostructures for Quasi-Solid Dye-Sensitized

Solar Cells with High Efficiencies up to 6.46%. *Adv. Mater.*, 25:4413–4419, 2013.

[37] Sheo K. Mishra, Rajneesh K. Srivastava, and S. G. Prakash. Photoluminescence and Photoconductivity Studies of ZnO Nanoparticles Prepared by Solid State Reaction Method. *J. Mater. Sci.: Mater Electron.*, 24(1):125–134, 2013.

[38] Ruiying Wang, Dianzeng Jia, and Yali Cao. Facile Synthesis and Enhanced Electrocatalytic Activities of Organic-inorganic Hybrid Ionic Liquid Polyoxometalate Nanomaterials by Solid-state Chemical Reaction. *Electrochimica Acta*, 72(0):101–107, 2012.

[39] Rongrong Jiang, Yudai Huang, Dianzeng Jia, Lishi Wang, and Lei Wang. High-Capacity, High-Cycling Cathode Material Synthesized by Low-Temperature Solid-State Coordination Method for Lithium Rechargeable Batteries. *J. Electrochemical Soc.*, 154(7):A698–A702, 2007.

[40] Yali Cao, Pengfei Hu, Weiyu Pan, Yudai Huang, and Dianzeng Jia. Methanal and Xylene Sensors Based on ZnO Nanoparticles and Nanorods Prepared by Room-Temperature Solid-State Chemical Reaction. *Sens. Actuat. B*, 134:462–466, 2008.

[41] Jin Q. Sun, Ji S. Wang, Xiu C. Wu, Guo S. Zhang, Jun Y. Wei, Shu Q. Zhang, H. Li, and Dai R. Chen. Novel Method for High-Yield Synthesis

of Rutile SnO_2 Nanorods by Oriented Aggregation. *Cryst. Growth Des.*, 6(7):1584–1587, 2006.

Chapter 4

Exploiting Water-Mediated Ethanol Sensing by Polycrystalline ZnO at Room Temperature

Reproduced with permission from The Electrochemical Society [1].

4.1 Abstract

We demonstrate that ambient moisture can dramatically promote the responses of ZnO to ethanol vapor, a hydrophilic gas. By comparing sensor responses in a broad range of humidities, we show that there is a consis-

tent enhancement in ethanol adsorption on ZnO when physisorbed water, detected by capacitance measurements, is present. The time constants related to the capacitive signal recovery during desorption are consistent with the formation of $C_2H_5OH-(H_2O)n$ clusters that have a different desorption rate than water alone. These room temperature results indicate that surface water mediates the dynamic adsorption/re-evaporation equilibrium of solvated ethanol molecules. Thus, attention to interactions between the target gas molecules and their environment is important for understanding the mechanisms behind selective gas sensing.

4.2 Introduction

Moisture is always present in ambient environments, so an understanding of water-solid interactions is important in many applied fields such as corrosion, catalysis, and sensor development [2]. The surface structure and reactivity of semiconducting metal oxides (MOX) such as ZnO, SnO_2 and WO_3 have been studied extensively for electrical gas sensing applications. These materials have highly sensitive electrical conductivity and capacitance responses to many gaseous species including CO, NH_3, and volatile organic compounds (VOCs) while having low production costs and high thermal durability [3]. However, the presence of environmental H_2O can effectively alter the reactivities of MOX surfaces, which leads to difficulties in obtaining reliable and selective sensing signals for different target gases in real-world environ-

ments [4–7].

Most investigations on the gas sensing performance of MOX materials have focused on analyte gas detection at relatively high operating temperatures (500-800 K), where optimal sensing responses are normally reached [8]. This is because the formation of surface hydroxyls from chemisorptive water dissociation tends to dominate at these high temperatures, and the net conductivity changes are determined by surface characteristics such as oxygen species density, surface defects and hydroxyl coverage [2]. At these high temperatures, target gas molecules undergo a combustive type of reaction that yields oxidized or reduced species on the MOX surface [9]. In contrast, at low temperatures ($\leq$ 400 K), physisorbed water in its molecular form can increase the surface conductivity by donating lone pair electrons to the oxide's space charge region. There is surprisingly little work that focuses on water effects on gas-sensing of MOX at room temperature, despite the urgent need for room temperature gas sensors [10]. Polymeric sensors are typically preferred at ambient temperatures, but they can also be adversely affected by the presence of moisture, and they exhibit similar selectivity challenges to those encountered in MOX sensors.

In this study, we show that ambient moisture can dramatically promote the response of ZnO to ethanol (EtOH) vapor, a hydrophilic gas. By comparing sensor recovery times in a broad range of humidities, we show that there is an enhancement of ethanol adsorption on ZnO when it is covered with a physisorbed water layer, whose thickness depends on the relative humidity

(RH) of the atmosphere around it. Capacitance data allow us to infer the formation of ethanol-water critical clusters, and we demonstrate that there is discrimination of sensing events between ethanol vapor and background humidity. Our results show that paying more attention to interactions between the target gas molecules and their environment could offer benefits for developing more selective gas sensing materials.

4.3 Experimental

4.3.1 Synthesis

ZnO particles were synthesized using a room temperature solid-state metathesis reaction [11]. All reagents were analytical grade (99%) and used without further purification. $ZnCl_2$ (Caledon) and NaOH (EM Science) were ground separately to fine powders, then mixed together in a beaker with a molar ratio of 1:2 to react in the following way:

$$2\,NaOH + ZnCl_2 \longrightarrow Zn(OH)_2 + 2\,NaCl \quad (1)$$

$$Zn(OH)_2 \longrightarrow ZnO + H_2O \quad (2)$$

Within 2 min of stirring the solid mixture, there was heat release and generation of water vapor, as well as a color change from white to yellow, and then back to white within tens of seconds after the reaction finished. The product was washed with ultrapure water (Barnstead Nanopure 18.2 Ω·cm) several times to remove the NaCl by-product, and then dried in an oven at

350 K before further characterization.

4.3.2 Material characterization

X-Ray diffraction (XRD) and Fourier transform infrared spectroscopy (FTIR) were used to assess the crystallinity and phase composition of the dried product. XRD data were collected with a Rigaku Ultima IV X-ray diffractometer (Cu Kα, 3°/min, step size 0.02° 2θ), and lattice constant refinements were performed with Jade software (Materials Data Inc.). FTIR data were collected in transmission mode with a Bruker Alpha at 4 cm^{-1} resolution on specimens dispersed in a 7 mm diameter KBr pellet. Representative XRD data, shown in Fig. 4.1a, indicate that the product is highly crystalline with lattice constants of $a = (3.5252 \pm 0.001)$ Å and $c = (5.210 \pm 0.001)$ Å, which are appropriate for wurtzite-type ZnO (JCPDS 36-1451, with $a = 3.250$ Å and $c = 5.207$ Å). No evidence of secondary phases was detected, either in XRD data or in FTIR spectra (Fig. 4.1b). Estimates of particle sizes were obtained by dynamic light scattering methods (Malvern Zetasizer Nano ZS) and confirmed qualitatively from scanning electron microscopy (SEM) images (FEI Quanta 400) of dispersed ZnO particles coated with a conductive carbon layer. Fig. 4.1c shows typical particle aggregates with poorly developed facets and diameters $\sim$ 100 nm. These sizes are consistent with the particle size estimates obtained from light scattering measurements (110 $\pm$ 30 nm). Brunauer-Emment-Teller (BET) analyses yield an average surface area of 3.6 $\pm$ 0.3 m^2g^{-1}. X-ray Photoelectron Spectra (XPS) data collected

with a VG Microtech MultiLab ESCA 2000 indicate O atom binding energies that are consistent with ZnO that has surface hydroxyl groups present [12].

4.3.3 Gas sensing measurement

Thick films (120 ± 30 μm) of ZnO particles served as sensor materials for subsequent study. A slurry of the as-prepared ZnO powder (0.10 g dispersed in 2 mL of acetone and sonicated for 30 s) was slowly poured onto, and spread evenly over, a mechanically polished stainless steel strip. The steel strip served as one electrode for subsequent electrical measurements, and the second electrode was a stainless steel pressure contact on the top of the film. For films with 1 cm × 7 cm area, typical resistance and capacitance values were $\sim$ 20 MΩ and $\sim$ 100 pF, respectively, at 45% ambient RH.

Prior to use, each sensor film was equilibrated in a sealed chamber (25 cm × 25 cm × 25 cm), and Ohmic electrical contacts were made with mechanically polished steel (0.5 cm^2). RH levels inside the test chamber were controlled and modified using different saturated salts solutions. At 295 K, 150 mL of one of the following saturated salt solutions yields a distinct and characteristic relative humidity: CH_3CO_2K (20 ± 2%), K_2CO_3 (45 ± 2%), or KNO_3 (90 ± 2%) [13]. Before initiating gas detection measurements, one of the aforementioned salt solutions was kept in the chamber for two hours to reach the intended equilibrium RH. Our experiments utilized independent control of the RH of the target gas as well. For clarity of presentation in the rest of this manuscript, the humidity levels of the target gases – ethanol-

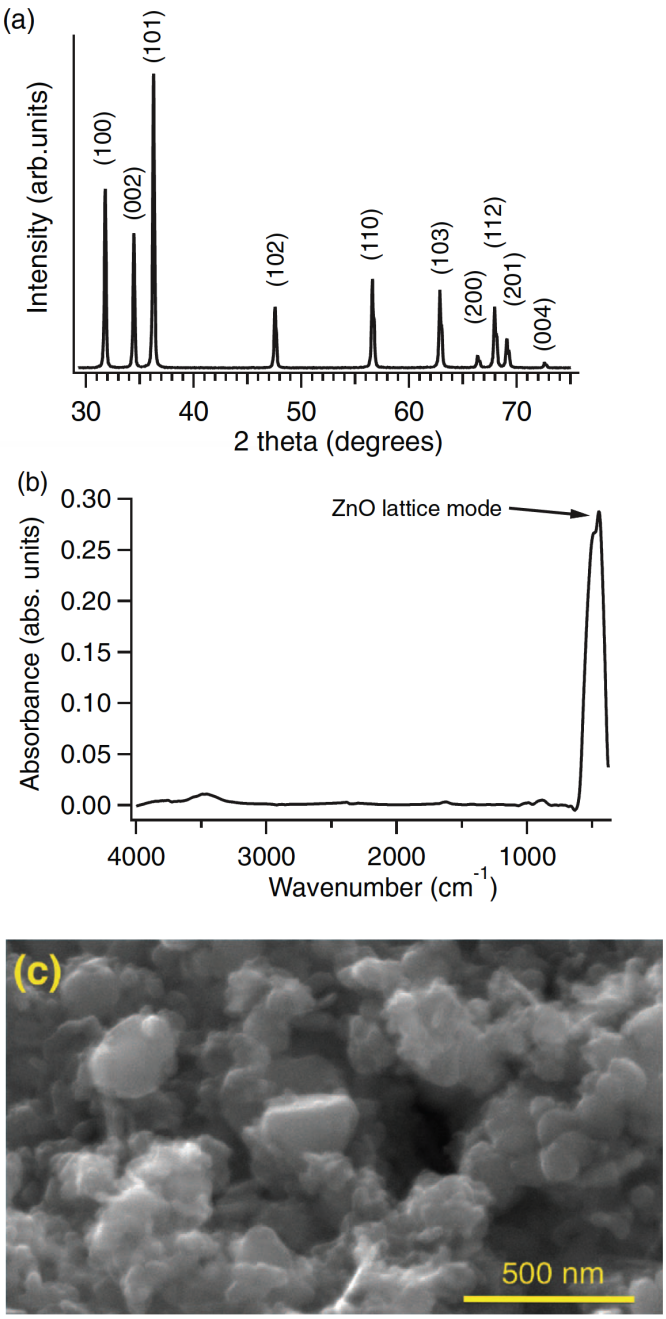

Figure 4.1: (a) Representative XRD data with all peaks indexed to wurtzite-type ZnO. (b) Representative FTIR data show a characteristic ZnO lattice mode peak near 450 cm^{-1}. (c) SEM image of ZnO particles.

water vapor mixtures – are categorized as "dry" (20% RH), "medium" (45% RH), or "wet" (90% RH).

Gas sensing experiments were initiated by injecting 20 mL of the target gas into the chamber in close proximity to the sensing film. Given the large chamber volume relative to that of the injected gas, multiple injections could be executed without interference from one injection to the next. EtOH concentrations were calculated using the standard vapor pressure of anhydrous ethanol (ACS grade) under atmospheric pressure at 294 K. We note that this method of determining gas concentration is more realistic, and more conservative, than some other reports of ethanol sensing by ZnO [14]. All of our experiments used EtOH vapor at 5000 ppm unless otherwise noted.

Sensing responses for the ZnO films were assessed by measuring capacitance changes at 3 kHz with an applied AC RMS voltage of 50 mV (National Instruments LCR meter with PXI-1033 interface). We interpret the response assuming that our films function as parallel plate capacitors such that

$$C = \frac{A\epsilon_0\epsilon}{d} \tag{4.1}$$

where C is the effective capacitance, ϵ_0 is the permittivity of free space, A is the total contact area of the plate, ϵ is the effective dielectric constant of the thin film [15]. Since ϵ changes with humidity, and with exposure to target gases such as ethanol, the resulting change in capacitance yields a measurable

response. We report the response

$$S = \frac{C_g - C_a}{C_a} \tag{4.2}$$

where C_g is the maximum capacitance response after exposure to the target gas, and C_a is the baseline capacitance value. The recovery time τ is extracted from an exponential fit of the sensor's return to baseline (after exposure to the target gas) and corresponds to the time required to return within 95% of the original (baseline) capacitance. All sensing studies were conducted at room temperature (295 $\pm$ 2 K).

4.4 Results and Discussion

4.4.1 Response enhancement with humidity

Increasing ambient humidity causes a significant increase in the ZnO response to ethanol vapor. A representative example of this effect is shown Fig. 4.2a, which compares sensor capacitance responses triggered by a series of four identical ethanol vapor injections (5000 ppm in a 45% RH target gas) at ambient (test chamber) RH values of 20%, 45% and 90%. The dotted lines indicate the time at which the target gas was introduced to the sensor. Both the baseline (resting) capacitance values and the magnitudes of the sensing responses increase with increasing ambient humidity. The arrows indicate the below-baseline recovery that occurs when the target gas has a RH that

is much lower than the ambient RH. Fig. 4.2b shows that ZnO response to EtOH increases with both increasing ambient RH and increasing target gas RH over the full range of ambient and target gas RH combinations. We note that the poor response of ZnO to ethanol vapor in a dry environment is consistent with previous investigations [7, 14, 16–18].

It is well known that at room temperature, a hydrophilic solid surface in air will adsorb many layers of water, leading to formation of a thin condensed water layer on the surface whose thickness equilibrates with ambient RH [19]. Since water has dielectric constant of 80, while that for ZnO is 10, an absorbed water layer will increase the effective film capacitance.

Our experiments show evidence of this changing water layer thickness in the capacitance baseline of the sensor, since at resting value (with no target gas present), the capacitance increases with increasing ambient RH. For example, Fig. 4.2a shows that an ambient RH value of 20% registers a baseline capacitance near 70 pF, while an ambient RH of 90% increases the baseline above 300 pF.

4.4.2 Desorption of water and ethanol hydrates

Despite the synergistic effect of water and EtOH in the ZnO response, it is also possible to discriminate between EtOH and H_2O sensing events by analyzing the time required for the measured capacitance to return to its baseline value after exposure to a pulse of the target gas. We compared representative sensing signals of four target gases (dry ethanol (20% RH),

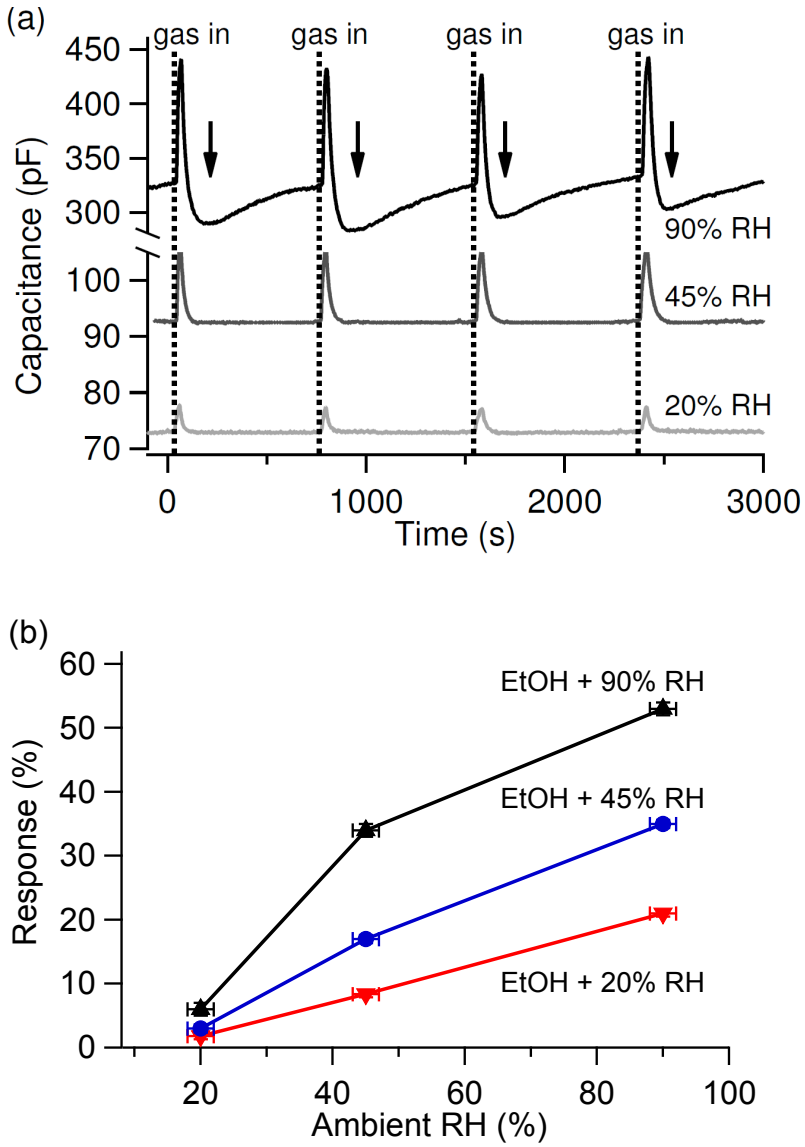

Figure 4.2: (a) A representative comparison of sensor capacitance responses triggered by ethanol vapor injections (5000 ppm in a 45% RH target gas) at ambient (test chamber) RH values of 20%, 45% and 90%. (b) ZnO response to EtOH increases with both increasing ambient RH and increasing target gas RH. The lines connecting the data points serve as guides to the eye, and uncertainty estimates are displayed for each data point.

wet ethanol (90% RH), dry air (20% RH) and water vapor (100% RH)) in humid (90% RH) ambient conditions where there will be a high level of surface water on ZnO. Fig. 4.3a shows that, under these conditions, ethanol vapor and water vapor target gases behave in qualitatively different ways. EtOH (whether dry or wet) always gives a capacitance increase. On the other hand, the response in the absence of ethanol (RH-controlled air only) appears to depend on the fugitive build-up (or removal) of the condensed thin water layer on the ZnO surface. Thus, an increase in capacitance occurs when the RH of the target gas is higher than ambient, while a decrease occurs when the target gas that is drier than ambient. An extreme example of this effect is the "over-recovery" that occurs when a relatively dry target gas is directed on the ZnO film, as indicated with arrows in Fig. 4.2a. We infer from this behavior that the dry EtOH removes water molecules from the ZnO surface in order to form EtOH-H_2O clusters, and then atmospheric water vapor must be reabsorbed to equilibrate the ZnO surface water.

Solvation of EtOH has been heavily investigated for its fundamental non-ideal behavior of mixing that is caused by a hydrogen-bonded H_2O-EtOH network. Many studies have shown that when ethanol vapor interacts with surface water, a cluster of $C_2H_5OH-(H_2O)n$ with a critical size ($1 \leq n \leq 3$) will form at the gas-liquid interfaces [20]. For example, Katrib *et al.* investigated the composition and geometry of ethanol-water clusters during the ethanol vapor uptake process by water, and their experimental and theoretical results show that the interaction of one water molecule with ethanol (n=1) is favored

[21].

At this stage, we are not able to confirm the exact structure of the ethanol hydrate that desorbs from our ZnO surfaces. However, evidence for the existence of ethanol hydrates was derived from the signal recovery time constant. Assuming first-order desorption kinetics [22], we fitted the signal recovery curves of all sensing data with a single exponential function to extract the recovery constant. What is surprising in the data trend shown in Fig. 4.3b is that the recovery constant for EtOH — for any combination of target gas and ambient RH value — is identical, despite the fact that the sensor response is strongly affected by ambient RH (as shown in Fig. 4.3b). This again suggests that ethanol-water association on the ZnO surface leads to the formation of a cluster whose desorption rate is independent of the ambient water pressure.

In contrast, for water vapor alone, the recovery time constant increases with an increasing ambient RH (Fig. 4.3b). We believe this is due to slower desorption of water from ZnO surface with higher water vapor pressure in the surrounding environment [23].

A schematic overview of the ethanol-hydrate-based sensing mechanism for ZnO at room temperature is depicted schematically in Fig. 4.4. Limited response to ethanol at low RH is due to the low adsorption affinity between ethanol and a dry ZnO surface (Fig. 4.4a). For high ambient RH, however, the adsorption efficiency of ethanol onto ZnO surface can be enhanced by solvation by a surface water layer to form ethanol-water clusters (Fig. 4.4b). When desorption occurs, surface water molecules that have become part

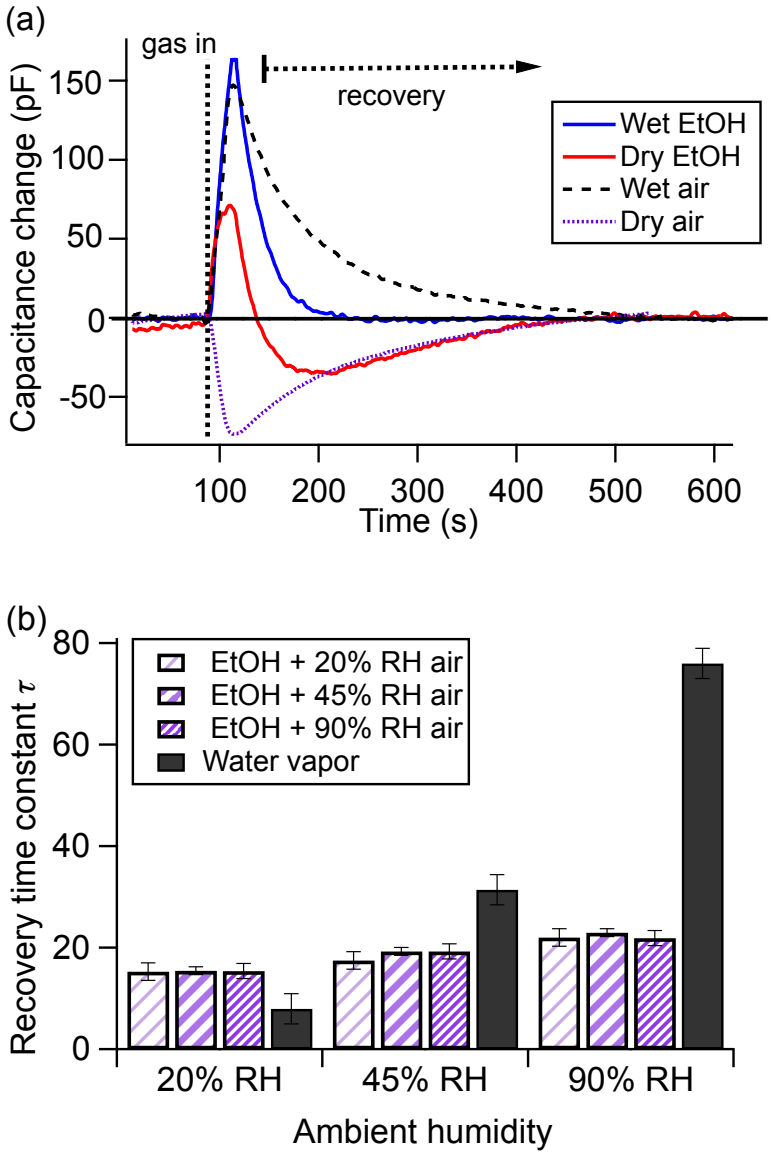

Figure 4.3: (a) Comparison of representative capacitive signals of ZnO when sensing dry air (20% RH), wet air (100% RH), dry ethanol vapor (5000 ppm at 20%), or wet ethanol vapor (5000 ppm at 90% RH) in a test chamber held at 90% ambient RH. (b) Comparison of sensor recovery times after exposure to target gases with different humidities in test chamber environments with a range of different ambient humidities.

of the EtOH-water clusters are removed, thereby thinning the water layer which results in a drop of sensor capacitance below the original starting (baseline) value (Fig. 4.4c). (The experimental observation of this water removal appears as a capacitance decrease below the original baseline level, as indicated by the arrows in Fig. 4.2a). We note that this below-baseline recovery effect is less predominant when the humidity level of the incident ethanol vapor is comparable to that of the surrounding environment.

To confirm the validity of this water-mediated room temperature sensing mechanism, we executed control experiments by testing different hydrophobic vapors, including hexane, and benzene. Each of these gases has been reported as detectable by ZnO-based gas sensors at higher temperatures (500-800 K) [24–26], but no sensing data are reported at room temperature. In our room temperature experiments, none of these vapors show a discernible capacitance response for any level of ambient or target gas humidity. This suggests that room temperature response depends critically on the solubility of the target gas in water. We also executed other control experiments wherein, using other synthetic methods [27, 28], we made several types of ZnO particles with different size distributions ranging from ~ 5 nm to ~ 2 μm. Regardless of the ZnO synthesis method, we observed similar trends in RH effects at room temperature, including increased response to EtOH for higher ambient RH as well as RH-independent recovery time constants for EtOH sensing.

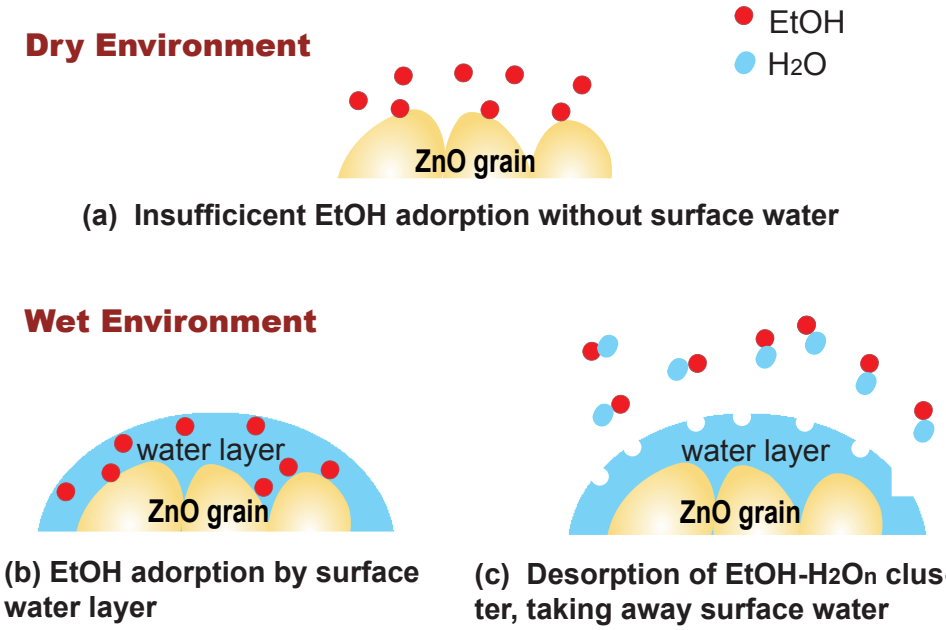

Figure 4.4: Schematic diagram depicting the ethanol sensing processes by ZnO grains under (a) dry and (b) wet ambient RH conditions. (c) When the ambient RH is high, EtOH desorbs as a complex with water, thereby temporarily depleting some of the surface water.

4.5 Conclusions

Lack of selectivity is a common drawback of metal oxide gas sensors, but our data show that the response of dry air is qualitative different, and there are quantitative differences in the recovery times between wet air and the ethanol-containing test gases. The recovery time for EtOH sensing is similar for all target gas and ambient humidities. However, more humid environments show a slower sensor recovery after exposure to either 20% or 100% RH air alone, due to drying and subsequent rehydration of the ZnO surface. Thus, tailoring the interaction between the target gas and ambient water vapor can simultaneously help improve sensor response and promote selectivity to hydrophilic ethanol gas at room temperature.

4.6 Acknowledgments

Natural Science and Engineering Resource Council (Canada), Petroleum Research Atlantic Canada, and the Canada Foundation for Innovation (New Opportunities) funded this work. We also acknowledge Dr. W. Aylward (XRD, grain size analyzer) and Dr. M. Shaffer (SEM) for use of their facilities through Memorial University's Core Research Equipment and Instrument Training network, Ms. J. Wen and Prof. A. Chen for BET measurements at Lakehead University (Thunder Bay, Ontario, Canada) and Dr. Z. Bayindir at the Dalhousie University Facilities for Materials Characterization managed by the Institute for Research in Materials (funded by the Atlantic

Innovation Fund and other partners).

4.7 Discussion of the ethanol sensing mechanism

*This section is not part of the original published paper on which this chapter is based (J. Cheng, M. A. Rasheed, K. M. Poduska, ECS J. Solid State Sci. Technol., **2**, Q23, 2013 [1]).*

Our results clearly show enhanced EtOH sensing responses at RT when more water is present in the environment. Also, the recovery behavior of EtOH sensing responses under various humidity conditions reveals a synergistic EtOH-water interaction at the sensor surface, which shows a clear distinction from water response alone. In regard to the recovery time analysis, an additional point—which was not addressed in the publication—is that the "over-recovery" feature in dry EtOH sensing curve also shows the distinction between water and EtOH adsorption/desorption kinetics. We demonstrate this by fitting the "re-hydration" portion of the curve, *i.e.* the portion between the minimum of the curve below the baseline after "over-recovery" and the baseline at which the equilibrium fully restores to the state prior to gas exposure, with a single exponential function (see Fig. 4.5), and the time constant extracted from this portion is consistent with that from a water response under the same ambient humidity level.

In this section, we also provide further discussion and analysis on the data

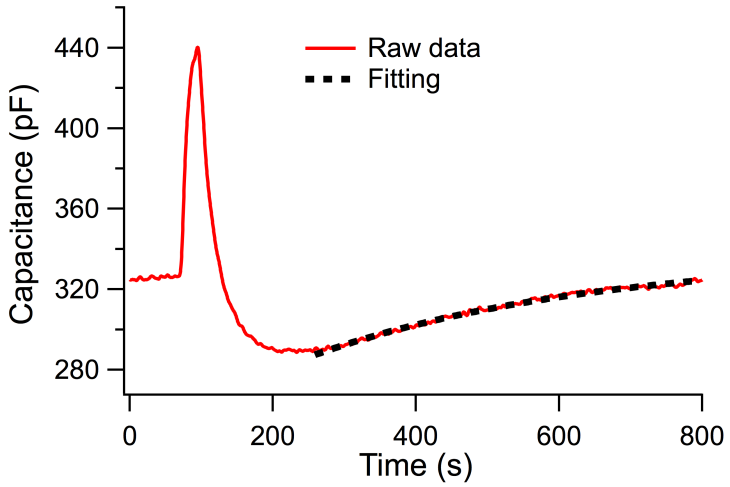

Figure 4.5: A representative sensing response of "dry EtOH". The "re-hydration" portion of the curve is fitted with a single exponential function (the dash curve).

in order to support our assumption that the capacitive response of our ZnO film during the RT sensing event is solely a consequence of physisorption of gas molecules with larger dielectric constant than ZnO.

As described above, the capacitance of our sensor with the sandwich geometry can be approximated by a parallel plate capacitor, as shown in Fig. 4.6.

$$C = \frac{\epsilon_{\text{effective}}\epsilon_0}{d} \tag{4.3}$$

where C is the effective measured capacitance, ϵ_0 is the permittivity of free space, A is the total contact area of the plate, d is the distance between the plates and $\epsilon_{\text{effective}}$ is the effective dielectric constant of the polycrystalline film and the environment around it.

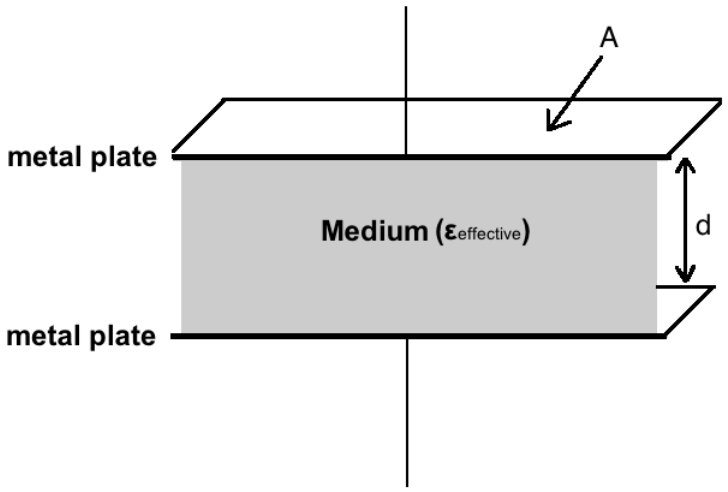

Figure 4.6: Scheme of our model capacitor illustrating $\epsilon_{\text{effective}}$ by viewing the substances between the metal plates as a homogenous medium.

Although it is difficult to calculate the true dielectric constant of the polycrystalline ZnO film directly from the corresponding capacitance values, we can, however, evaluate the change of $\epsilon_{\text{effective}}$ after gas exposure using the changes in the film's capacitance (We made an assumption that A and d do not change with humidity or gas exposure). In Fig. 4.2a, the measured (baseline) capacitance has increased from 75 pF to 345 pF with increasing ambient humidity level from 20% to 90%. The ratio of capacitance between the two baseline can be calculated by:

$$\frac{C(90\%RH)}{C(20\%RH)} = \frac{\epsilon(90\%RH)}{\epsilon(20\%RH)} = \frac{345pF}{75pF} = 4.5 \tag{4.4}$$

This implies that the $\epsilon_{\text{effective}}$ has increased by a factor of 4.5 from a "dry"

to a "wet" environment. Since the dielectric constant of water (~ 80) is 10 times larger than that of ZnO (~ 8), a complete wetting of the medium could lead to a ratio as high as 10. Viewing from this perspective, we believe that a factor of 4.5 in $\epsilon_{\text{effective}}$ enhancement observed by us is consistent with a partial wetting of the ZnO film *via* water adsorption/condensation.

Effects of EtOH exposure on $\epsilon_{\text{effective}}$ can also be estimated by dividing the peak capacitance of the EtOH sensing responses by the baseline. In Fig. 4.2a, the corresponding ratios at various RHs are ~ 1.05 (20% RH), ~ 1.2 (45% RH) and ~ 1.4 (90% RH), respectively. Given the dielectric constant of EtOH (~ 24), these ratios obtained for responses to 5000 ppm EtOH are well below the upper limit we might expect that is $\epsilon(\text{EtOH})/\epsilon(\text{ZnO}) \sim 3$.

Some recent studies have paid attention to molecular level details of water/EtOH adsorption on ZnO surfaces at room temperature. Xie *et al.* [29] investigated the adsorption/desorption mechanism for different alcohols at ZnO surfaces in a dry environment in developing quartz crystal microbalance gas sensor. They concluded that EtOH molecules would first chemisorb onto a ZnO surface *via* the hydroxyl group in the molecule, followed by further physisorption/condensation. They showed that the chemisorption process, which is associated with a larger desorption time constant, dominates at low analyte concentrations. At high analyte concentrations, however, the adsorption-desorption equilibrium is controlled by physisorption that is often characterized by a smaller desorption time constant. Our data is consistent with the physisorption model because a single time constant was observed in

the recovery/desorption curve in the responses to EtOH.

Finally, we discuss the effects of EtOH adsorption on the electronic property of ZnO. This is a kind reminder from Dr. Simon Garcia at Kenyon College who suspects that the EtOH adsorption could also alter the electronic characteristics of ZnO surface because EtOH is a good Lewis base with strong tendency to donate electrons, and such electron transfer between EtOH and ZnO—if indeed occurs —could also be a source of sensor's capacitance responses. Nevertheless, we exclude this possibility based on a recent computational study published by Korir *et al.*, in which the authors have shown that the adsorption of EtOH molecules onto ZnO surface would induce no change in the destiny of states plot of ZnO surface [30].

Bibliography

[1] Jiaqi Cheng, Muhammad Asim Rasheed, and Kristin M. Poduska. Exploiting Water-Mediated Ethanol Sensing by Polycrystalline ZnO at Room Temperature. *ECS J. Solid State Sci. Technol.*, 2(1):Q23–Q26, 2013.

[2] Michael A. Henderson. The Interaction of Water with Solid Surface: Fundemental Aspects Revisited. *Surf. Sci. Rep.*, 46:1–308, 2002.

[3] Alexandru Oprea, Nicolae Barsan, and U. Weimar. Work Function Changes in Gas Sensitive Materials: Fundamentals and Applications. *Sens. Actuat. B*, 142:470–493, 2009.

[4] R. Binions, H. Davies, A. Afonja, S. Dungey, D. Lewis, D. E. Williams, and I. P. Parkin. Zeolite-Modified Discriminating Gas Sensors. *J. Electrochem. Soc.*, 156:J456–J51, 2009.

[5] J. D. Prades, F. Hernández-Ramírez, T. Fischer, M. Hoffmann, R. Müller, N. López, S. Mathur, and J. R. Morante. Quantitative Analysis of CO-Humidity Gas Mixtures with Self-Heated Nanowires Operated in Pulsed Mode. *Appl. Phys. Lett.*, 97:243105, 2010.

[6] Qi Qi, Tong Zhang, Xuejun Zheng, Huitao Fan, Li Liu, Rui Wang, and Yi Zeng. Electrical Response of Sm_2O_3-doped SnO_2 to C_2H_2 and Effect of Humidity Interference. *Sens. Actuat. B*, 134:36, 2008.

[7] Zikui Bai, Changsheng Xie, Mulin Hu, Shunping Zhang, and Dawen Zheng. Effect of Humidity on the Gas Sensing Property of the Tetrapod-Shaped ZnO Nanopowder Sensor. *Sens. Actuat. B*, 149:12–17, 2008.

[8] N. Barsan, D. Koziej, and U. Weimar. Metal Oxide-Based Gas Sensor Research: How to? *Sens. Actuat. B*, 121:18–35, 2007.

[9] G. H. Jain. MOS Gas Sensors: What Determines Our Choice? *Proceedings of the Fifth International Conference on Sensing Technology 2011*, N/A:71–77, 2011.

[10] Noboru Yamazoe. Toward Innovations of Gas Sensor Technology. *Sens. Actuat. B*, 108:2–14, 2005.

[11] Yali Cao, Pengfei Hu, Weiyu Pan, Yudai Huang, and Dianzeng Jia. Methanal and Xylene Sensors Based on ZnO Nanoparticles and Nanorods Prepared by Room-Temperature Solid-State Chemical Reaction. *Sens. Actuat. B*, 134:462–466, 2008.

[12] Jun Lu, Ka M. Ng, and Shihe Yang. Efficient, One-Step Mechanochemical Process for the Synthesis of ZnO Nanoparticles. *Ind. Eng. Chem. Res.*, 47(4):1095–1101, 2008.

[13] L. B. Rockland. Saturated Salt Solution for Static Control of Relative Humidity Between 5°C and 40 °C. *Anal. Chem.*, 32:1375–1376, 1960.

[14] Xiaoyan Zhou, Jianpeng Li, Ming Ma, and Qingzhong Xue. Effect of Ethanol Gas on the Electrical Properties of ZnO Nanorods. *Physica E*, 32:1056–1060, 2011.

[15] T. T. Grove, M. F. Masters, and R. E. Miers. Determining Dielectric Constants Using A Parallel Plate Capacitor. *Am. J. Phys.*, 73:52–56, 2005.

[16] Yu Jin. Chen, Chun. Ling. Zhu, and Gang. Xiao. Ethanol Sensing Characteristics of Ambient Temperature Sonochemically Synthesized ZnO Nanotubes. *Sens. Actuat. B*, 129:639, 2008.

[17] Yujin. Chen, C. L. Zhu, and G. Xiao. Reduced-temperature Ethanol Sensing Characteristics of Flower-Like ZnO Nanorods Synthesized by A Sonochemical Method. *Nanotechnology*, 17:4537–4541, 2006.

[18] Q. Wan, Q. H. Li, Y. J. Chen, T. H. Wang, X. L. He, J. P. Li, and C. L. Lin. Fabrication and Ethanol Sensing Characteristics of ZnO Nanowire Gas Sensors. *Appl. Phys. Lett.*, 84(18):3654–3656, 2004.

[19] C. Leygraf. *Atmospheric Corrosion*. John Wiley: New York, US, 2000.

[20] Paul Davidovits, Charles E. Kolb, Leah R. Williams, John T. Jayne, and Douglas R. Worsnop. Update 1 of Mass Accommodation and Chemical Reactions at Gas-Liquid Interfaces. *Chem. Rev.*, 111:1323–1354, 2011.

[21] Y. Katrib, Ph. Mirabel, S. Le Calvé, G. Weck, and E. Kochanski. Experimental Uptake Study of Ethanol by Water Droplets and Its Theo-

retical Modeling of Cluster Formation at the Interface. *J. Phys. Chem. B*, 106:7237–7245, 2002.

[22] A. Fort, M. Mugnaini, I. Pasquini, S. Rocchi, and V. Vignoli. Modeling of the Influence of H_2O on Metal Oxide Sensor Responses to CO. *Sens. Actuat. B*, 159:82–91, 2011.

[23] Zhi Chen and Chi Lu. Humidity Sensors: A Review of Materials and Mechanisms. *Sens. Lett.*, 3(4):274–295, 2005.

[24] B. L. Zhu, C. S. Xie, A. H. Wang, D. W. Zeng, W. L. Song, and X. Z. Zhao. The Gas-sensing Properties of Thick Film Based on Tetrapod-Shaped ZnO Nanopowders. *Mater. Lett.*, 59:1004–1007, 2005.

[25] Tian Shouqin, Fan Yang, Dawen Zeng, and Changsheng Xie. Solution-Processed Gas Sensors Based on ZnO Nanorods Array with An Exposed (0001) Facet for Enhanced Gas-Sensing Properties. *J. Phys. Chem. C*, 116:10586–10591, 2012.

[26] P. K. Basu, P. Bhattacharyya, N. Saha, H. Saha, and S. Basu. The Superior Performance of the Electrochemically Grown ZnO Thin Films as Methane Sensor. *Sens. Actuat. B*, 133:357–363, 2008.

[27] Tao Xu, Xi Zhou, Zhiyuan Jiang, Qin Kuang, Zhaoxiong Xie, and Lansun Zheng. Syntheses of Nano/Submicrostructured Metal Oxides with All Polar Surfaces Exposed via A Molten Salt Route. *Cryst. Growth Des.*, 9(1):192–196, 2009.

[28] Jagriti Gupta, K.C. Barick, and D. Bahadur. Defect Mediated Photocatalytic Activity in Shape-Controlled ZnO Nanostructures. *J. Alloys Compd.*, 509(23):6725–6730, 2011.

[29] Juan Xie, Hu Wang, and Ming Duan. QCM Chemical Sensor Based on ZnO Colloid Spheres for the Alcohols. *Sens. Actuat. B*, 203(0):239–244, 2014.

[30] K. K. Korir, A. Catellani, and G. Cicero. Ethanol Gas Sensing Mechanism in ZnO Nanowires: An ab Initio Study. *J. Phys. Chem. C*, 118(42):24533–24537, 2014.

Chapter 5

Capacitive Gas Sensing by ZnO at High Temperature

5.1 Abstract

This chapter presents results of capacitive gas sensing experiments conducted at high temperatures. Various types of ZnO samples synthesized differently were tested for their capacitance responses to organic vapors. Our results indicate that, depending on the operating temperatures, the ZnO sensors exhibit very different sensitivities and selectivity. On one hand, the overall sensing responses were enhanced drastically at high T; on the other hand, the gas selectivity, which at room temperature was based on hydrophilicity of target gas, is no longer present at high T. The trends observed at these high temperatures do not correlate with the sensor's responses at RT to

same target gas molecules, which suggests that the nature of gas-surface interactions for these molecules tested could be altered drastically by the temperature rise. Moreover, since differently synthesized ZnO samples show apparently different sensing behaviors, we examined factors such as particle sizes, shapes (surface reactivities) to assess their sensing performances.

5.2 Introduction

The surface conductivity of semiconducting MOX (ZnO, SnO_2) can be modulated by gas exposure. This leads to many possibilities for utilizing ultra-fine MOX structures as gas sensing materials for detecting CO, H_2 and organic vapors. However, the capacitance responses of the MOX to these gases have long been overlooked, since there remains a lack of clear evidence showing that capacitance, which is based on changes of effective dielectric constant, could be a better signal transduction principle than resistance for MOX-based gas sensors in terms of sensitivity and cost.

Nevertheless, one exception is humidity sensing, for which a capacitive sensor has received considerable popularity. Compared to its resistive counterpart, it has advantages such as high sensitivity, long term stability and structural simplicity [1]. One of the most widely used materials for capacitive humidity sensing is porous Al_2O_3 [1, 2]. The success of capacitive gas sensors in humidity sensing is largely due to an abnormally high ϵ of water (~ 80) compared to Al_2O_3 and other MOX (~ 10). However, when detecting VOCs

with smaller ϵ, its applicability is substantially reduced. As a consequence, only a handful of recent studies have focused on capacitive VOC sensing using various MOX nano-materials at room temperature [3–5].

In this chapter, I extend my investigations of ZnO capacitive gas sensors by testing their sensing behaviors at high operating temperatures. What motivated this study is that most MOX-based resistive sensors exhibit optimal sensitivities at high temperatures (≥ 250 °C) [6], and we wanted to examine the capacitance responses of our ZnO samples to various VOCs (ethanol, hexane, and toluene) at these elevated temperatures. In companion with the RT sensing responses, our testing results at high T show drastically enhanced capacitive responses of ZnO nanoparticles to both hydrophilic EtOH and hydrophobic hexane vapor. The difference in sensing behaviors among ZnO samples prepared by different methods has been discussed based on the impacts of particle size/shape and surface reactivities.

5.3 Experimental

5.3.1 Synthesis and characterization

Three types of ZnO with distinct size and shape, namely MA-ZnO, ST-ZnO and MS-ZnO, were synthesized by different methods. The details of synthesis and characterization were included in Chapter 3. The XPS data presented in this chapter is different from Chapter 3 as new data fitting was performed.

5.3.2 Gas sensing measurements

At room temperature, the gas sensing measurement setup was the same as reported in a previous study [4] (described in Chapter 4).

Several modifications to the room temperature gas sensing setup were made to construct a high T gas sensor testing system. Aluminum plates were used to make electrical contacts with the ZnO sensing layer. The sensor was then placed in a tube furnace (Lindberg/Blue 1500 °C, Thermo Scientific). During a typical measurement, 100 mL of target gas was injected into the tube, and then released by opening the ends of the tube. At elevated temperatures, the humidity level in the environment was not deliberately controlled (the sensing environment was assumed to be dry). The water content in the target gases was not calibrated, but it was $\sim$ 20% RH.

Selection of target gases was based on our previous ambient sensing experiments, in which ZnO capacitive sensor selectively detected hydrophilic EtOH [4]. Herein, we tested hydrophilic EtOH as well as hydrophobic hexane and toluene vapors. In resistive sensing mode, both EtOH and hexane reportedly can be sensed by pure ZnO at high temperature [7, 8]. However, no sensing response was reported for the toluene vapor by ZnO, unless the ZnO is functionalized with Au nanoparticles [9]. In our experiments, the typical gas concentration was 1000 ppm for VOCs unless otherwise noted. Additionally, to assess the possible humidity impact at high T, water vapor (90% RH) was also tested.

5.4 Results

5.4.1 Surface analysis

Gas sensing is triggered by gas-surface interactions [6]. Therefore, we analyzed the surface compositions of ZnO using XPS—measured in ultra high vacuum at room temperature—on recently made samples.

O 1s raw spectra for the three ZnO samples are shown in Fig. 5.1. Previously, we reported that ZnO polar surfaces would undergo rapid ambient carbonation, forming a new crystal phase $Zn_5(CO_3)_2(OH)_6$, denoted as ZHC [10]. The binding energy of O 1s in the ZHC phase was confirmed from synthesized ZHC, which yields a single peak at 534 eV (Fig. 5.1d).

Apart from ZHC peak, peaks between 530.0 eV and 533.5 eV are likely due to surface oxygen of ZnO with different origins. The location and intensity of the O 1s peaks on each ZnO surface is summarized in Table 5.2. A literature search was conducted for peak assignments; and the results are summarized in Table 5.1. O 1s peaks on ZnO surfaces have been attributed to three types of surface oxygens. The first peak at 530.7 $\pm$ 0.2 eV, denoted as O_b, corresponds to bulk lattice O that is stoichiometrically bonded with neighboring lattice Zn in the wurtzite crystal structure. The second peak at 531.5 $\pm$ 0.2 eV was attributed to two possible sources, depending on the experimental setup: (1) the O^{2-} in oxygen-deficient regions within the matrix of ZnO (O_v), or (2) the surface hydroxyl (Zn-OH). The third peak at higher binding energy 533.0 $\pm$ 0.5 eV was assigned to the chemisorbed O (O_{ad})

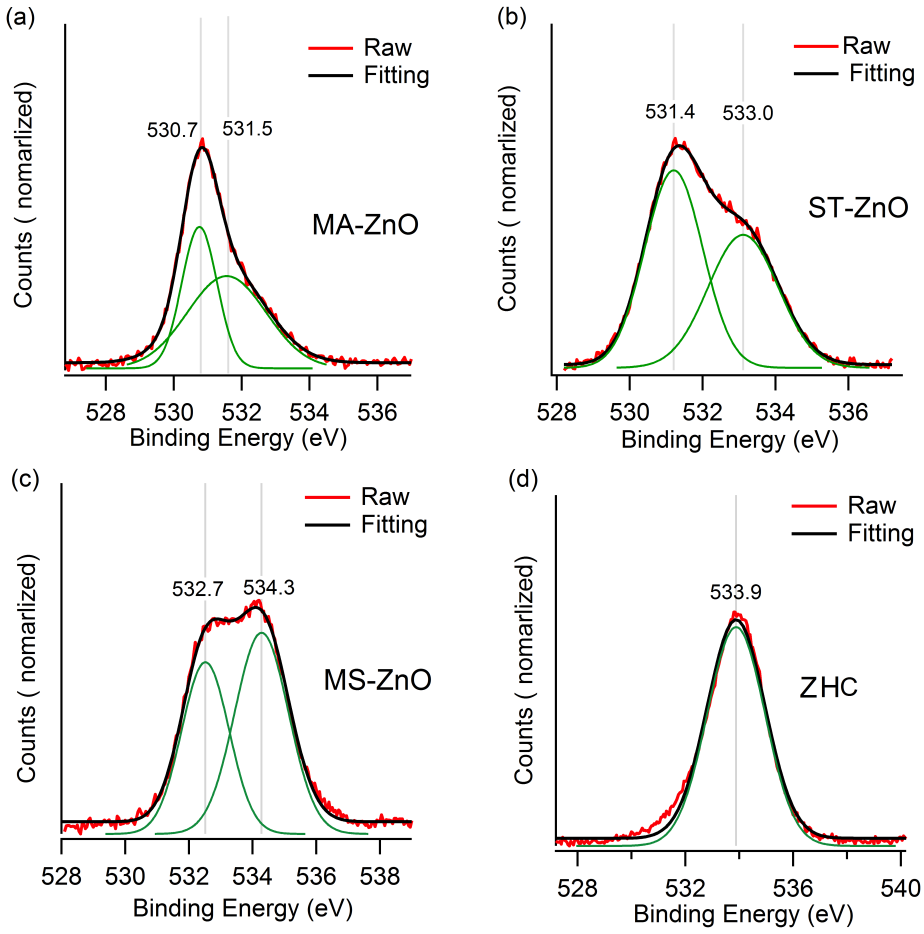

Figure 5.1: XPS results for O 1s electrons on the surfaces of (a) MA-ZnO, (b) ST-ZnO, (c) MS-ZnO, and the (d) $Zn_5(CO_3)_2(OH)_6$ sample. The raw data were fitted with Gaussian functions.

Table 5.1: Some reported assignments of O 1s peak positions (unit: eV) of ZnO surfaces in the literature.

ZnO types	Lattice O_b	Lattice O_v or -OH	Chemisorbed O_{ad}
Nanoparticle [13]	529.5	N/A	532.0
Nanoparticle [14]	530.15	531.3 (O_v)	532.4
Nanoparticle [15]	530.2	531.4 (O_v)	532.6
Nanoparticle [11]	530.205	531.4 (O_v)	532.725
Film O-polar [16]	N/A	531.6 (Zn-OH)	533.5
Wafer(0001) [17]	530.7	532.3 (Zn-OH)	533.5
Nanoparticle [12]	529.6	531.2 (Zn-OH)	532.3

Table 5.2: Estimated percentage of surface oxygen of different nature on ZnO surfaces based on intensities of Gaussian fits on the X-ray photoelectron O 1s spectra.

Sample	Lattice O_b	Lattice O_v	Adsorbed O_{ad}	Carbonates O_{cr}
MA-ZnO	**60%** (530.7 eV)	**40%** (531.5 eV)	**0%**	**0%**
ST-ZnO	**0%**	**56%** (531.4 eV)	**44%** (533.0 eV)	**0%**
MS-ZnO	**0%**	**0**	**54%** (532.7 eV)	**46%** (534.3 eV)

from ambient O_2 [11]. As a result, the concentration of O_{ad} is considered as a good indicator of the surface reactivity for ZnO particles under ambient conditions [12].

Among the ZnO samples tested in this study, the presence of a ZHC layer is evident on MS-ZnO (Table 5.2), indicating that the surface undergoes a composition transformation under ambient conditions. In our previous investigation, such ambient instability was attributed to particular polar surfaces of hexagonal bi-pyramid shaped MS-ZnO [10]. No sign of a ZHC layer was found on the surfaces of other two ZnO samples. On the surfaces of MA-ZnO,

which was subjected to prolonged annealing (8 h at 500 °C), the majority of the surface O are the bulk O_b. In contrast, a higher concentration of chemisorbed oxygen was observed on the surfaces of ST-ZnO nanoparticles prepared by a low temperature solvothermal route.

It is worthy of note that the XPS data were measured at room temperature. Thus, the results cannot be directly correlated with ZnO surface reactivities at high temperature because the surface chemistry could change significantly at high T. For instance, the ZHC layer which decomposes at $\sim$ 280 °C on MS-ZnO would disappear at our operating temperature (350-450 °C). Nevertheless, we still assume—based on the XPS data—that the O_2 chemisorption ability of MA-ZnO is lower than that of ST-ZnO in high T environments. The same rationale has also been adopted by others who assessed high T surface activity of ZnO surface based on the room temperature XPS data [11, 12].

5.4.2 Capacitance gas sensing responses

Capacitive responses of ZnO samples to 1000 ppm of target gases at different temperatures are included in Table 5.3. Several trends can be summarized based on the testing results.

5.4.2.1 Some ZnO samples show stronger responses than others

ZnO samples prepared by different synthetic methods behave differently when tested as capacitive gas sensors (Table 5.3). At room temperature, ST-ZnO

Table 5.3: Summary of capacitance responses and recovery time constant τ of ZnO samples when exposed to different target gases at various temperatures (NR denotes "No Response", and N/A means "data not available").

Sample		**ST-ZnO**				**MS- ZnO**		**MA-ZnO**	
Temperature → Target gas ↓		22°C	350°C	400°C	450°C	22°C	350 to 450°C	22°C	350 to 450°C
Water vapor (90%)	S (%)	20±2	66±3	N/A	N/A	2.0±0.1	N/A	2.6±0.3	N/A
	τ (s)	43±2	120±5	N/A	N/A	8±1	N/A	38±5	N/A
EtOH	S (%)	6±2	150±25	110±20	110±20	0.3±0.05	0.3±0.05	0.15±0.06	NR
	τ (s)	10±1	14±2	14±2	14±2	1.5±0.5	N/A	13±2	N/A
Hexane	S (%)	-22±2	260±20	210±20	230±25	-2.7±0.3	0.5±0.1	-0.15±0.1	NR
	τ (s)	45±5	17±2	14±2	14±2	50±5	N/A	39±5	N/A
Toluene	S (%)	-18±2	NR			NR		-0.15±0.1	NR
	τ (s)	45±5	N/A			N/A		39±5	N/A

a b

[a]The responses $S(\%)$ for ST-ZnO are original, but $S(\%)$ for MA-ZnO and MS-ZnO samples were adjusted according to their normalized surface-area-to-volume ratios to that of the ST-ZnO from the BET measurement

[b]The negative values correspond to capacitance decreases after gas exposure.

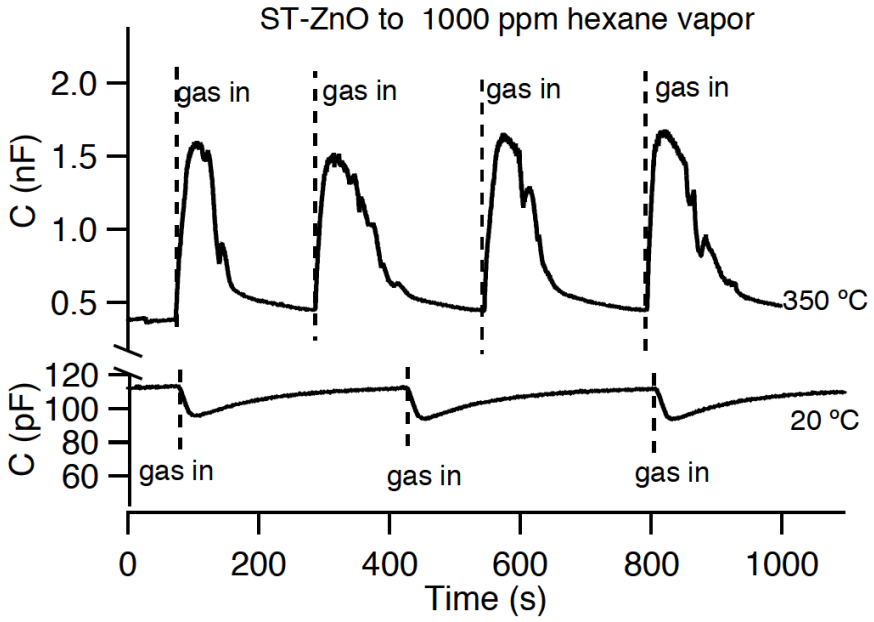

Figure 5.2: Comparison of representative sensing responses of ST-ZnO to 1000 ppm of hexane vapor measured between room temperature (20 °C) and high T (350 °C), dash lines indicate the moments of gas introduction and release. At RT, the film shows negative responses to hexane pulses.

shows the highest capacitance responses to EtOH vapor, averaging 10 times higher than MA-ZnO and MS-ZnO. (Interestingly, MS-ZnO exhibits fastest gas recovery (τ) that is approximately one order of magnitude faster than the other two, which is not understood).

At 350 °C, the sensing responses vary drastically among samples. For example, when sensing EtOH, ST-ZnO shows a $\sim$ 20 time enhancement in capacitance responses (S increases from $\sim$ 6 to $\sim$ 150) as the operating temperature is increased from room temperature to 350 °C . In contrast, the MA-ZnO shows no capacitive response to EtOH at high T; and as for MS-ZnO, the responses remain low at high T and is comparable to that at RT.

5.4.2.2 Temperature affects the sign and magnitude of the capacitance change

By comparing the responses of ST-ZnO sensor to hexane vapor at different working temperatures (Fig. 5.2), we observe that in response to the same hexane pulses, the sensor's capacitance decreases (negative response) at low T, but increases (positive response) at high T. Moreover, for ST-ZnO, the magnitudes of sensing responses to EtOH and hexane are greatly promoted at high T, as shown in Table 5.3.

Three temperature regions can be identified based on the sensing behaviors of ST-ZnO that shows the best performances: in region I (room temperature), the capacitive responses are relative low, and sign of change

of capacitances is determined by the hydrophilicity of the target gas. Positive responses were observed when sensing hydrophilic EtOH gases, while exposures to hydrophobic gases (hexane and toluene) have led to negative responses of the sensing film. Region II is between 100 °C and 300 °C, for all the testing done at this region, no apparent sensing response was observed. Region III (350 to 450 °C) is the optimal sensing temperature range as maximum sensing responses to hexane and EtOH are reached.

5.5 Discussion

At high operating temperatures, we found that ZnO can sense hexane and EtOH capacitively with enhanced responses, compared to that at RT. Also, the impacts of gas hydrophilicity becomes insignificant in determining the gas selectivity at high T. At this stage, our results cannot directly validate any mechanism for the high T capacitive sensing behaviors. In Chapter 4, we proposed a RT sensing model that attributes the positive capacitance responses to the increases in the effective dielectric constant of the ZnO film after adsorption gas molecules with larger dielectric constant than the sensing layer (Section 4.7). However, this model has failed to explain the large positive response to hexane ($\epsilon = 1.88$, much smaller than ZnO) in Fig. 5.2. Furthermore, as an exploratory study, the significance of this work—even without a sensing mechanism—should not be underestimated because this work has provided useful information for optimizing capacitive VOCs

sensing performances for MOX at high T.

5.5.1 Working temperature

In our experiment, optimal capacitive sensing responses were obtained at temperatures above 300 °C, in agreement with the optimal operating temperature reported for MOX-based resistive-type sensors [6, 18]. Activation of the gas-surface combustive reaction is often cited as the main reason behind the high temperature requirement for MOX sensors [6, 19]. This temperature range could imply that the large capacitance responses of ZnO is transduced from the similar chemical processes that trigger the resistive sensing responses. However, this is merely a speculation at this stage.

5.5.2 Effects of ZnO preparation methods

ZnO samples synthesized by different methods show distinctive capacitive gas performances at high T. This may provide important guidance for adjusting our synthetic strategies to make improved MOX-based capacitive sensors. Our data indicate that ZnO with the smallest particle sizes (ST-ZnO) yields the best capacitive gas sensing responses. Moreover, surface reactivities could play an important role as well. For example, in our testing, the MA-ZnO sample prepared by prolonged high temperature annealing method shows poor sensing responses, which could be related to the lack of chemisorption sites on the ZnO surfaces prepared by this method, according to the XPS

results [20].

5.5.3 Target gas selectivity

At room temperature, we demonstrated that our ZnO can selectively sense gas molecules based on its hydrophilicity [4]. However, this control is weakened at high T as ZnO is responsive to both EtOH and hexane with capacitance increases. Furthermore, throughout our testing, no capacitance response was observed for toluene vapor by any ZnO sample (Table 5.3). A recent study reported toluene sensing in resistive mode by ZnO nanowires functionalized with Au nanoparticles that catalyze the reaction of toluene at ZnO surfaces [9]. As a result, we believe that the absence of capacitive toluene sensing response for our ZnO could due to the relative high stability of toluene against oxidation or combustion at ZnO surface. Regarding the same point, we think that the target gas selectivity in high T capacitive sensing could be achieved by tailoring the catalytic activity of ZnO—*via* doping or hybridization—toward a particular class of gaseous compounds, such as poly/mono-aromatic hydrocarbons.

5.6 Conclusions

We have explored the capacitive gas responses of polycrystalline ZnO at high temperatures. We show that the sensing performances are strongly influenced by several factors, including operating temperature, ZnO particle

sizes and shapes (surface reactivities). Our data show promises of utilizing ZnO as capacitive type gas sensor for high T gas sensing task (*e.g.* onsite monitoring of VOCs emissions at a flare stack).

What causes the large positive capacitance responses of ZnO films to VOCs (polar and non-polar) at elevated T is still a mystery. Solving it requires understandings of the chemical processes occurred at high T when gas molecules adsorb on the ZnO surfaces, and also the correlations between the chemical process and the resulting capacitance signal. For investigating the gas-surface reaction, spectroscopic techniques can be used. In this thesis, I employed XPS for studying the surface chemistry of ZnO powders in vacuum at RT. However, due to the dynamic nature of a gas sensing process, it could be helpful to use the spectroscopic technique that is *in situ*, meaning capable of characterization in real working conditions of the gas sensor (high T, with air flow) [6]. *In situ* spectroscopies based on diffuse reflectance infrared Fourier transformed (DRIFT) spectroscopy have been frequently used to study the reaction mechanism during a catalytic reaction on MOX surfaces [6]. For ZnO-based gas sensor, Chen *et al.* used this technique, combined with conductivity measurement, to investigate the NOx sensing mechanism at high T by ZnO in resistive mode. As for the sensing mechanism, a model has been proposed for resistive sensing mode by MOX which attributes the conductivity variation of ZnO sensing layer upon gas exposure to the charge transfer induced changes in the band bending that sequentially alters the potential barriers at the surface/interface of ZnO [6]. Unfortu-

nately, there remains a lack of widely accepted model for the capacitance responses.

Furthermore, we have demonstrated in this study that the sensing performances of the ZnO capacitive sensors can be optimized by reducing the particle size and/or altering the surface chemistry (particle shape). Another important parameter worth investigating for capacitive sensing performance optimization is the AC frequency. It has been reported that the dielectric properties as well as the capacitive gas sensing responses of ZnO at RT are heavily dependent on the AC frequency [3]. Regarding this point, I suggest an interesting future experiment that could involve electrical impedance spectroscopy (EIS), which allows us to examine various electronic properties for ZnO gas sensor as a function of frequency in the real-world working (high T) conditions.

5.7 Acknowledgments

Natural Science and Engineering Resource Council (Canada), Petroleum Research Atlantic Canada, and the Canada Foundation for Innovation (New Opportunities) funded this work. L. Whelan assisted with design and assembly of the high temperature gas sensing apparatus. H. Hirasawa and C. Han assisted with sample preparation as well as data collection.

Bibliography

[1] Hamid Farahani, Rahman Wagiran, and Mohd Nizar Hamidon. Humidity Sensors Principle, Mechanism, and Fabrication Technologies: A Comprehensive Review. *Sensors*, 14(5):7881–7939, 2014.

[2] Zhi Chen and Chi Lu. Humidity Sensors: A Review of Materials and Mechanisms. *Sens. Lett.*, 3(4):274–295, 2005.

[3] Xiaoyan Zhou, Jianpeng Li, Ming Ma, and Qingzhong Xue. Effect of Ethanol Gas on the Electrical Properties of ZnO Nanorods. *Physica E*, 32:1056–1060, 2011.

[4] Jiaqi Cheng, Muhammad Asim Rasheed, and Kristin M. Poduska. Exploiting Water-Mediated Ethanol Sensing by Polycrystalline ZnO at Room Temperature. *ECS J. Solid State Sci. Technol.*, 2(1):Q23–Q26, 2013.

[5] Mangilal Agarwal, Mercyma D. Balachandran, Sudhir Shrestha, and Kody Varahramyan. SnO_2 Nanoparticle-Based Passive Capacitive Sensor for Ethylene Detection. *J. Nano Mater.*, 2012:145406, 2012.

[6] N. Barsan, D. Koziej, and U. Weimar. Metal Oxide-Based Gas Sensor Research: How to? *Sens. Actuat. B*, 121:18–35, 2007.

[7] Liwei Wang, Yanfei Kang, Xianghong Liu, Shoumin Zhang, Weiping Huang, and Shurong Wang. ZnO Nanorod Gas Sensor for Ethanol Detection. *Sens. Actuat. B*, 162(1):237–243, 2012.

[8] A. Z. Sadek, S. Choopun, W. Wlodarski, S. J. Ippolito, and K. Kalantarzadeh. Characterization of ZnO Nanobelt-Based Gas Sensor for H_2, NO_2, and Hydrocarbon Sensing. *Sensors Journal, IEEE*, 7(6):919–924, June 2007.

[9] Liwei Wang, Shurong Wang, Mijuan Xu, Xiaojing Hu, Hongxin Zhang, Yanshuang Wang, and Weiping Huang. A Au-Functionalized ZnO Nanowire Gas Sensor for Detection of Benzene and Toluene. *Phys. Chem. Chem. Phys.*, 15:17179–17186, 2013.

[10] Jiaqi Cheng and Kristin M. Poduska. Ambient Degradation of ZnO Powders: Does Surface Polarity Matter? *ECS J. Solid State Sci. Technol.*, 3(5):P133–P137, 2014.

[11] Z. G. Wang, X. T. Zu, S. Zhu, and L. M. Wang. Green Luminescence Originates from Surface Defects in ZnO Nanoparticles. *Phys. E*, 35(1):199–202, 2006.

[12] R. Al-Gaashani, S. Radiman, A. R. Daud, N. Tabet, and Y. Al-Douri. XPS and Optical Studies of Different Morphologies of ZnO Nanostructures Prepared by Microwave Methods. *Ceram. Inter.*, 39(3):2283–2292, 2013.

[13] M. N. Islam, T. B. Ghosh, K. L. Chopra, and H. N. Acharya. XPS and X-ray Diffraction Studies of Aluminum-Doped Zinc Oxide Transparent Conducting Films. *Thin Solid Films*, 280:20–25, 1996.

[14] M. Chen, X. Wang, Y. H. Yu, Z. L. Pei, X. D. Bai, C. Sun, R. F. Huang, and L. S. Wen. X-ray Photoelectron Spectroscopy and Auger Electron Spectroscopy Studies of Al-doped ZnO Films. *Appl. Surf. Sci.*, 158:134 –140, 2000.

[15] P.-T. Hsieh, Y.-C. Chen, K.-S. Kao, and C.-M. Wang. Luminescence Mechanism of ZnO Thin Film Investigated by XPS Measurement. *Appl. Phys. A*, 90(2):317–321, 2008.

[16] M. Kunat, St. Gil Girol, U. Burghaus, and Ch. Wöll. The Interaction of Water with the Oxygen-Terminated, Polar Surface of ZnO. *J. Phys. Chem. B*, 107(51):14350–14356, 2003.

[17] B. J. Coppa, R. F. Davis, and R. J. Nemanich. Gold Schottky Contacts on Oxygen Plasma-Treated, n-Type ZnO(0001). *Appl. Phys. Lett.*, 82(3):400–402, 2003.

[18] Yali Cao, Pengfei Hu, Weiyu Pan, Yudai Huang, and Dianzeng Jia. Methanal and Xylene Sensors Based on ZnO Nanoparticles and Nanorods Prepared by Room-Temperature Solid-State Chemical Reaction. *Sens. Actuat. B*, 134:462–466, 2008.

[19] G. Korotcenkov. Metal Oxides for Solid-State Gas Sensors: What Determines Our Choice? *Mater. Sci. Eng. B*, 139(1):1–23, 2007.

[20] Mohammad R. Alenezi, Abdullah S. Alshammari, K. D. G. I. Jayawardena, Michail J Beliatis, Simon J. Henley, and S. R. P. Silva. Role of the Exposed Polar Facets in the Performance of Thermally and UV Activated ZnO Nanostructured Gas Sensors. *J. Phys. Chem. C*, 117(34):17850–17858, 2013.

Chapter 6

UV Photoresponses of ZnO under DC and AC Conditions: A Preliminary Study

6.1 Abstract

In this chapter, we present preliminary results from a study of photoresponses of ZnO polycrystalline samples to UV light. This study is motivated by an idea that gas sensing responses of ZnO can be substantially enhanced by UV light stimulation—an alternative to the conventional thermal activation strategy that requires heating of the sensing element [1]. Herein, using impedance spectroscopy, we show that the sign and magnitude of UV light responses of ZnO depend on the AC frequency.

6.2 Introduction

Change in conductivities of some materials upon exposure to UV light has sparked their applications in binary switches for imaging techniques, flame sensing, and optoelectronic circuits [2]. For this UV detection, traditional Si-based photodetectors require filters to eliminate interference from other low energy (IR, visible) lights, due to the small band gap of Si (1.1 eV). As a result, recent development of new UV detectors has focused on wide band gap materials, such as SiC, diamond, GaN, and metal oxides [2–4]. Among them, ZnO attracted extensive attention because of its large room temperature band gap (3.37 eV), high UV sensing efficiency, strong radiation hardness, and low cost [3]. Also, the UV cut-off wavelength can easily be adjusted by doping the ZnO with other elements, such as Mg [3].

The mechanism behind photoresponses may vary, depending on the materials or devices [5, 6]. For ZnO, it has been shown that surface states play dominant roles [5], which led to a flourish of research activity related to ZnO nanostructures (nanowire, nanorod) due to their large surface-volume ratios and large response [2]. When light shines, ZnO absorbs photons with energy greater than the band gap of ZnO, triggering the generation of electron-hole pairs in the bulk ZnO. The holes then migrate to surface and neutralize pre-adsorbed oxygen ions at the surface (O_2 can readily form surface O^{2-} on ZnO surfaces under ambient conditions [5, 7]). The overall process can be expressed by the following equations:

$$h\nu \longrightarrow h^+ + e^- \tag{6.1}$$

$$O_2{}^-{}_{(ad)} + h^+ \longrightarrow O_{2(gas)} \tag{6.2}$$

the combination of photo-generated holes (h^+) with the pre-adsorbed oxygen ions ($O_2{}^-$) leads to desorption of O_2 from ZnO (Eqn. 6.2). Subsequently, the unpaired electrons contribute to the conductivity increase. According to this mechanism, the photoresponse of ZnO is controlled by the O_2 adsorption/desorption equilibrium at surfaces.

Electrical impedance spectroscopy (EIS) has been applied explicitly by some groups for investigating the UV light induced changes in the electrical behaviors of polycrystalline ZnO films [8–10]. In an earlier study, Martins *et al.* compared EIS spectra of nano-crystalline ZnO films taken before and during UV exposure in vacuum at room temperature, and concluded that under a vacuum, ZnO films with small average grain sizes, high porosity and low level of surface oxidation would show enhanced overall responses in AC impedance as well as DC conductivity to UV irradiation [9, 10]. In a more recent study, Morfa *et al.* combined EIS with gas chromatography mass spectrometry (GC-MS) to probe the chemical origin of the UV responses of ZnO nano-crystalline film in an ambient environment [8]. They showed that the changes of ZnO film's impedance are accompanied by desorption of O_2, water and other organic byproducts from ZnO surfaces *via* UV induced

photochemistry [8]. They also suggested that UV illumination could serve as a good method to "clean" the surface contaminants that may jeopardize performances of the ZnO-based electronics [8].

In this study, I focus on the impacts of AC frequency on UV responses of the ZnO samples reported in this dissertation. One novelty of this work is that I have shown that the sign of the UV responses of some ZnO samples depends on AC frequency. Upon UV exposure, AC resistance (the real component of the impedance) is decreased at low frequencies, consistent with its DC behavior. However, at higher frequencies, the sign of the UV response is reversed, and the same UV radiation causes an increase in the AC resistance of the ZnO film. I further demonstrate that this behavior is consistent with UV-induced changes in film's resistance and capacitance.

6.3 Experimental

6.3.1 ZnO film preparation

I tested UV responses for various ZnO samples (MA, ST, M, MS) that were prepared by methods described in Chapter 3 [11]. The crystal phase, particle size and surface characterization results for these samples are included in Chapter 3.

Preparation procedure for photo-sensing film is same as that for gas sensor, except that here the conductive indium tin oxide (ITO) coated glass slides (8-12 Ω, Delta Technology, Ltd.) were used as substrates. A layer of

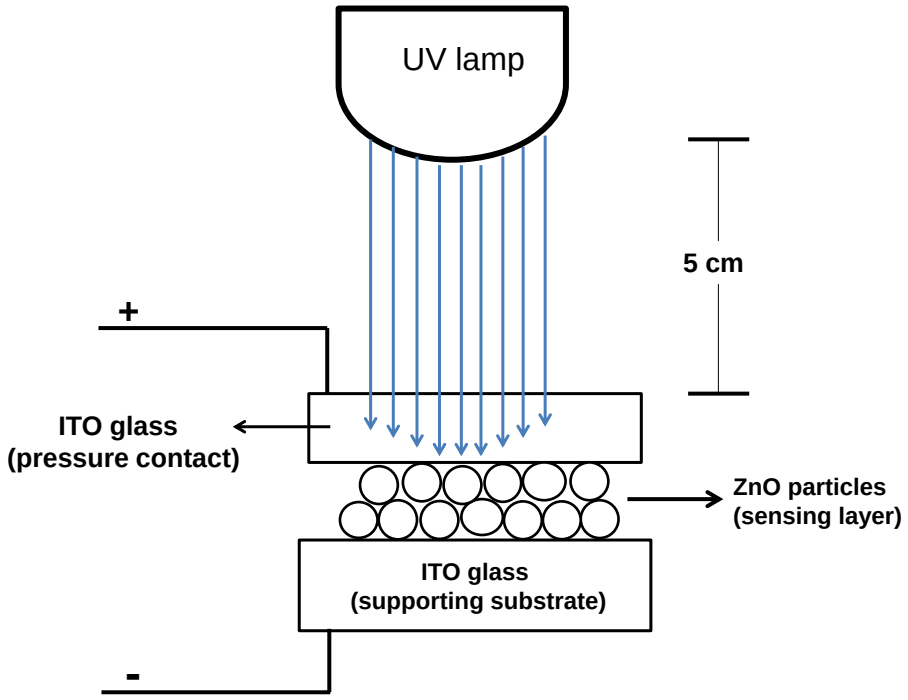

Figure 6.1: Schematic side view (not drawn to scale) depicting the UV measurement. The circles represent individual ZnO particles in the sensing layer.

ZnO sample was deposited on by a drop-casting method. A slurry was made by dispersing 0.10 g of the as-prepared ZnO powder in 2 mL of ethanol/water (1:1) mixture which was sonicated for 30 s. The slurry was then poured onto and spread evenly over the substrate that serves as one electrode. The second ITO electrode was pressed tightly on the top of the ZnO film by a binder clip.

6.3.2 Photoresponse measurements

Resistances of the ZnO films were measured with an inductance-capacitance-resistance (LCR) meter (National Instruments). A DC test current of 0.5 μA was applied across the sample film (meter range = 10 MΩ, resolution = 10 Ω). As illustrated in Fig. 6.1, the sample was illuminated by a 365 nm UV lamp (Model UVGL-25, UVP Inc.) with an intensity of 1.6 mW cm^{-2} at a distance of 5 cm. All measurements were conducted at room temperature (22 °C) and under steady humidity levels that were controlled using saturated salt solutions [12]. Prior to the measurements, ZnO films were allowed to equilibrate with the environment for 24 h. The photo-detection response S is calculated as:

$$S = \frac{R_{\text{off}}}{R_{\text{on}}} \tag{6.3}$$

where R_{off} and R_{on} are the sample's resistances in the dark and under UV exposure, respectively.

On samples that have shown large photo-responses in film resistance, further electrical impedance spectroscopy (EIS) study was performed using a Princeton Applied Research (PAR) Potentiostat/Galvanostat (Model 273A with Signal Recovery Model 5210 Lock-in Amplifier). The data collection was controlled using the Power SUITE software (Princeton Applied Research). The impedance measurement was done by applying a sinusoidal AC potential (RMS amplitude of 10 mV) with 0 DC bias to the sample with test frequencies

swept between 10^{-1} Hz and 10^{5} Hz. Analysis of the impedance data (circuit fitting) was performed using a freeware EIS Spectrum Analyser (Copyright: Aliaksandr Bandarenka and Genady Ragoisha), the circuit fitting was done by superimposing the simulated spectra onto the original ones and adjusting parameters manually by trial.

6.4 Results and Discussion

6.4.1 UV responses in film's resistance

Fig. 6.2 shows typical on/off photo-responses of four types of ZnO films when exposed to UV light. All four ZnO films respond to UV with a decrease in resistance, which is recovered after the UV light was turned off. Among them, the largest off/on resistance ratio is achieved by ST-ZnO ($S \sim 20$). MA-ZnO film shows the second largest response ($S \sim 3.7$), and both films of MS-ZnO and M-ZnO give poor responses with comparable $S \sim 1.1$. Fig. 6.2f demonstrates good repeatability of the UV responses by the MA-ZnO that is employed as test case in the following experiments.

6.4.2 Electrochemical impedance spectroscopy (EIS)

EIS spectra were taken for MA-ZnO and ST-ZnO samples that show good DC UV response and repeatability. The measurements were done in the dark and under UV light. Fig. 6.3 presents the representative Nyquist and Bode

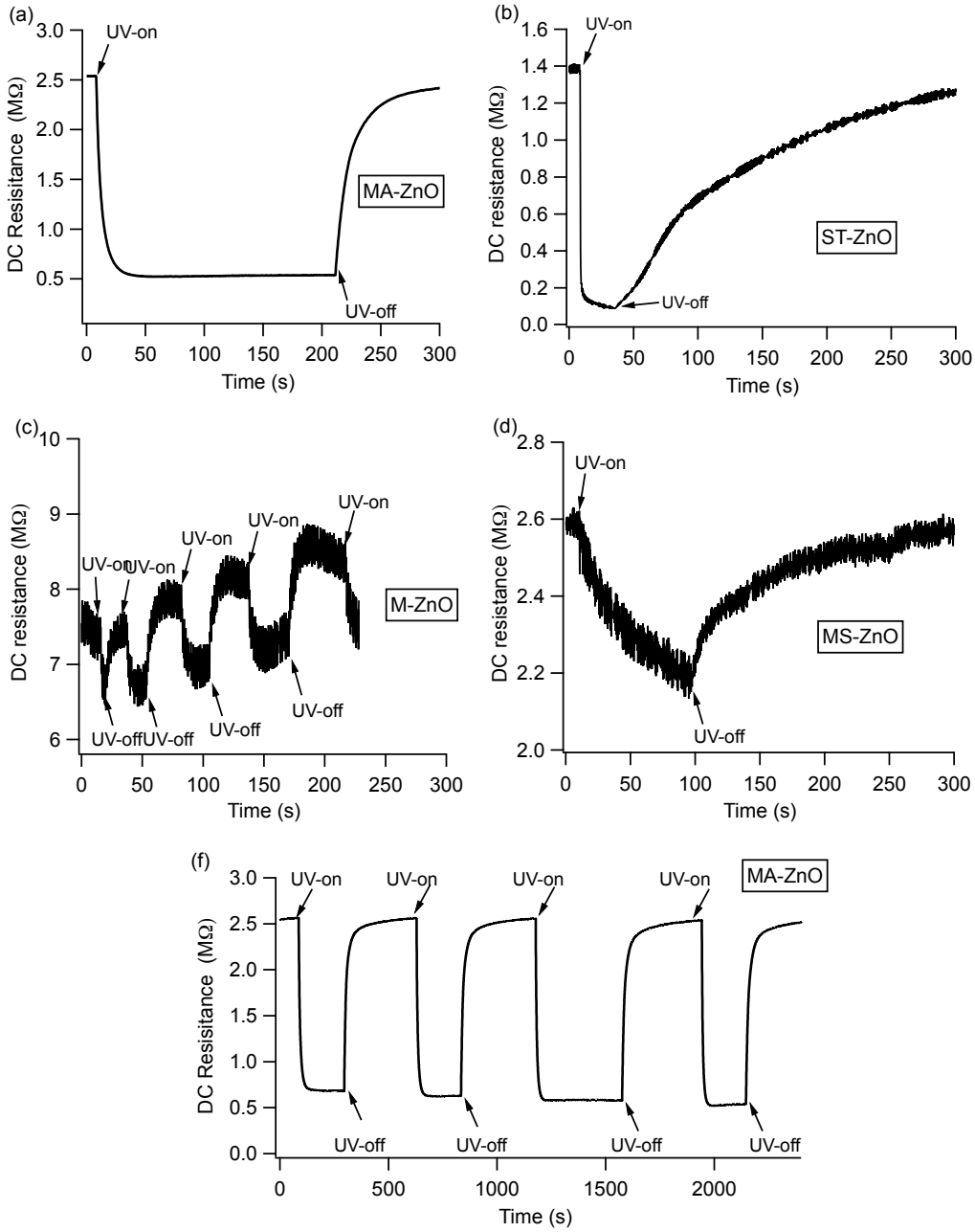

Figure 6.2: (a-d) Resistance variations of the four types of ZnO films (MA, ST, M and MS) in response to UV light exposure. In each plot, the on and off sequences of the UV light are indicated. (f) Demonstration of the repeatability of the UV responses of MA-ZnO sample with 4 on/off cycles.

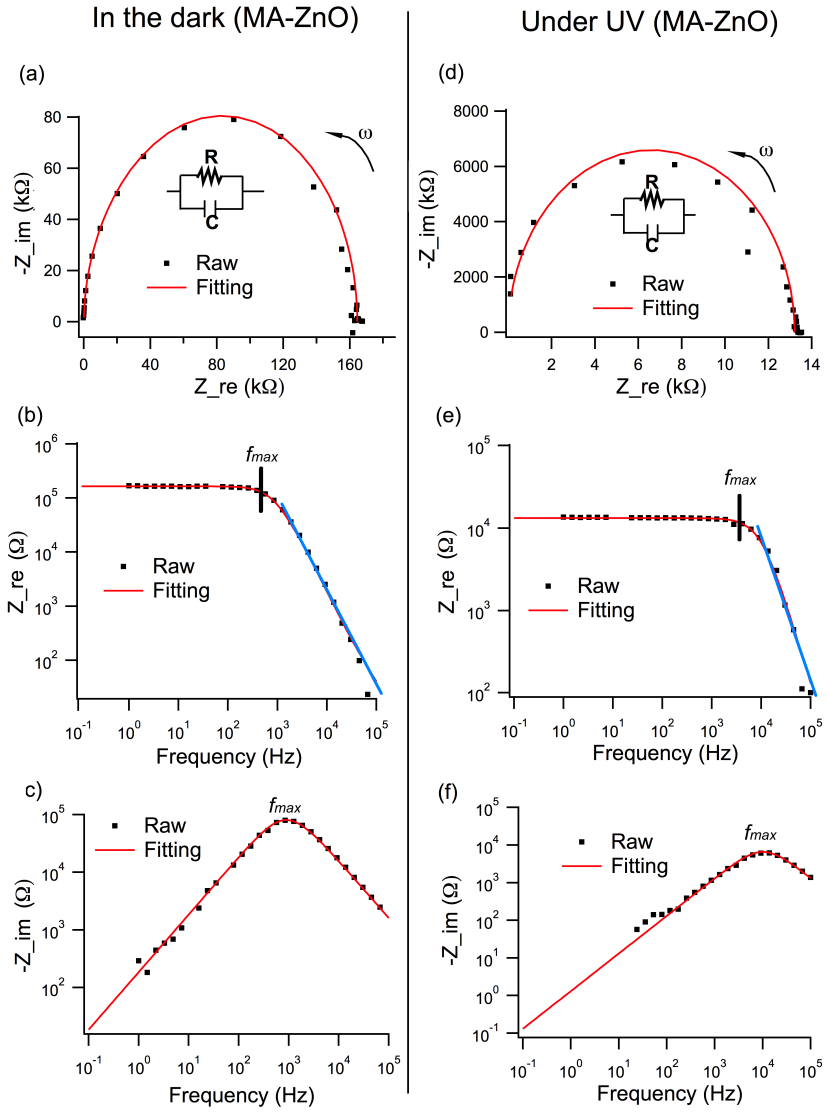

Figure 6.3: EIS data plotted in different forms (Nyquist (a and d) and Bode (b, c, e and f)) for the MA-ZnO film taken in the dark (a-c) and under UV illumination (d-f). Arrows in the Nyquist plots indicate the directions of the increasing frequency (from 0.1 Hz to 100 kHz) and raw data were fitted to an equivalent circuit (insert). A blue fitting line (in b and e) is applied to the portion of the spectrum to highlight the linear decreases in the log-log plot.

Table 6.1: Parameters extracted from the equivalent circuit fittings in Fig. 6.3 for MA-ZnO.

	R	C
MA-ZnO, Dark	150±5 kΩ	1.0±0.2 nF
MA-ZnO, UV	13.2±0.2 kΩ	1.2±0.2 nF

plots for the dark and light responses of MA-ZnO films. Equivalent circuits were constructed to fit the raw data, and the parameters are summarized in Table 6.1.

Both dark and UV the EIS spectra for the MA-ZnO can be fitted with a simple parallel RC circuit (Fig. 6.3a). From the R and C values extracted from the fitting parameters (Table 6.1), it appears that the UV effect on MA-ZnO sample is resistive because no apparent change has been found in film's capacitance between dark and UV. However, we can not extend this conclusion over other ZnO samples that show large DC UV response such as ST-ZnO, since its EIS spectrum indicates a more complicated behavior than single parallel RC. (Circuits fitting results and parameters for ST-ZnO are included in Fig. 6.8 and Table 6.3 in the Appendix).

In Fig. 6.3, we also present the Bode plots with the fittings because they clearly reveal the frequency dependence of Z_{re} and -Z_{im}. For a system showing a simple RC parallel circuit, the behavior of Z_{im} as a function of frequency follows a relationship [13]:

$$Z_{im}(f) = -R\frac{2\pi f\tau}{1+(2\pi f\tau)^2} \tag{6.4}$$

where τ is the time constant that is related to R and C of the system as well as f_{max} by:

$$\tau = RC = \frac{1}{2\pi f_{max}} \tag{6.5}$$

In log-log form, Eqn. 6.4 can be re-written as:

$$log(Z_{im}) = log(f) + log(-2\pi\tau R) - log(1 + (2\pi f\tau)^2) \tag{6.6}$$

According to this relation, f_{max} corresponds to a peak in the -Z_{im} Bode plot.

Similar to the imaginary component, the frequency dependence of the real component (Z_{re}) for a single parallel RC system can be expressed as:

$$Z_{re}(f) = \frac{R}{1 + (2\pi f\tau)^2} \tag{6.7}$$

In the log-log form:

$$log(Z_{re}) = log(R) - log(1 + (2\pi f\tau)^2) \tag{6.8}$$

When $f \ll f_{max}$, $Z_{re}(f) \rightarrow R$; as a result, Z_{re} is independent of f. At high frequencies ($f \gg f_{max}$), $Z_{re}(f) \rightarrow \mathrm{R}/(2\pi f)^2$, so it decreases at a rate of $1/(2\pi f)^2$, displaying a linear drop in the log-log plot as indicated by the straight lines in Fig. 6.3. In this case, the manifestation of f_{max} is the lowest frequency at which the roll-off in Z_{re} begins.

6.4.3 Frequency-dependent photoresponses

To clearly indicate the UV effects on ZnO films as a function frequency, I overlaid the Bode spectra of ZnO samples obtained in the dark and under UV illumination for comparison. (Z_{im} spectra is shown in Fig. 6.9 in the Appendix).

An interesting feature appears when the Z_{re} Bode spectra are overlaid. Fig. 6.4 shows dark and UV Z_{re} spectra for MA-ZnO. The dark spectrum intersects with the UV spectrum at 4000 Hz. This feature of intersection (denoted as f_{cross}) suggests that opposite UV responses in Z_{re} could occur, depending on the test frequency. At a frequency smaller than f_{cross}, the Z_{re} value for dark is larger than that for UV. However, beyond f_{cross}, the Z_{re} for UV becomes larger, implying that the UV exposure could lead to an increase in the Z_{re} in this frequency region. The same feature is observed for ST-ZnO, which gives rise to $f_{cross} = 540$ Hz after overlaying its dark and UV spectra (Fig. 6.5a).

To verify this assumption, I tested the real time photo-sensing response of ST-ZnO above and below f_{cross} (Fig. 6.5a). Fig. 6.5b compares the UV response of the film taken at 20 Hz and 2000 Hz, respectively. Upon UV exposure, Z_{re} at 20 Hz decreases, similar to its response in DC resistance. At 2000 Hz, however, Z_{re} responds to the UV light with a rise. This opposite frequency-dependent UV response is consistent with what the Bode spectra indicate. (UV response testing at fixed frequencies was not performed for MA-ZnO).

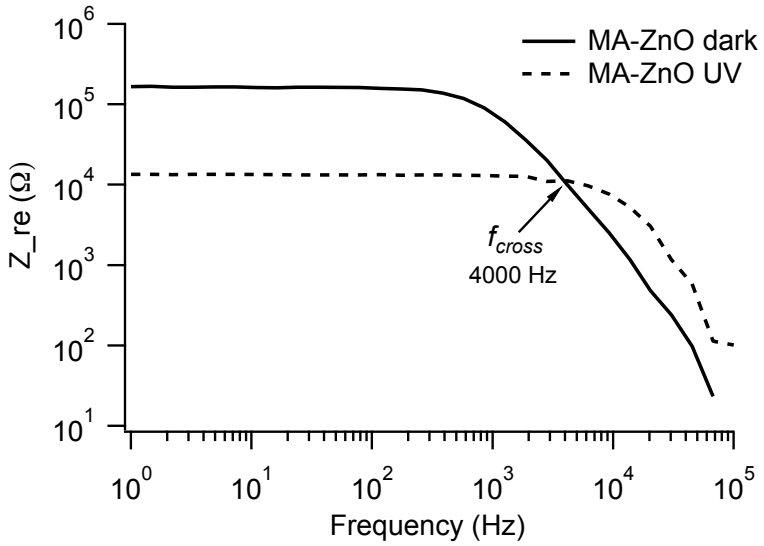

Figure 6.4: Comparison of Z_{re} Bode plots taken in the dark and under UV light for MA-ZnO. Intersection (f_{cross}) of the spectra is indicated by the arrow.

6.4.4 Simulating f_{cross}

Illumination by UV light changes the electrical behavior of our ZnO films, and the occurrence of f_{cross} is a direct result of the transition between the dark and UV behaviors. The next step of my investigation was to study the correlations between changing R and C, and the resulting f_{cross} and S. For this task, I simulated Z_{re} Bode plots using freeware (EIS Spectrum Analyser) that can generate EIS spectra in various forms from a circuit. To model the electrical behavior before exposing to UV, I used a single parallel RC circuit with $R = 100$ kΩ and $C = 1$ nF. This circuit was chosen based on the electrical response of MA-ZnO (Table 6.1), which shows a simple RC behavior before and after UV exposure. The effects of UV on the film were

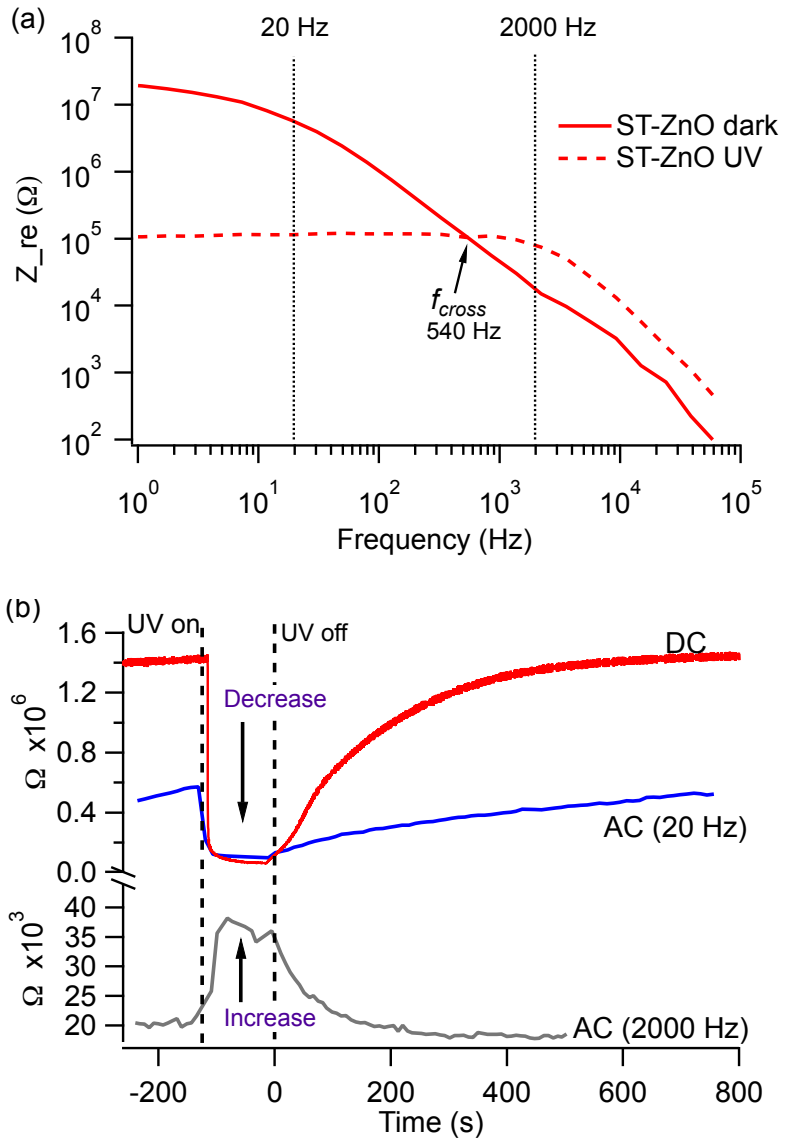

Figure 6.5: (a) Z_{re} Bode spectra taken in the dark and under UV light for ST-ZnO sample. f_{cross} is indicated by the arrow. The positions of 20 Hz and 2000 Hz on the Bode spectra are indicated. (b) compares the representative UV responses of ST-ZnO film for its DC resistance, Z_{re} at 20 Hz, and Z_{re} at 2000 Hz. The arrows indicate the direction of the UV response in each case.

modeled by varying the R and C values.

My simulations clearly show that changing R and C values result in a shift of Z_{re} spectra. Fig. 6.6a presents simulation results after decreasing C while keeping R constant. This manipulation leads to a shift of f_{max} toward higher frequencies and does not cause f_{cross}. Fig. 6.6b shows another scenario: decreasing R while keeping RC constant same by increasing C proportionally. In this case, Z_{re} drops over the whole frequency range without intersecting with the original spectrum. In Fig. 6.6c, I demonstrate that f_{cross} would occur when R (and RC constant) is decreased. Based on the simulation, I concluded that the occurrence of f_{cross} for a photodetector with single parallel RC behavior must satisfy two conditions:

$$(1)\ R_{dark} > R_{UV} \text{ and,}$$
$$(2)\ R_{dark} \times C_{dark} > R_{UV} \times C_{UV}$$

Relating the simulation to the experimental results, an apparent R change alone (without C change) would allow f_{cross} to occur, and would lead to the frequency-dependent sign change in the sensing response. This is consistent with the resistive response of MA-ZnO (Table 6.1).

The simulation also suggests that f_{cross} in the Z_{re} Bode plot could be estimated directly from the DC UV responses, since the Z_{re} at low AC frequency should be close to DC (equivalent to AC at 0 Hz) resistance. Following this lead, I then compared the photoresponses (S= $\mathrm{UV}_{off}/\mathrm{UV}_{on}$) between the time-dependent measurements and values extracted from the Z_{re} Bode spec-

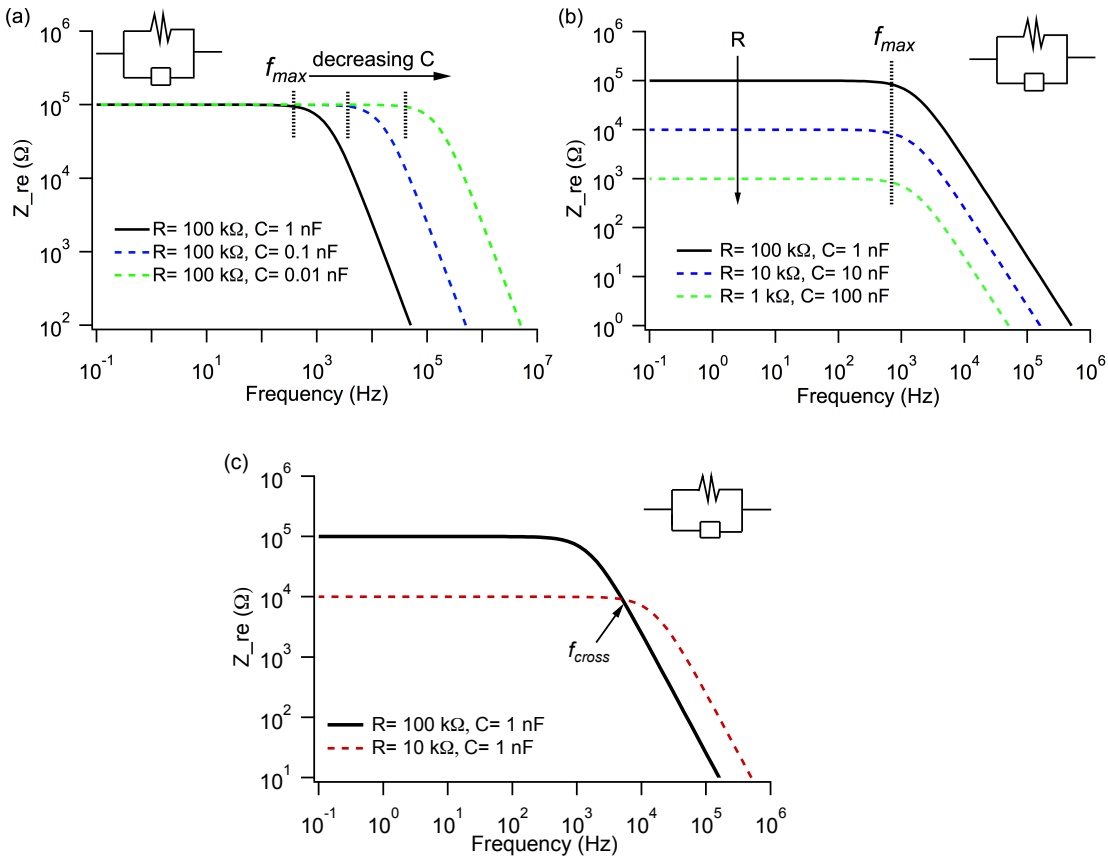

Figure 6.6: Simulated Bode Z_{re} spectra based on the single parallel RC circuit (insert). In (a), R was kept constant while C was decreased.The shift of f_{max} is indicated by arrow; in (b), RC was kept constant while R was decreased. The arrow indicates deceases of Z_{re} at the low frequency (flat) region due to decreasing R. (c) shows a scenario when R (and RC) was decreased. f_{cross} is indicated.

Table 6.2: Comparisons of photoresponses between the prediction ($S_{predict}$), *i.e.* values extracted from Z_{re} Bode spectra, and time-dependent measurements ($S_{measure}$). The $S_{predict}$ for DC (0 Hz) is not exact, but approximated with data at 1 Hz.

	MA-ZnO	ST-ZnO
$S_{predict}$ DC	12.2 ± 0.2	210 ± 30
$S_{measure}$ DC	4.0 ± 0.5	20 ± 2
$S_{predict}$ (20 Hz)	12.2 ± 0.2	50 ± 10
$S_{measure}$ (20 Hz)	N/A	9.0 ±1.0
$S_{predict}$ (2000 Hz)	2.6 ± 0.1	0.2 ± 0.1
$S_{measure}$ (2000 Hz)	N/A	0.5 ± 0.1

tra, as shown in Table 6.2. Nevertheless, there is a discrepancy between the photoresponse results obtained from the two measurements.

6.4.5 Humidity impact

I also attempted to study the UV responses of ZnO in a wet environment. Fig. 6.7 compares the dark and UV Z_{re} spectra for ST-ZnO between dry and wet environment (65% RH). The overall resistance of film has dropped considerably in the wet air. Moreover, as the film becomes wet, its UV response in R also becomes negligible. As a consequence, no intercept point (f_{cross}) can be seen from the dark and UV Z_{re} spectra in the wet air. This data indicates that the ambient humidity apparently impacts the electrical properties as well as photoresponses of ZnO films.

6.5 Conclusions

From the preliminary results based on ZnO powders, we observed an interesting effect in the AC frequency-dependent photoresponses: upon UV illumination, the AC resistance decreases at low frequencies. However, when measured at higher frequencies, the resistance increases in response to the same UV exposure. An EIS study & modeling over a range of frequencies (from 0.1 Hz to 100 kHz) has indicated that this frequency-dependent UV response results from a feature f_{cross} which is influenced by a resistance change induced by the UV exposure.

My findings suggest that it could be desirable to manipulate the R and C values of ZnO photo-detector for optimizing the frequency-dependent UV responses (such as avoiding or controlling the position of f_{cross}). ZnO can show a wide range of R values. The resistivity of undoped ZnO thin film can vary from 10^{-4} to 10^{8} Ω·cm as a function of oxygen concentration [14] and/or thickness of the films. Moreover, preliminary results show that the overall UV responses of ZnO films are reduced when ambient humidity level is high.

This study serves as an important part of my thesis theme of gas sensor development. My EIS investigation is motivated by exploiting the possibility of using UV stimuli as an alternative to high T for enhanced gas sensitivity of ZnO. My findings suggest that choosing an AC operating frequency based on the electrical characteristics of ZnO could play key roles in the UV-activated

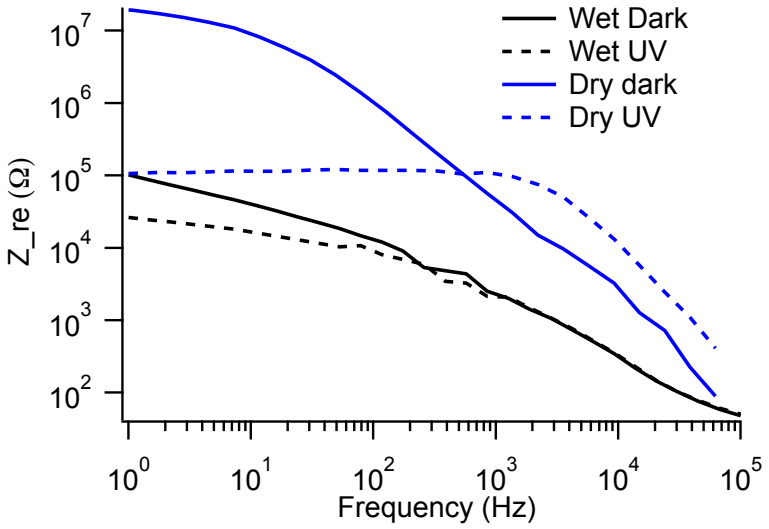

Figure 6.7: Bode plots comparing UV-induced changes of Z_{re} for ST-ZnO in a dry (20% RH) and wet (65% RH) environment.

gas sensing.

6.6 Appendix

An ST-ZnO film (Fig. 6.8a) presents a more complicated behavior which deviates from the single parallel RC circuit. Thus, I need a different equivalent circuit model. The best option I used was: a RC parallel circuit connected in series to a second RC in which the capacitor is replaced with a constant phase element (CPE). The impedance of a CPE can be expressed as:

$$Z_{\mathrm{CPE}} = \frac{1}{Q(i\omega)^{\alpha}} \tag{6.9}$$

Table 6.3: Parameters extracted from the equivalent circuit fittings for ST-ZnO (Fig. 6.8). Three UV exposure measurements were taken on the same sample (same contact spot) at intervals of 20 min.

	$R1$ MΩ	$C1$nF	$R2$ MΩ	Q nF	α
ST-ZnO, Dark	8.3±0.2	0.75±0.15	16.5±0.1	6.0±1.0	0.8
ST-ZnO, UV (run 1)	0.092±0.002	0.42±0.1	N/A		
ST-ZnO, UV (run 2)	0.118±0.002	0.40±0.05			
ST-ZnO, UV (run 3)	0.23±0.02	0.45±0.1			

where Q is the quasi-capacitance, i is the complex number and ω is the angular frequency. The exponent α takes a value between 0 (for a perfect resistor) and 1 (for a perfect capacitor). In the Nyquist plot, a manifestation of a CPE in parallel with a resistor is a depressed semicircle. Nevertheless, the fitting quality for dark ST-ZnO with this circuit is not great, despite of its improvement from the single RC. A plausible reason for this more complicated electrical behavior of ST-ZnO might be due to the high resistance of the film ($\sim 10^7$ Ω), which is comparable to the input impedance of the instrument (10 MΩ). Under UV illumination, the ST-ZnO shows a single parallel RC behavior.

Fig. 6.9 shows a comparison of -Z_{im} spectra between dark and UV for MA and ST-ZnO films. For both samples, f_{max} shifts to a higher frequency after UV exposure. The reproducibility of -Z_{im} Bode spectra measured under UV exposure was also examined with different runs (three measurements were taken on the same sample and same contact spot) while the sample was illuminated by UV. The interval between each run was 20 min. The position

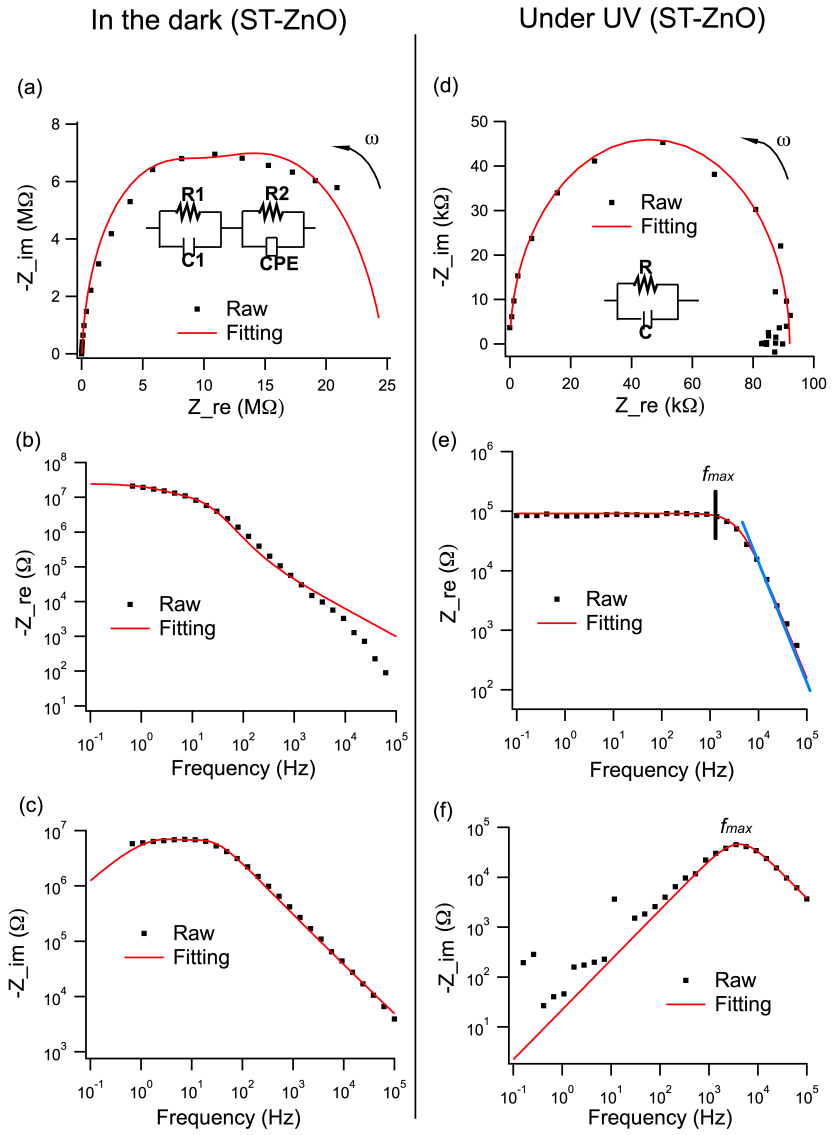

Figure 6.8: EIS data plotted in different forms (Nyquist (a and d) and Bode (b, c, e and f)) for the ST-ZnO film taken in the dark (a-c) and under UV illumination (d-f). Arrows in the Nyquist plots indicate the directions of the increasing frequency (from 0.1 Hz to 100 kHz) and raw data were fitted to an equivalent circuit (insert). A blue fitting line (in e) is applied to the portion of the spectrum to highlight the linear decrease in the log-log plot.

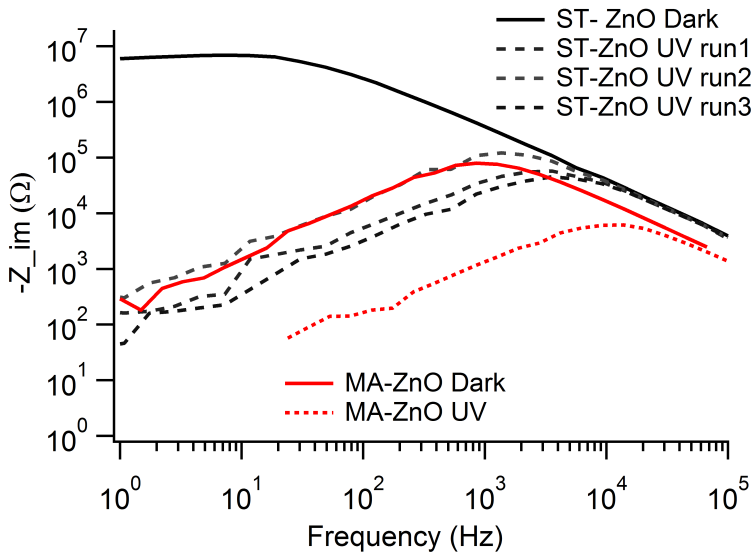

Figure 6.9: Comparison of Bode plots (expressed in Z_{im}) of ZnO films (MA and ST), both in the dark and under UV light.

of f_{max} in these three spectra ranges from 1500 Hz to 4000 Hz.

Bibliography

[1] Mohammad R. Alenezi, Abdullah S. Alshammari, K. D. G. I. Jayawardena, Michail J Beliatis, Simon J. Henley, and S. R. P. Silva. Role of the Exposed Polar Facets in the Performance of Thermally and UV Activated ZnO Nanostructured Gas Sensors. *J. Phys. Chem. C*, 117(34):17850–17858, 2013.

[2] Tianyou Zhai, Xiaosheng Fang, Meiyong Liao, Xijin Xu, Haibo Zeng, Bando Yoshio, and Dmitri Golberg. A Comprehensive Review of

One-Dimensional Metal-Oxide Nanostructure Photodetectors. *Sensors*, 9(8):6504–6529, 2009.

[3] Kewei Liu, Makoto Sakurai, and Masakazu Aono. ZnO-Based Ultraviolet Photodetectors. *Sensors*, 10(9):8604–8634, 2010.

[4] Liwen Sang, Meiyong Liao, and Masatomo Sumiya. A Comprehensive Review of Semiconductor Ultraviolet Photodetectors: From Thin Film to One-Dimensional Nanostructures. *Sensors*, 13(8):10482–10518, 2013.

[5] C. Soci, A. Zhang, B. Xiang, S. A. Dayeh, D. P. R. Aplin, J. Park, X. Y. Bao, Y. H. Lo, and D. Wang. ZnO Nanowire UV Photodetectors with High Internal Gain. *Nano Lett.*, 7(4):1003–1009, 2007.

[6] Lei Shi and S. Nihtianov. Comparative Study of Silicon-Based Ultraviolet Photodetectors. *Sensors Journal, IEEE*, 12(7):2453–2459, July 2012.

[7] Marion E. Franke, Tobias J. Koplin, and Ulrich Simon. Metal and Metal Oxide Nanoparticles in Chemiresistors: Does the Nanoscale Matter? *Small*, 2(1):36–50, 2006.

[8] Anthony J. Morfa, Brandon I. MacDonald, Jegadesan Subbiah, and Jacek J. Jasieniak. Understanding the Chemical Origin of Improved Thin-film Device Performance from Photodoped ZnO Nanoparticles. *Sol. Energ. Mat. Sol. Cells*, 124(0):211–216, 2014.

[9] R. Martins, E. Fortunato, P. Nunes, I. Ferreira, A. Marques, M. Bender, N. Katsarakis, V. Cimalla, and G. Kiriakidis. Zinc Oxide as An Ozone Sensor. *J. Appl. Phys.*, 96(3):1398–1408, 2004.

[10] R. Martins, R. Igreja, I. Ferreira, A. Marques, A. Pimentel, A. Goncalves, and E. Fortunato. Room Temperature DC and AC Electrical Behaviour of Undoped ZnO Films Under UV light. *Mater. Sci. Eng. B*, 118:135–140, 2005.

[11] Jiaqi Cheng and Kristin M. Poduska. Ambient Degradation of ZnO Powders: Does Surface Polarity Matter? *ECS J. Solid State Sci. Technol.*, 3(5):P133–P137, 2014.

[12] Jiaqi Cheng, Muhammad Asim Rasheed, and Kristin M. Poduska. Exploiting Water-Mediated Ethanol Sensing by Polycrystalline ZnO at Room Temperature. *ECS J. Solid State Sci. Technol.*, 2(1):Q23–Q26, 2013.

[13] C. Montella J. P. Diard, B. Le Gorrec. Handbook of EIS - Diffusion impedances. *Online resources, Bio-Logic Science Instrument, LTD.*, 2012.

[14] P. F. Carcia, R. S. McLean, M. H. Reilly, and G. Nunes. Transparent ZnO Thin-Film Transistor Fabricated by rf Magnetron Sputtering. *Appl. Phys. Lett.*, 82(7):1117–1119, 2003.

Chapter 7

A Strategy for Hydroxide Exclusion in Nanocrystalline Solid-State Metathesis Products

Reproduced with permission from MDPI [1].

7.1 Abstract

We demonstrate a simple strategy to either prevent or enhance hydroxide incorporation in nanocrystalline solid-state metathesis reaction products prepared in ambient environments. As an example, we show that $ZnCO_3$ (smith-

sonite) or $Zn_5(CO_3)_2(OH)_6$ (hydrozincite) forms extremely rapidly, in less than two minutes, to form crystalline domains of 11 ± 2 nm and 6 ± 2 nm, respectively. The phase selectivity between these nanocrystalline products is dominated by the alkalinity of the hydrated precursor salts, which may in turn affect the availability of carbon dioxide during the reaction. Thus, unlike traditional aqueous precipitation reactions, our solid-state method offers a way to produce hydroxide-free, nanocrystalline products without active pH control.

7.2 Introduction

Nanoparticle production *via* solid-state synthesis often involves metathesis of well-mixed solid precursors that react exothermically and quickly through a well-known class of self-sustaining reactions [2]. In comparison with traditional sol-gel or solvo-thermal routes, the absence of solvent in solid-state metathesis (SSM) has enabled rapid formation of a wide range of materials including metal oxides [3–6], sulfides [7], perovskites [8], and zeolites [9]. A typical synthesis is carried out at ambient temperature, pressure, and atmosphere conditions, where two powdered precursors are ground together. Once the reaction is triggered, a self-sustained exothermic reaction proceeds: no external heating is required. This metathesis is driven by thermodynamics and the formation of stable crystal products. Although the mechanism for ambient SSM is still not completely understood, some have noted that there

is a class of SSM reactions that appears to benefit from the precursors waters of hydration and/or from ambient water that is adsorbed at precursor grain interfaces [7]. It is possible that this small amount of water, which is released during the exothermic reaction to make a slurry with the starting powders, promotes diffusion and lowers the reactions activation energies.

Although ambient SSM has opened up a new window for expedient and solvent-free synthetic routes for many technologically and industrially relevant nanomaterials, unwanted incorporation of hydroxide or CO_2 species compromise the purity of the final product. These secondary products cannot always be removed by rinsing with water or organic solvents, and they are sometimes best removed by high temperature calcination [8]. Some reports have shown that this problem can be mitigated by dosing the precursor mixture with surfactants or other additives to control both crystal habit and composition [5, 10]. However, these additional components can present different issues for product purification, and the role of additives with regard to composition control during the metathesis process remains unclear.

Herein, we demonstrate that we can control hydroxide incorporation in nano-crystalline products using ambient SSM with a careful selection of precursors to affect pH in the small amount of water that is present. We demonstrate the efficacy of this approach with zinc carbonate nano-crystalline products: the hydroxide-free $ZnCO_3$ (ZC, smithsonite), as well as hydrozincite, $Zn_5(CO_3)_2(OH)_6$ (abbreviated here as ZHC). In nano-crystalline form, zinc carbonates have found industrial use as surface-active absorbers in respirators

for health and safety applications [11]. Neither additives nor post-synthesis annealing are required to regulate the composition of the metathesis product, nor is there any active pH regulation required during the synthesis.

7.3 Experimental

Our experiments began with analytical grade reagents: 0.5 mol of $Zn(NO_3)_2 \cdot 6H_2O$ was mixed with 1.5 mol of $NaHCO_3$ and then mixed thoroughly by hand in an agate mortar. The importance of this mixing is not at all related to mechanical pressure; instead, it is the intermingling of the powdered precursors that triggers the reaction. The total mass of the precursors was typically $\sim$ 1 g, but scaling up the reaction by a factor of ten did not adversely affect the results. After about 1 min of mixing, the exothermic reaction within the mixture yielded a wet white paste, with only a small temperature increase ($\sim$ 5 °C). Photographs of the paste-like products are shown in Fig. 7.1. This product was transferred to anhydrous ethanol and washed several times with ultrapure water (18.2 MΩ·cm) to remove soluble ions. The remaining product was oven dried at 80 °C for at least 24 h, prior to further characterization. Similar experiments were repeated with different combinations of precursors, as shown in Table 7.1. Results are highly reproducible, and were tested at least three times for each combination, including significant variations in the reactant ratios (0.67:1, 1:1, 1.5:1).

All samples were characterized by powder X-ray diffraction (PXRD; Ul-

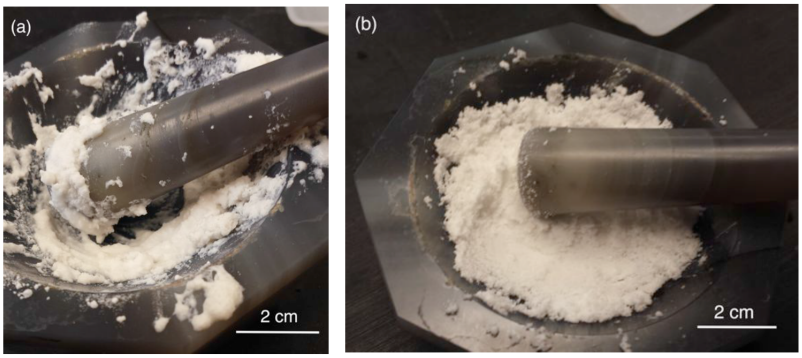

Figure 7.1: Representative photographs of the paste-like reaction products from (a) $Zn(NO_3)_2{\cdot}6H_2O$ and $NaHCO_3$ precursors, which yields $ZnCO_3$; and (b) $ZnCl_2$ + Na_2CO_3, which yields $Zn_5(CO_3)_2(OH)_6$

Table 7.1: Products from ambient SSM using different precursor combinations. Here, ZHC means $Zn_5(CO_3)_2(OH)_6$ and ZC means $ZnCO_3$. Gibbs free energy data are from [12]

Precursors	**Product**	**Calc. ΔG_0(kJ/mol) at 25°C**	
		ZC	**ZHC**
$ZnCl_2$ + $NaHCO_3$	none	-64	-278
$ZnCl_2$ + Na_2CO_3	ZHC	-86	-391
$Zn(NO_3)_2{\cdot}6H_2O$ + Na_2CO_3	ZHC	-71	-483
$Zn(NO_3)_2{\cdot}6H_2O$ + $NaHCO_3$	ZC	-85	-203

tima IV X-ray diffractometer (Rigaku, Texas, U.S.A.) with Cu Kα 3°/min, step size 0.02°; lattice constant refinements from Jade software, Materials Data Inc. (Livermore, CA, U.S.A.), comparison with JCPDS [13]), Fourier transform infrared spectroscopy (FTIR; Alpha spectrometer (Bruker, Billerica, MA, U.S.A.) at 4 cm^{-1} resolution on specimens dispersed in a 7 mm diameter KBr pellet), and Raman spectroscopy (Renishaw inVia Raman microscope, 830 nm excitation). Thermal decomposition experiments were conducted with a Q500 thermogravimetric analyzer (TA Instruments, New Castle, DE, U.S.A.) using a Pt pan, 600 °C (20.00 °C/min) under 40.0 mL/min N_2 gas flow). Crystalline domain sizes were extracted by Scherrer analyses on PXRD peak widths using at least 11 diffraction peaks. This approach gives a truly representative average crystalline domain size, since the data were obtained using $\sim$ 1 g of powder. Brunauer-Emment-Teller (BET) analyses provided surface area values.

7.4 Results and Discussion

The particles in the product are truly nanocrystalline, with crystalline domain sizes of 11 $\pm$ 2 nm for ZC and 6 $\pm$ 2 nm for ZHC, and surface areas of 25.4 $\pm$ 0.3 m^2/g for ZHC. From PXRD data, we find that ZC has sharper diffraction peaks (Fig. 7.2a) than ZHC (Fig. 7.2b). For this reason, we also used FTIR and Raman spectroscopies to corroborate the phase compositions of the products. As shown in the representative FTIR spectrum in Fig. 7.3a,

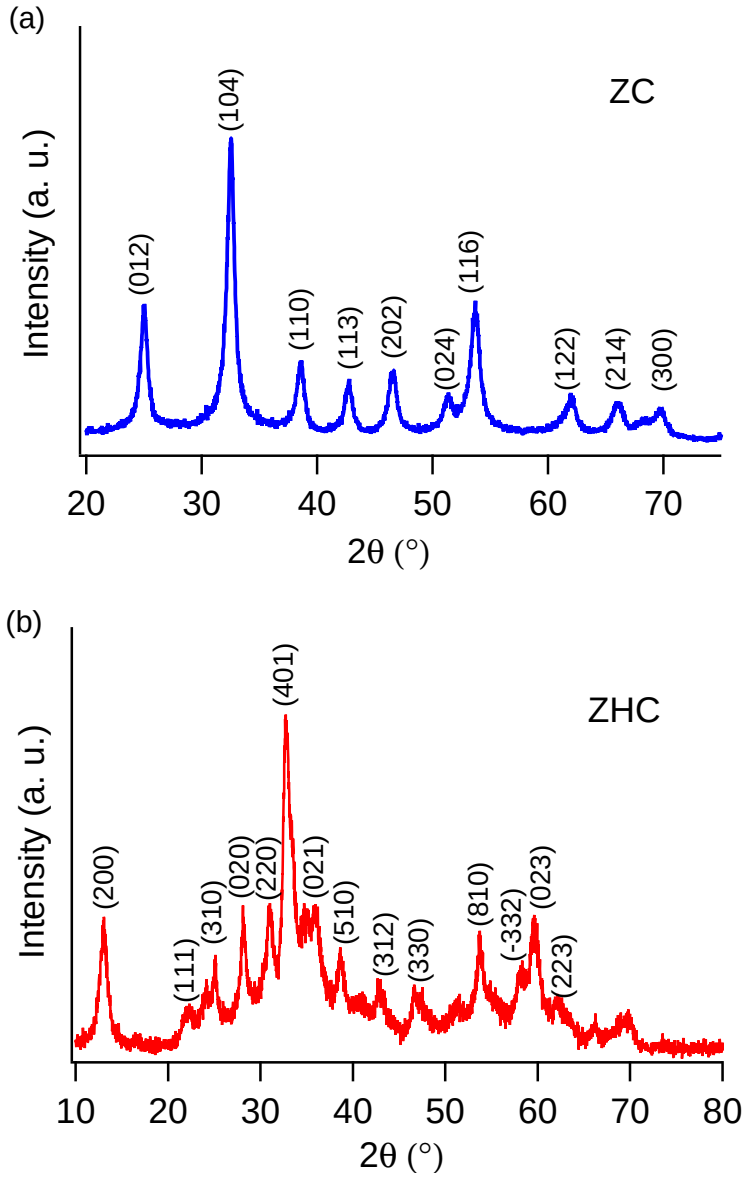

Figure 7.2: Representative indexed X-ray diffraction (XRD) data. In (a), all major peaks corresponding to $ZnCO_3$ (JCPDS 8-0449) are present when starting with $Zn(NO_3)_2$ and $NaHCO_3$ precursors. In (b), the product matches $Zn_5(OH)_6(CO_3)_2$ (JCPDS 19-1458) [13].

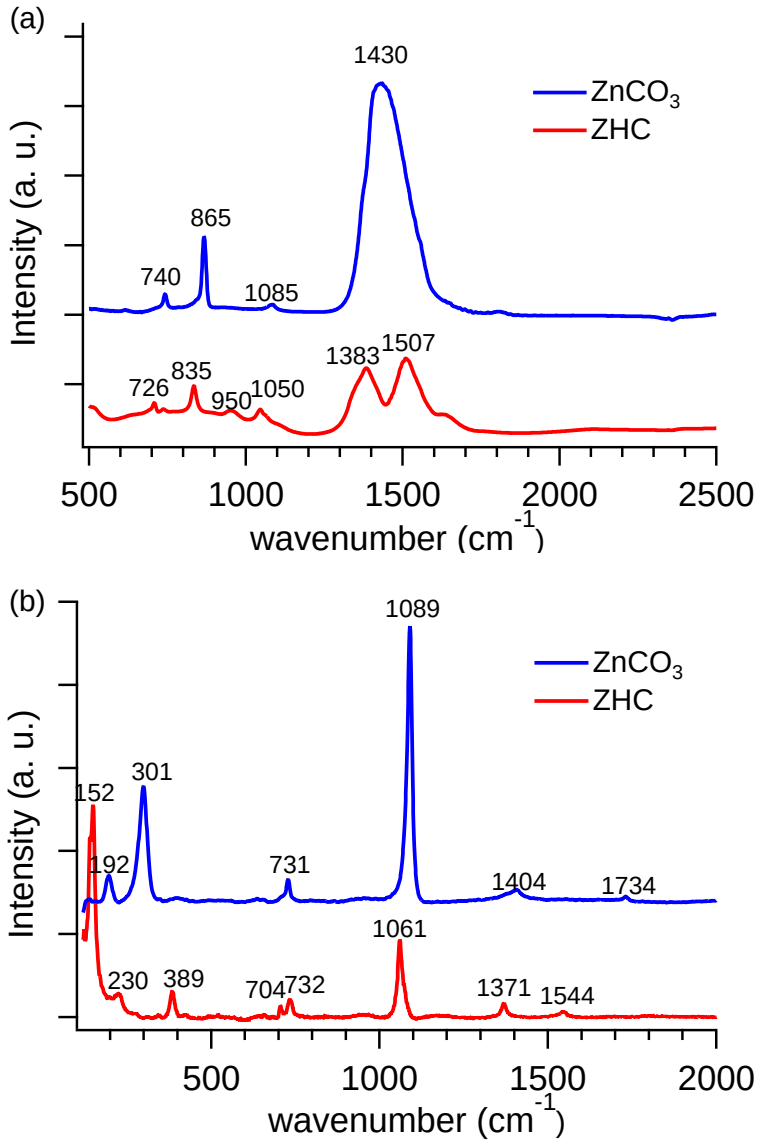

Figure 7.3: Representative (a) FTIR spectra and (b) Raman spectra for ZC and ZHC.

ZC displays an intense single peak at 1430 cm^{-1} (υ_3 antisymmetric carbonate stretch). Hydroxide incorporation in ZHC lowers the symmetry of this carbonate vibration [14] to yield multiple peaks between 1380 and 1510 cm^{-1}. A low intensity peak near 1085 cm^{-1} (υ_1 carbonate stretch) is IR inactive, according to ideal symmetry considerations [15], but is very intense in Raman spectra (Fig. 7.3b). For ZHC, this υ_1 mode is not observed in either FTIR or Raman spectra, however, the presence of a peak at 950 cm^{-1} has been attributed to a Zn-OH distortion in previous reports [16]. The carbonate υ_2 and υ_4 bending modes cause sharp peaks at 865 cm^{-1} and 740 cm^{-1}, respectively, in ZC; these peaks shift to lower wavenumbers and broaden in ZHC.

We performed additional experiments to ensure the SSM reactions yield phase-pure products. Thermal decomposition data indicate that both ZC and ZHC undergo a one-step decomposition process, releasing their carbonate and hydroxide ions simultaneously in the forms of CO_2 and H_2O (Fig. 7.4). The theoretical mass loss [17] for ZC is 35.1% when $ZnCO_3 \rightarrow ZnO + CO_2$; our yield was 33.9% $\pm$ 0.5%. For ZHC, we measured a mass loss of 25.8% $\pm$ 0.5%, which agrees well with the expected value [18] of 25.9% based on the reaction $Zn_5(CO_3)_2(OH)_6 \rightarrow 5ZnO + 2CO_2 + 3H_2O$. PXRD measurements confirmed that the decomposition product was ZnO, consistent with decomposition studies reported by others [19–21].

By comparing combinations of different precursors (Table 7.1), we find that only $Zn(NO_3)_2{\cdot}6H_2O + NaHCO_3$ yields the hydroxide-free $ZnCO_3$. Based

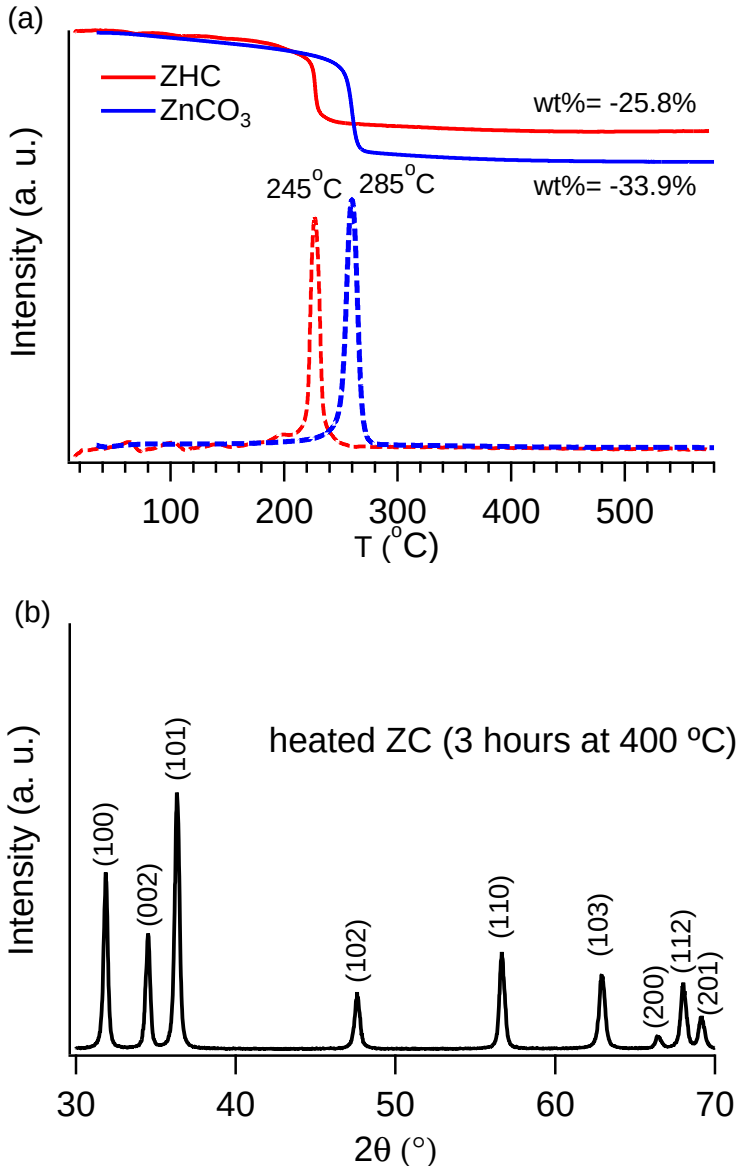

Figure 7.4: (a) $ZnCO_3$ (ZC, blue) and $Zn_5(CO_3)_2(OH)_6$ (ZHC, red) show one-step decomposition toward the formation of ZnO. The mass loss curves are shown as solid lines, and their derivatives are shown as dashed lines; (b) The decomposition products match ZnO (JCPDS 36-1451). The representative data shown here are for the product from ZC decomposition.

on results of previous aqueous precipitation experiments [11, 14, 18, 22–25], it appears that $NaHCO_3$ provides sufficient acidity and CO_2 to produce ZC, while Na_2CO_3 does not. We note that other carbonate precursor salts can also be used with similar effect. For example, K_2CO_3 gives results that are identical to those with a Na_2CO_3 precursor. It is also evident that the choice of the Zn precursor is quite important. For example, a self-sustained reaction did not occur between $ZnCl_2$ and $NaHCO_3$. We note that the wettest slurry occurred when using $Zn(NO_3)_2{\cdot}6H_2O$ and $NaHCO_3$ (as shown in Figure 7.1a). This would suggest that having sufficient water, contributed by either hydration waters or by absorption from the ambient environment, is also important to enable a self-sustained SSM reaction in this system. To assess the thermodynamics of the different precursor reactions shown in Table 7.1, we calculated the Gibbs energy of reaction based on the following four equations, in which X is either NO_3^- or Cl^- and n is an integer:

$$5ZnX_2{\cdot}nH_2O + 5Na_2CO_3 \rightarrow$$
$$Zn_5(CO_3)_2(OH)_6 + 3CO_2 + 10NaX + (5n\text{-}3)H_2O \quad (1)$$

$$ZnX_2{\cdot}\ nH_2O + 2NaHCO_3 \rightarrow ZnCO_3 + CO_2 + (n{+}1)H_2O + 2NaNO_3 \quad (2)$$

$$ZnX_2{\cdot}\ nH_2O + 2NaHCO_3 \rightarrow ZnCO_3 + CO_2 + H_2O + 2NaCl \quad (3)$$

$$5ZnCl_2 + 5Na_2CO_3 \rightarrow Zn_5(CO_3)_2(OH)_6 + 3CO_2 + 10NaCl + 3H_2O \quad (4)$$

In all four cases, the negative Gibbs energy of reaction values indicate that the reactions can proceed spontaneously. Both of our zinc carbonate products (ZC and ZHC) have a low solubility in water and, as a consequence,

aqueous syntheses by direct precipitation have been reported for each phase using a variety of different zinc salt precursors, including $ZnCl_2$, $Zn(NO_3)_2$, $ZnSO_4$, and $Zn(CHCOO)_2$. ZHC is the most common product under standard temperature and atmosphere conditions [22–24] with ZC formation reported only with acidic pH control [18] high CO_2 pressure [17, 25], or low temperatures [11]. In contrast, there is only one report of phase-pure ZC through ambient SSM, in which the authors conclude that the precursors (NH_4HCO_3 and $ZnSO_4$) had to be ground in the presence of an additional surfactant (polyethyleneglycol-octyl-phenylate) in order to yield ZC; a mechanism was not proposed [10].

We propose that three factors must be met for selective ZC or ZHC production: negative Gibbs free energy of reaction, sufficient structural and/or surface water, and crude pH control. As shown in Table 7.1, the calculated standard Gibbs free energy of reaction for each salts combination in SSM are all negative and thus thermodynamically possible. The Na_2CO_3 precursor, we believe, contributes to hydroxide incorporation in the product due to ${CO_3}^{2-}$ hydrolysis. In contrast, the dissociation of $NaHCO_3$ during the exothermic reaction provides a ready source of gaseous CO_2 that can be dissolved in the reaction slurry. ${HCO_3}^{-}$ also provides a sufficiently acidic environment in the slurry by preventing hydrolysis of ${CO_3}^{2-}$ with ambient water.

7.5 Conclusions

It is surprising and very widely applicable that a solid-state synthesis method can be adjusted to provide a robust way to exclude hydroxide under ambient temperature and atmosphere conditions. Crude pH control during the reaction is provided by acid-producing, hydrated precursor salts, and this is sufficient to produce phase-pure $ZnCO_3$. This is in stark contrast to reports of aqueous-based precipitation reactions for $ZnCO_3$, which have shown that accurate pH control is essential as acidic pH values ($\leq$6) lead to ZC dissolution, while excessively alkaline conditions promote $Zn(OH)_2$ formation at the expense of ZC [11, 14, 18, 25]. Furthermore, our solid-state products are nanocrystalline, in both the ZC and ZHC forms, due to the extremely rapid formation process. Our strategy of using acid-producing salts to form hydroxide-free carbonates could likely be extended to other classes of compounds for which pH is a tuning parameter for phase selectivity.

7.6 Acknowledgments

Natural Science and Engineering Resource Council (Canada), Petroleum Research Atlantic Canada, and the Canada Foundation for Innovation (New Opportunities) funded this work. K. Kenneally, J. Wells, and H. Hirasawa assisted with sample preparation. W. Aylward (PXRD), J. Collins (TGA), and M. Shaffer (SEM) granted use of the facilities they manage through Memorial University Core Research Equipment and Instrument Training network.

V. Booth at Memorial University granted use of DLS and zeta potential instrumentation. J. Wen and A. Chen conducted the BET measurements at Lakehead University, Thunder Bay, Ontario, Canada. Z. Bayindir conducted the XPS measurements at the Dalhousie University Facilities for Materials Characterization managed by the Institute for Research in Materials, which is funded by the Atlantic Innovation Fund and other partners.

Bibliography

[1] Jiaqi Cheng and Kristin M. Poduska. A Strategy for Hydroxide Exclusion in Nanocrystalline Solid-State Metathesis Products. *Nanomater.*, 3(3):317–324, 2013.

[2] John B. Wiley and Richard B. Kaner. Rapid Solid-State Precursor Synthesis of Materials. *Science*, 255(5048):1093–1097, 1992.

[3] Jin Q. Sun, Ji S. Wang, Xiu C. Wu, Guo S. Zhang, Jun Y. Wei, Shu Q. Zhang, H. Li, and Dai R. Chen. Novel Method for High-Yield Synthesis of Rutile SnO_2 Nanorods by Oriented Aggregation. *Cryst. Growth Des.*, 6(7):1584–1587, 2006.

[4] Sujith Perera, Nadiya Zelenski, and Edward G. Gillan. Synthesis of Nanocrystalline TiO_2 and Reduced Titanium Oxides via Rapid and Exothermic Metathesis Reactions. *Chem. Mater.*, 18(9):2381–2388, 2006.

[5] Jun Lu, Ka M. Ng, and Shihe Yang. Efficient, One-Step Mechanochemical Process for the Synthesis of ZnO Nanoparticles. *Ind. Eng. Chem. Res.*, 47(4):1095–1101, 2008.

[6] Arun Kumar Sinha, Mukul Pradhan, Sougata Sarkar, and Tarasankar Pal. Large Scale Solid State Synthesis of Sn-SnO_2 Nanoparticles from Layered SnO by Sunlight: A Material for Dye Degradation in Water by Photocatalytic Reaction. *Environ. Sci. Technol.*, 47(5):2339–2345, 2013.

[7] Xiang R. Ye, Dian Z. Jia, Jian Q. Yu, Xin Q. Xin, and Ziling Xue. One-Step Solid-State Reactions at Ambient Temperatures-A Novel Approach to Nanocrystal Synthesis. *Adv. Mater.*, 11(11):941–942, 1999.

[8] Eric S. Toberer, James C. Weaver, K. Ramesha, and Ram Seshadri. Macroporous Monoliths of Functional Perovskite Materials Through Assisted Metathesis. *Chem. Mater.*, 16(11):2194–2200, 2004.

[9] Limin Ren, Qinming Wu, Chengguang Yang, Longfeng Zhu, Caijin Li, Pengling Zhang, Haiyan Zhang, Xiangju Meng, and Feng-Shou Xiao. Solvent-Free Synthesis of Zeolites from Solid Raw Materials. *J. Am. Chem. Soc.*, 134(37):15173–15176, 2012.

[10] Wenwei Wu and Qiuyu Jiang. Preparation of Nanocrystalline Zinc Carbonate and Zinc Oxide via Solid-state Rection at Room Temperature. *Mater. Lett.*, 60(21-22):2791–2794, 2006.

[11] S. Zhang, H. Fortier, and J.R. Dahn. Characterization of Zinc Carbonate Hydroxides Synthesized by Precipitation from Zinc Acetate and Potassium Carbonate Solutions. *Mater. Res. Bull.*, 39(12):1939–1948, 2004.

[12] J. A. Dean. *Lange's Handbook of Chemistry.* McGraw Hill Book Co.,New York, NY, 1985.

[13] Powder Diffraction File Joint Commission on Powder Diffraction Standards – International Centre for Diffraction Data, 2003.

[14] Matthew C. Hales and Ray L. Frost. Synthesis and Vibrational Spectroscopic Characterisation of Synthetic Hydrozincite and Smithsonite. *Polyhedron*, 26(17):4955–4962, 2007.

[15] M. Bouchard and D. C. Smith. Catalogue of 45 Reference Raman Spectra of Minerals Concerning Research in Art History or Archaeology, Especially on Corroded metals and Coloured glass. *Spectrochim. Acta A Mol. Biomol. Spectrosc.*, 59(10):2247–2266, 2003.

[16] Bin Su, Mei Li, Zhengyu Shi, and Qinghua Lu. From Superhydrophilic to Superhydrophobic: Controlling Wettability of Hydroxide Zinc Carbonate Film on Zinc Plates. *Langmuir*, 25(6):3640–3645, 2009.

[17] M. C. Hales and R. L. Frost. Thermal Analysis of Smithsonite and Hydrozincite. *J. Therm. Anal. Calorim.*, 91:855–860, 2008.

[18] Nobuyoshi Koga, Yuri Goshi, Shuto Yamada, and Luis A. Pérez-Maqueda. Kinetic Approach to Partially Overlapped Thermal Decomposition Processes. *J. Therm. Anal. Calorim.*, 111(2):1463–1474, 2013.

[19] Zlatko Micković, Duncan T. L. Alexander, Andrzej Sienkiewicz, Marijana Mionić, László Forró, and Arnaud Magrez. Synthesis of Nanosized Mn-Doped ZnO by Low Temperature Decomposition of Hydrozincite Precursors. *Cryst. Growth Des.*, 10(10):4437–4441, 2010.

[20] Jun Zhang, Shurong Wang, Mijuan Xu, Yan Wang, Baolin Zhu, Shoumin Zhang, Weiping Huang, and Shihua Wu. Hierarchically Porous

ZnO Architectures for Gas Sensor Application. *Cryst. Growth Des.*, 9(8):3532–3537, 2009.

[21] S. V. Nistor, L. C. Nistor, M. Stefan, D. Ghica, Gh. Aldica, and J. N. Barascu. Crystallization of Disordered Nanosized ZnO Formed by Thermal Decomposition of Nanocrystalline Hydrozincite. *Cryst. Growth Des.*, 11(11):5030–5038, 2011.

[22] Xiurong Qu and Dechang Jia. Synthesis of Octahedral ZnO Mesoscale Superstructures via Thermal Decomposing Octahedral Zinc Hydroxide Precursors. *J. Cryst. Growth*, 311(4):1223–1228, 2009.

[23] Mojtaba Shamsipur, Seied Mahdi Pourmortazavi, Seiedeh Somayyeh Hajimirsadeghi, Mir Mahdi Zahedi, and Mehdi Rahimi-Nasrabadi. Facile Synthesis of Zinc Carbonate and Zinc Oxide Nanoparticles via Direct Carbonation and Thermal Decomposition. *Ceram. Inter.*, 39(1):819–827, 2013.

[24] Zhongjun Li, Xiaoqing Shen, Xun Feng, Peiyuan Wang, and Zhishen Wu. Non-Isothermal Kinetics Studies on the Thermal Decomposition of Zinc Hydroxide Carbonate. *Thermochimica Acta*, 438:102–106, 2005.

[25] Alwan K. Alwan and Peter A. Williams. Mineral Formation from Aqueous Solution. Part I. The Deposition of Hydrozincite, $Zn_5(OH)_6(CO_3)_2$, from Natural Waters. *Transition Met. Chem.*, 4(2):128–132, 1979.

Chapter 8

Summary and Outlook

8.1 Summary

My Ph.D. research focused on gas sensing with explorations of materials chemistry and materials electrical properties.

I explored capacitive gas sensing responses of different kinds of polycrystalline ZnO samples under humid and/or high temperature conditions in a laboratory setting. Under these conditions, I tested the sensing performances of ZnO samples to various VOCs. I discovered that at room temperature, selective gas detection is achievable with ZnO capacitive sensors even in humid environments [1]. At high temperatures, I found large enhancements in the capacitive gas sensing responses for sensors made of ZnO nanoparticles.

My emphasis on materials chemistry was reflected in the synthesis and ambient instability assessments of ZnO samples. I successfully applied (and

also developed) various techniques, including solid-state, solvothermal and high temperature methods to prepare micro-scale and nano-scale ZnO particles with controlled crystal habit and surface characteristics (surface area and surface polarity). Furthermore, I studied the instabilities of ZnO samples caused by interactions between ZnO surfaces and ambient water/CO_2, and linked the different degrees of reactivity of ZnO to surface dissolution and crystal growth conditions. This information has also proved helpful for understanding the distinctive gas sensing performances among different kinds of ZnO.

I also investigated the electrical properties of ZnO sensing films under UV light stimulation. Using impedance spectroscopy, I observed photoresponses that change sign, depending on the AC frequency applied during measurement; and I demonstrated that this frequency dependence is determined by the UV induced changes of electrical properties of the ZnO film.

8.2 Thesis contributions in a broader context

A thread running through my entire thesis—from solid-state metathesis, ambient instability, to the room temperature gas/UV sensing—is the impact of surface/interface water on materials properties. In my investigations, I found that ambient water can facilitate room temperature capacitive gas sensing [1], can cause surface degradations of ZnO [2], and can trigger solid-state reactions for synthesizing polycrystalline ZnO [3].

For the gas sensor community, humidity interference has been a long-standing issue. Many commercial gas sensors have to be calibrated for the background ambient humidity levels prior to use. The conventional strategy for solving this water problem is to reduce or avoid its presence. For instance, a collaborator of ours at the University of London, Dr. Russell Binions, developed a method to reduce humidity interference by incorporating a water absorbing layer (zeolites) into the sensors in order to screen the moisture from reaching the sensing elements [4–6]. Nevertheless, I believe my findings on ambient gas capacitive detection [1] provide a new route for resolving the moisture issue. Instead of focusing on preventing water interference (which is difficult), we may be able to take advantage of ambient water to promote gas sensing performance for hydrophilic gases. This vision might also be applicable to different sensing materials, such as SnO_2. Beyond MOX materials, conductive polymers [7] (polypyrrole, polyaniline) have higher overall gas sensitivities at room temperature than MOX, but also suffer from even more severe humidity interference [7].

My contributions in materials chemistry and electrical properties may also impact other fields beyond gas sensors. As a functional material with a range of optical, piezoelectric, and sensor device applications [8], ZnO has always been celebrated for its structural stability, despite some awarenesses of its degradation issue under humid conditions [9–11]. My study on the surface carbonation of ZnO [2] once again raised this important issue. It is very likely that many electronic and optical functionalities of ZnO would fail

in ambient environments once ZnO is transformed to zinc carbonates. This implies that measures for moisture and CO_2 prevention may be required for ensuring the long term stability of ZnO-based devices.

Finally, the solid-state metastasis method is one of my favorite methods for synthesizing binary nanomaterials because it contains many green chemistry characteristics: solvent free, high yield, no heating requirement, and ultra-fast reaction [12]; and ambient humidity is likely involved in triggering the reaction. I have opened up a new way to impose control over crystal phases of the SSM products by tuning the acid/base chemistry at interfaces of the solid grains.

Bibliography

[1] Jiaqi Cheng, Muhammad Asim Rasheed, and Kristin M. Poduska. Exploiting Water-Mediated Ethanol Sensing by Polycrystalline ZnO at Room Temperature. *ECS J. Solid State Sci. Technol.*, 2(1):Q23–Q26, 2013.

[2] Jiaqi Cheng and Kristin M. Poduska. Ambient Degradation of ZnO Powders: Does Surface Polarity Matter? *ECS J. Solid State Sci. Technol.*, 3(5):P133–P137, 2014.

[3] Jiaqi Cheng and Kristin M. Poduska. A Strategy for Hydroxide Exclusion in Nanocrystalline Solid-State Metathesis Products. *Nanomater.*, 3(3):317–324, 2013.

[4] R. Binions, H. Davies, A. Afonja, S. Dungey, D. Lewis, D. E. Williams, and I. P. Parkin. Zeolite-Modified Discriminating Gas Sensors. *J. Electrochem. Soc.*, 156:J456–J51, 2009.

[5] R. Binions, A. Afonja, S. Dungey, D. W. Lewis, I. P. Parkin, and D. E. Williams. Discrimination Effects in Zeolite Modified Metal Oxide Semiconductor Gas Sensors. *Sensors Journal, IEEE*, 11(5):1145–1151, 2011.

[6] William J. Peveler, Russell Binions, Stephen M. V. Hailes, and Ivan P. Parkin. Detection of Explosive Markers Using Zeolite Modified Gas Sensors. *J. Mater. Chem. A*, 1:2613–2620, 2013.

[7] Ehsan Danesh, Francisco Molina-Lopez, Malick Camara, Alexia Bontempi, Andrés Vásquez Quintero, Damien Teyssieux, Laurent Thiery, Danick Briand, Nico F. de Rooij, and Krishna C. Persaud. Development of A New Generation of Ammonia Sensors on Printed Polymeric Hotplates. *Anal. Chem.*, 86(18):8951–8958, 2014.

[8] Ü. Özgür, Daniel Hofstetter, and Hadis Morkoç. ZnO Devices and Applications: A Review of Current Status and Future Prospects. *Proc. IEEE*, 98(7):1255–1268, 2010.

[9] Yang Yang, Dong Sik Kim, Yong Qin, Andreas Berger, Roland Scholz, Hyunbin Kim, Mato Knez, and Ulrich Gösele. Unexpected Long-Term Instability of ZnO Nanowires Protected by a TiO_2 Shell. *J. Am. Chem. Soc.*, 131(39):13920–13921, 2009.

[10] Zhengwei Pan, Jing Tao, Yimei Zhu, Jing-Fang Huang, and M. Parans Paranthaman. Spontaneous Growth of $ZnCO_3$ Nanowires on ZnO Nanostructures in Normal Ambient Environment: Unstable ZnO Nanostructures. *Chem. Mater.*, 22(1):149–154, 2010.

[11] K. A. Cimatu, S. M. Mahurin, K. A. Meyer, and R. W. Shaw. Nanoscale Chemical Imaging of Zinc Oxide Nanowire Corrosion. *J. Phys. Chem. C*, 116(18):10405–10414, 2012.

[12] Rafael Luque and Rajender S Varma. *Sustainable Preparation of Metal Nanoparticles*. RSC Green Chemistry. The Royal Society of Chemistry: London, UK, 2012.